Abstract of the Dissertation

The Center-of-Mass Angular Distribution of Direct Photons at $\sqrt{s} = 1.8TeV$ Observed With the DØ Detector.

by

Paul Michael Rubinov

Doctor of Philosophy

in

Physics

State University of New York at Stony Brook

1995

The study of center-of-mass angular distribution of direct photons produced in $p\overline{p}$ collisions at $\sqrt{s} = 1.8TeV$ with the DØ detector is described. The photons are detected and identified using a liquid argon calorimeter, with charged particle rejection provided by tracking chambers. The photons are restricted to the central region ($\eta \leq 0.75$), but center-of-mass system for the hard scattering is reconstructed using the information from reconstructed jets. A method for avoiding possible bias due to edges of the calorimeter is presented. The background, due mainly to rare fragmentations

of a jet into a leading neutral meson, are subtracted statistically using the expected variation in the longitudinal profile of the electromagnetic shower. The angular distribution in the range of η^* from 0 to 1.5 ($\cos\theta^*$ from 0 to 0.9) is compared to next-to-leading order QCD predictions, and found to be in good agreement.

This dissertation is dedicated to my parents.

Contents

List of Figures . . . . . **xii**

List of Tables . . . . . **xiv**

Acknowledgements . . . . . **xv**

1 Introduction **1**

1.1 Context for the Non-physicist 2

2 Theory **6**

2.1 The Parton Model and Other Essentials 7

2.2 QED Oversimplified 11

2.3 QCD Oversimplified 13

3 The Detector **23**

3.1 Detector Principles 24

3.2 Calorimeter 29

3.3 Muon System 36

3.4 Central Tracking 36

3.5 The Vertex Chamber 38

3.6 The Transition Radiation Detector 39

3.7 The Forward Drift Chamber 40

3.8 The Central Drift Chamber 42

3.9 Trigger 46

3.10 Level 0 47

3.11 Level-1 49

3.12 Calorimeter Trigger 50

3.13 Level-2 51

4 Candidate Event Selection 55

4.1 Reconstruction 56

4.2 Streaming 57

4.3 Standard Cuts 58

4.4 Acceptance 69

4.5 Efficiency as a Function of Angle 74

4.6 Energy scale correction 76

4.7 Jet Reconstruction 76

5 Kinematics 79

5.1 Jet Energy Resolution 79

5.2 Jet η Bias 80

5.3 Reconstructing CM variables 81

5.4 Choosing Jets 83

5.5 Missing E_T cut 89

5.6 Event Selection 89

5.7 Acceptance 91

5.8 Normalization 95

5.9 Details of the Normalization Procedure 102

6 Estimation of the Background 110

6.1 Calorimeter Method 114

6.2 Calculation of the Signal Fraction in the Data 117

6.3 Central Drift Chamber Method 121

6.4 Matrix Formulation 123

6.5 Background Shape 128

7 Results 134

7.1 Conclusions 139

List of Figures

2.1 A schematic view of the parton model- A and B are the proton and anti-proton. 9

2.2 Diagrams of the four basic Feynman diagrams contributing to direct photon production at order $\alpha\alpha_s$. 15

2.3 A cartoon showing the development of two jets from two quarks. 18

2.4 Plot of gluon PDF at two different fragmentation scales. . . . 19

2.5 Plot of u quark PDF at two different fragmentation scales. . . 19

3.1 A cutaway view of the DØ detector. 25

3.2 A cutaway view of the DØ calorimeter. 30

3.3 A schematic view of the liquid argon gap and signal board unit cell. 31

3.4 A schematic view of one fourth of the DØ calorimeter showing the transverse and longitudinal segmentation pattern. 35

3.5 Side view of the DØ central tracking detectors. 38

3.6 A view of the FDC 41

3.7 End view of three CDC modules. 43

3.8 A general overview of the DØ trigger system. 48

3.9 The turn-on curve for the level-1 photon trigger 52

3.10 The turn-on curve for the level-2 photon trigger 54

4.1 The reconstructed energy of monoenergetic $50GeV$ photons after all quality cuts. 60

4.2 Invariant mass of the two highest EM clusters. 62

4.3 The electromagnetic fraction of electron candidates from Z boson decay. 63

4.4 The isolation energy of electron candidates from Z boson decay. 64

4.5 The H-matrix χ^2 of electron candidates from Z boson decay. . 65

4.6 The ionization of tracks near a photon/electron candidate as measured by the CDC. 68

4.7 The position of the primary interaction along the z axis for a sample of direct photon candidate events. 70

4.8 η distribution of photon candidates for different positions of the vertex. 71

4.9 An illustration of how the photon acceptance can be determined. 73

4.10 The Kolmogorov probability as a function of η_{MAX} for different vertex ranges. 73

4.11 The efficiency of the standard photon selection cuts on simulated events. 75

5.1 A diagram of a hypothetical event in the lab frame. 84

5.2 A diagram of a hypothetical event in the center of mass frame. 85

5.3 Number of jets in photon candidate events. 87

5.4 The angle in the transverse plane between the photon candidate and the leading jet. 88

5.5 The $\not{E}_{T\ reco}$ comparison between data and smeared Monte Carlo. 90

5.6 A plot of the η_{boost} vs. η^* for photon candidates constrained to lie within $|\eta_\gamma| < 0.75$ 92

5.7 Regions of flat acceptance in η_{boost} and η^*. 92

5.8 The effect of the minimum p_T cut on the data. 94

5.9 An explicit cut on p_γ^* to assure flat acceptance as a function of η^*. 94

5.10 The observed number of events plotted vs. η^*, from three different regions. 94

5.11 The regions of flat acceptance in η_{boost} and η^* used for the data. 96

5.12 Monte Carlo based theoretical prediction of cross section in the three regions as defined in the text. 97

5.13 Results from Monte Carlo based NLL prediction are shown after being subjected to the same treatment as the data. 98

5.14 Results from Monte Carlo based NLL prediction are shown integrated over a single bin η_{boost} and p_γ^*. 99

5.15 Same as 5.13, but plotted vs. $\cos\theta^*$ 100

5.16 Same as 5.14, but plotted vs. $\cos\theta^*$ 101

5.17 Normalized data plotted in bins of $\cos\theta^*$. 107

5.18 The data in bins of η^* after normalization. 108

6.1 Minimum separation between photons from π^0 and η meson decays. The horizontal line denotes the characteristic cell size in the central region. 112

6.2 The fractional energy deposited in the first layer of the calorimeter for simulated photons and π^0s. 115

6.3 The fractional energy deposited in the first layer of the calorimeter for simulated photons and π^0's. 116

6.4 A plot of ϵ_γ for two different ranges of η as a function of E. Notice the log scale on the x axis. 118

6.5 A plot of ϵ_π and ϵ_π as a function of η. 119

6.6 N_γ/N for Monte Carlo pions and photons over the range of interest for the angular distribution analysis. 120

6.7 The predicted ratio of gluon jets to all jets as a function of $\cos\theta^*$ using the HERWIG Monte Carlo. 129

6.8 Simulated photon data plotted in bins of η^*. 132

7.1 The observed angular distribution of direct photons in the center of mass frame after background subtraction. 136

7.2 Same as Figure 7.1, but binned in $\cos\theta^*$ 138

7.3 Results from an earlier analysis by CDF 139

List of Tables

3.1 Some relevant properties of liquid argon 32

3.2 Some relevant properties of uranium 32

3.3 Some parameters of the Central Calorimeter 33

3.4 Typical energy resolution of the calorimeter 34

3.5 Some parameters of the CDC. 44

4.1 Efficiency of standard photon ID cuts. 66

5.1 Parameters of the jet energy resolution 80

5.2 Parameters of the jet η bias fits 82

5.3 Parameters for regions of flat acceptance 95

5.4 Observed number of events, binned in η^* 103

5.5 Observed number of events, binned in $\cos\theta^*$ 104

5.6 Normalization coefficient 105

5.7 Normalized number of events, binned in η^* 106

5.8 Normalized number of events, binned in $\cos\theta^*$ 109

6.1 Properties of electromagnetic neutral meson decays 111

6.2 Signal Fraction in the Data Sample 121

6.3 CDC Conversion Method Parameters. 127

6.4 Observed number of jet events, binned in η^* 131

7.1 The background subtracted direct photon angular distribution. 137

7.2 The background subtracted direct photon angular distribution. 140

Acknowledgements

First and foremost, I would like to thank my advisor, Prof. Guido Finocchiaro for everything he has done. Without his support, I would not have pursued a doctoral degree. Many thanks also go to the other members of the Stony Brook high energy group, all of whom gave freely of their time, offered useful advice and answer my questions: Professors Rijssenbeek, Engelmann, Grannis, McCarthy and Marx. Special thanks goes to Vito Manzella and Kim Kwee Ng who have always been very helpful, as well as to Joan and Alice, without whose efforts I could not have made it through graduate school. I would also like to thank the members of the photon group who actually did a lot of the work described in this thesis: Steve Linn, John Womersley, Sal Fahey, Bob Madden, Steve Jerger, Wei Chen and Chris Shaffer. I would like to thank Scott Snyder for his efforts in proofreading my thesis. In addition, I owe many things to people too numerous to mention for making my life at Fermilab bearable. And of course I owe thanks to my parents, for their support over the years.

Chapter 1

Introduction

It appears ... a hopeless business, but when you're a graduate student you've got to get your degree, so you keep on going. – Richard Feynman.

The subject of this thesis is an obscure measurement relevant to one facet (direct photons) of a highly specialized sub-field (QCD) of a field (high energy physics) of branch (physics) of systematic effort to understand the the natural world (science). To a large extent this is a testament to the shear volume of scientific knowledge, and the mind-boggling rate at which it has grown in the last century. A century ago, no one could have even imagined the field of high energy physics as we know it today. Even now, the vast majority of people have not the slightest idea as to what high energy physics might be about. In the case that one of the majority should glance at this page, I will first try to put the work presented in this thesis into context at a level that a person with a liberal arts education may understand. The second chapter describes the theoretical motivation and expectations for the angular distribution of photons. Chapter 3 summarizes some relevant aspects of the

experimental apparatus. Chapter 4 explains how and why a small subset of the data collected by the detector is chosen to make the measurement. Chapter 5 explains how the data may be treated to extract the angular distribution of photons. Chapter 6 describes how we separate real photons from other things which may appear almost exactly like photons, and Chapter 7 presents the conclusions.

1.1 Context for the Non-physicist

High energy physics may at first glance appear to be a highly esoteric subject, and yet in some sense, a small child would understand it's basic program – if you want to learn how something works, poke at it a bit and see what happens. Physicists have acknowledged that this is a respectful way of going about the business of learning since Rutherford probed gold foil with a beam of alpha particles, and gave birth to what we now call high energy physics. What Rutherford learned from probing the gold foil was that the atom was made of two separate kinds of "things" (or particles) – the electron (which had been discovered earlier) and the nucleus. In 1932, Chadwick discovered that the nucleus was in turn made out of two kinds of particles – the proton and the neutron. In the meantime, the theory of relativity had erased the line between particles and energy, and quantum mechanics erased the line between radiation and particles, so in the new language of quantum mechanics and relativity, everything could be thought of as a particle. So for example, the atom can be thought of as being made out of electrons surrounding a nucleus,

held together by photons. The nucleus in turn, is composed of neutrons and protons. By combining protons and neutrons, nature can make different nuclei, and by combining them with different numbers of electrons, different atoms. "High energy" physics just means the study of things we don't know how to break apart – yet. Not long ago, the research on protons and neutrons was considered "high energy". That's why sometimes this field is also called "elementary particle physics".

After the war (between 1947 and 1970), lots of new particles were discovered, but Gell-Mann and Zweig were able to make sense of them by proposing that they in turn are made out of particles which he chose to call quarks. These are held together by the whimsically named gluons to make protons and neutrons and other things of the same sort that had been discovered around that time. In other words, Gell-Mann proposed that protons and neutrons are made out of quarks the same way a nucleus is made out of protons and neutrons, the same way as atoms are composed electrons and a nucleus. But it's dangerous to carry the analogy too far. The rules for putting each of these things together are very different, and each is still a vital research area in its own right. Studying atoms has given us lasers and semiconductors, the study of the nucleus has given us fission and someday may give us fusion, while the study of quarks has given us ... well, nothing, yet. But we're just starting!

The area of high energy physics that deals with quarks and gluons is called Quantum Chromo Dynamics, or QCD. This sounds complicated, but it's just an analogy with the theory that explains how electrons and photons interact, called Quantum Electro Dynamics. "Dynamics" just means the theory ex-

plains interactions, "Electro" refers to the to the fact that the interactions the theory describes give rise to what every one already knows as electricity and magnetism. And it's "Quantum" because its based on quantum mechanics, which describes the strange behavior of very small particles. So QCD is the theory that describes the interaction of quarks and gluons that gives rise to the colors we see everyday? No The "Chromo" (color in greek) refers to abstract property quarks and gluons have. Like charge is not anything by itself, it's something some particles have, "color" in this context is not something by itself, it's a property of quarks and gluons that differentiates them from other particles that are not quarks or gluons. QCD is a little hard to explain in a few words, in part because it is *very* strange, like nothing humans have ever experienced before, and that is exactly what makes it very interesting to study.

Before explaining more about quarks and gluons, let's recall how the atom is supposed to work. The electron has a negative charge, the nucleus has a positive charge, the photon can "see" charge, so photons run back and forth between the nucleus and the electrons "telling" them where they are relative to each other, binding them into one unit – the atom. In the same way, gluons can "see" color, and it tells quarks where they are relative to each other, so they can act as a unit– a proton for example. The way we study these particles is by smashing them together and looking to see what comes out, and in what direction. Now the interesting part: quarks have charge *and* color, but gluons have only color. So photons can "see" quarks, but they can't see gluons. This immediately suggests that one way to study QCD is to smash quarks

and gluons together and watch where the quarks and gluons come flying out and how many. Then compare that to where and how many photons come flying out from the same kinds of collisions. This provides complementary information and scientists can learn about quarks and gluons and how they are arranged relative to each other. So the subject of this thesis in plain language might be phrased like this: "The Direction in Which Photons Are Observed When Quarks and Gluons Collide at Very High Energy."

Chapter 2

Theory

The analysis of direct photon production at DØ is motivated by an interest in testing the theoretical predictions for this process and by a desire to extract certain parameters which are not fixed by the theory. Thus, it is important to understand some features and limitations of the way in which calculations are done to arrive at predictions with which the experimental data is compared.

The theoretical framework for describing direct photon production in $p\overline{p}$ collisions rests on two of the three pillars of the Standard Model – perturbative Quantum Chromodynamics (pQCD), Quantum Electrodynamics (QED), augmented by the parton model. In principle, QCD can tells us how gluons and quarks are arranged inside a proton, but in practice, since QCD is non perturbative in this regime, it is currently not possible to calculate the distribution of quarks and gluons from first principles. We are forced to settle for the phenomenological picture offered by the parton model.

2.1 The Parton Model and Other Essentials

The parton model evolved to explain certain features of deep inelastic scattering. Experiments in the 1960's and 1970's revealed that there was a logical structure to the many mesons and baryons that had become known at that time. By making the analogy with studies of the nucleus by inelastic scattering, which could be understood in terms of the *elastic* scattering of the electron with the individual constituents of the whole nucleus, workers at that time argued that the nucleons must in turn be built from some more elementary particles. Thus the study of deep inelastic scattering can be used to provide information about the structure of the nucleons and the properties of their "constituents". [1]

We know now that these are the quarks and gluons described by QCD, but the full complexity of QCD is not needed to build the very simple but very useful parton model. In the parton model, the inelastic collision between (for example) a very energetic proton and anti-proton can be thought of as an elastic collision between a single parton in the proton and a single parton in the anti-proton. This boils down to assuming that the quarks and gluons inside the proton can be considered independently. This assumption is justified by appealing to the impulse approximation: if the time scale of the hard scattering is much shorter than the time scale on which the partons inside the proton interact, then the scattered parton is essentially free, and the structure of the entire proton can be reduced to a function $G_{a/A}(x)$ which denotes the probability of finding parton a in the proton A with a momentum fraction

between x and $x + dx$. We refer to these functions as *parton distribution functions* (PDFs) because they give the probability distribution of partons within the hadron. Then the hard scattering of partons a and b can be described by two body Born scattering. The key here is that since the particles from which partons a and b originate do not "know" anything about the reaction in which a and b may be involved, the parton distribution functions do not depend on the particulars of the hard scattering (at least in the parton model), and we say that they are universal. In other words, $G_{a/A}(x)$ can be measured in one process (for example deep inelastic scattering), and applied to calculate a prediction for a different process (for example direct photon production).

In addition, because strongly interacting quarks and gluons are never observed as free particles in nature, they must somehow recombine to form particles that we do observe. This process is referred to as fragmentation. Thus if we are interested in observing some particular particle, for instance, a energetic photon, we must include a function that gives the probability that a quark or a gluon fragments into a photon. The probability that a particular parton d fragments into a photon with momentum fraction between z and $z + dz$ of the parent parton d is denoted by the function $D_{\gamma/d}(z_\gamma)$. (We are especially interested in the case were z is close to 1, because in such a case we can not distinguish a photon produced directly in the hard scattering from a photon produced by the fragmentation process.) Like the parton distribution functions, this function is universal, and can be extracted from various hard scattering processes. In the parton model, the cross section for inclusive direct photon production in proton – anti-proton collisions can be written as the

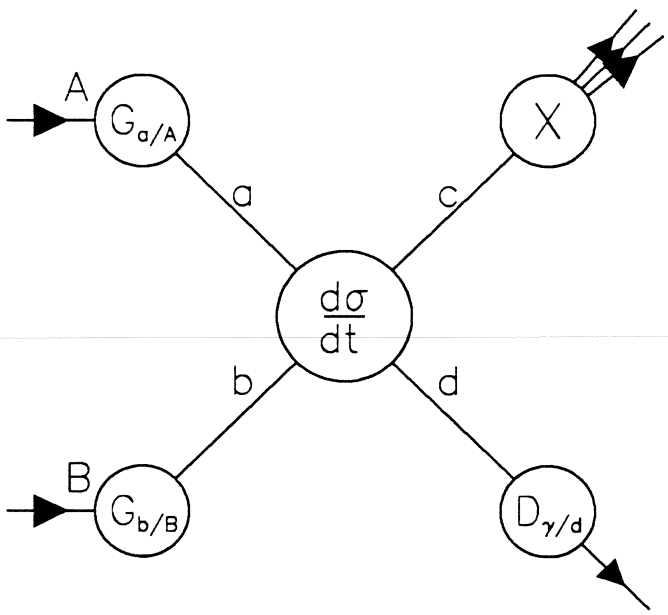

Figure 2.1: A schematic view of the parton model- A and B are the proton and anti-proton. X represents the particles that are integrated over in the final state to obtain a semi-inclusive cross section.

incoherent sum of all the possible sub-processes [2]:

$$E_\gamma \frac{d\sigma}{d^3 p_\gamma}(p\bar{p} \to \gamma + X) =$$

$$\sum_{a,b,c,d} \int dx_a dx_b dz_\gamma G_{a/p}(x_a) G_{b/\bar{p}}(x_b) D_{\gamma/d}(z_\gamma) \frac{\hat{s}}{z^2 \pi} \frac{d\hat{\sigma}}{d\hat{t}}(ab \to cd) \delta(\hat{s} + \hat{t} + \hat{u}). \quad (2.1)$$

We can represent this equation schematically as shown in Figure 2.1.

Here, the variables $\hat{s}, \hat{u}, \hat{t}$ are the Mandelstam variables in the center of mass frame of the partons and the delta function enforces conservation of

energy and momentum. We can define these and several other useful variables as follows. Let p_A and p_B be the four momentum of proton and anti-proton. Then

$$s = (p_A + p_B)^2,$$

and the momenta of the partons can be written (assuming massless partons, and ignoring any transverse momentum they may have) as

$$p_a = \frac{x_a\sqrt{s}}{2} \quad \text{and} \quad p_b = \frac{x_b\sqrt{s}}{2}$$

If the produced photon has transverse momentum p_T and rapidity y, then its four momentum can be written

$$E_\gamma = p_T \cosh(y) \quad \text{and} \quad p_\gamma = p_T(\cos(\phi), \sin(\phi), \sinh(y))$$

where y is the rapidity, defined as

$$y = \frac{1}{2}\ln\frac{E + p_z}{E - p_z} = \tanh^{-1}\frac{p_z}{E}$$

(here p_z is the momentum along the z axis). For massless particles this reduces to this very useful form:

$$y = -\ln\tan\left(\frac{\theta}{2}\right)$$

For massive particles, this quantity is called pseudorapidity η. In what follows, we will always assume massless particles, but we will use η for the most part to remind us that we are making the massless approximation. Finally, we define the Mandelstam variables in the center of mass frame as

$$\begin{aligned}
\hat{s} &= x_a x_b s & \hat{u} &= -x_b p_T\sqrt{s}e^y & \hat{t} &= -x_a p_T\sqrt{s} \\
\hat{s} &= (p_a + p_b)^2 & \hat{u} &= (p_c - p_b)^2 & \hat{t} &= (p_c - p_a)^2 \\
& & \hat{u} &= -\tfrac{\hat{s}}{2}(1 + \cos\theta^*) & \hat{t} &= -\tfrac{\hat{s}}{2}(1 - \cos\theta^*).
\end{aligned}$$

In the parton model, the scattering is neatly divided into a "soft" part represented by the parton distribution functions and the fragmentation functions on the one hand, and the "hard scattering" on the other. The success of the parton model relies on the phenomenological observation that the parton distribution functions are universal (that is the same for any process) and depend only of x (this property is referred to as scaling.) However, in QCD there is no such neat division, and there is no reason to expect scaling. For the moment, let's take the parton model at face value and consider the description of the hard scattering process denoted by $d\hat{\sigma}/d\hat{t}$. Such a description must include not only QCD, but also QED, because the photon interacts only electromagnetically.

2.2 QED Oversimplified

QED is a local gauge theory with U(1) as the gauge group. The gauge boson of the theory is the photon, which mediates interactions between charged particles. Because the photon is not itself charged, the photon does not couple to itself. The essential tools of QED were developed in the years immediately after World War II, especially after the realization that QED was renormalizable. This is a key ingredient in the success of QED specifically and all field theories in modern particle physics in general. This is so because in quantum field theory, a naive calculation of observable quantities will routinely give un-

physical infinities. Essentially such infinities occur when Feynman graphs with "loops" are included in the calculation, as in principle they should be. The problem is that this introduces integrals over the momentum in the loop, and the integral diverges. So in order to get sensible answers, one must somehow get rid of these infinities. Renormalization is the process of "taming" these infinities. [1]

Since the time when QED was first shown to be renormalizable it has achieved astounding success in describing the observed features of Electromagnetism. However, the QED content of direct photon production is not directly interesting. It is understood well enough that the study of this process at the Tevatron is very unlikely to shed any additional light on the subject. This understanding of QED is what makes direct photon production an interesting process to study– by making it easier to calculate higher order QCD corrections and by reducing the total number of subprocesses that have to be considered. The result is that historically the theoretical predictions (based on perturbative calculations) available for direct photon production are more accurate (done to a higher order) than those available for a process like inclusive jet production, although this situation is now changing.

Historically, QED has served as the model for QCD, so they share much of their language, but QCD is more complicated. QCD is a gauge theory which describes the interactions of quarks and gluons, with SU(3) as the gauge group and gluons as the gauge bosons. [3]. There are three colored quarks of each flavor and eight gluons. Any reasonable description of QCD is well beyond the scope of this work, but a brief description of some of the essential features

may help the reader gain insight into the physics motivation for studying direct photons, and some of the challenges such studies entail.

2.3 QCD Oversimplified

The interactions of quarks and gluons are known as strong interactions, and the coupling constant, $\alpha_s(q^2)$ can become quite large (above one) at low energies, and this renders the use of weak coupling perturbation theory, like that used in QED, meaningless at low energies. However, the theory was given a tremendous boost with the discovery of asymptotic freedom, and it has proven to be very useful in the description of strong interactions at high energies. [3]

The classical QCD Lagrangian is

$$\mathcal{L} = -\tfrac{1}{4} F_a^{\mu\nu} F_{a\mu\nu} + \overline{\psi}_j (i\gamma_\mu D^\mu_{jk} - M_j \delta_{jk}) \psi_k \tag{2.2}$$

where

$$D^\mu_{jk} = \delta_{jk}\partial^\mu + ig(T-a)_{jk} G^\mu_a \tag{2.3}$$

$$F_a^{\mu\nu} = \partial^\mu G^\nu_a - \partial^\nu G^\mu_a - g f_{abc} G^\mu_b G^\nu_c \tag{2.4}$$

where $a = 1, \ldots, 8$ and $j, k = 1, 2, 3$ are the color indices for gluons and quarks, respectively. $F_a^{\mu\nu}$ is the gluon field tensor and D^μ_{jk} is the covariant derivative acting on a quark field. The f_{abc} are the structure constants of SU(3), M is the mass matrix, and g is the strong coupling constant. If we think in terms of the analogy with QED, we notice that the gluon field tensor differs from

the electromagnetic field tensor $F^{\mu\nu}_{QED} = \partial^\mu A^\nu - \partial^\nu A^\mu$ by the addition of a term that couples gluons to gluons. This is one of the hallmarks of QCD. It makes QCD matrix elements more difficult to calculate (compared to QED) – at least in part because at a given order there can be many more diagrams. Once again, this underscores the advantage of the direct photons production process versus a "pure" QCD process such as inclusive jet production. For example, there are eight subprocesses to be considered at the lowest order for the process $\overline{p}p \rightarrow \text{jet} + X$, but only two for the direct photon production, $\overline{p}p \rightarrow \gamma + X$. [2] The two subprocesses for direct photon production are $qg \rightarrow q\gamma$ and $q\bar{q} \rightarrow g\gamma$, which gives four basic diagrams when all the possible combinations are considered. The diagrams are shown Figure 2.3.

Another important difference between QCD and QED is that the strengths of their coupling constants evolve in different directions. The fact that coupling "constants" evolve at all is a startling result of the theory and is intimately related to the procedure by which the theory is renormalized. As mentioned above, renormalization is the procedure by which the predictions of a theory are made finite, in spite of diverging loop integrals. The procedure involved can be thought of as reabsorbing the infinities into the the formal parameters of the theory – the masses of the quarks and the coupling constant. The theory than depends on the renormalized masses and coupling constant. Such procedures also have the side effect of introducing a cut-off parameter on which the predictions made by the theory depend. That is, the basic parameters of the theory, such as the coupling constant now become an explicit

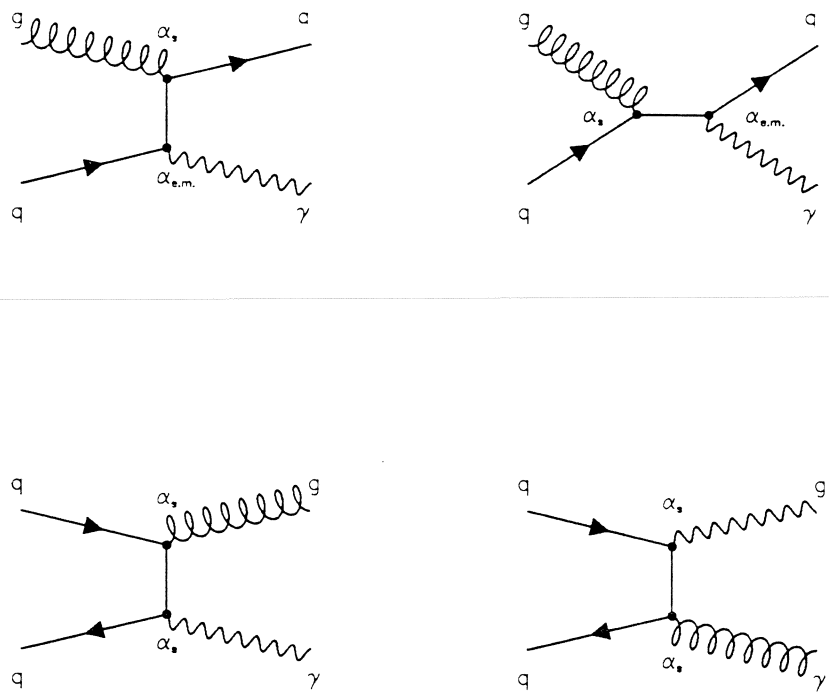

Figure 2.2: Diagrams of the four basic Feynman diagrams contributing to direct photon production at order $\alpha\alpha_s$. The top diagrams are Compton scattering, and the bottom diagrams are the annihilation diagrams.

function of some dimensional scale parameter μ : $\alpha_s = \alpha_s(\mu)$. However, we insist that observable physical quantities can not depend on the scale parameter, and this in turn implies that the formal parameters of the theory must depend on μ in a particular way. The result is that it is possible to derive the function that describes how $\alpha_s(\mu)$ changes with the momentum scale of the scattering. In QCD, its slope in μ is negative. That is, the renormalized

coupling constant decreases as the momentum scale of the process increases. And in fact, $\alpha_s \to 0$ as $\hat{t} \to \infty$. This situation is opposite from that found in QED. In QED the renormalized coupling constant *increases* with increasing energy. This can be understood heuristically in terms of the gluon self interaction. Because a virtual gluon can radiate another gluon and become less virtual, QCD becomes dominated by processes that involve many soft gluons if we allow enough time for such radiation to happen. In QED, on the other hand, a virtual photon can not radiate other photons, but it can decay into virtual fermion pairs, and this produces a screening effect which becomes less important at small scales, and therefore, higher order corrections are more important at higher energies. In a nutshell, the message the running coupling has for us is that in QED, higher order corrections are more important at high energy than at low energy, while in QCD, higher order corrections are more important at low energy. The asymptotic decrease in the renormalized strong coupling to zero as Q^2 increases is what is referred to as asymptotic freedom.

On the other hand, the increase in α_s at low momentum scales is responsible for binding quarks and gluons into colorless objects such as hadrons. The result is that quarks and gluons are never observed in isolation. In high energy collisions, a gluon or quark with large momentum in the final state must "hadronize" into a "jet" of particles that are only roughly collinear with the outgoing parton. This process is not easily amenable to calculation, because it is intrinsically non-perturbative. However, we can make some qualitative arguments about the process based on the idea of confinement. Because gluons carry color, the force between two colored objects, for instance a pair of

quarks as in Figure 2.3, does not decrease with the distance between them but instead remains approximately constant. The result is that the energy of the gluons between the two quarks grows, and when the energy is large enough, a new quark antiquark pair is created. This process continues until the relative momenta of the quarks becomes small enough that colorless hadrons are created. [4] This introduces a large uncertainty in any experimental attempt to associate the measured jet with the parton from which it originated. It is especially difficult to determine the energy of the original parton, but somewhat easier to estimate its direction. A great of deal of work is now in progress in this area [5], and we may look forward to improved understanding of jet formation in the future, but for the moment, this is an area of experimental and theoretical difficulty. This is yet another reason that photons are a preferred probe for testing QCD. The photon provides a *direct* probe of the hard scattering.

However, it is alway important to remember that all of the above must be thought of in the context of perturbation theory. If one were mathematically powerful enough to calculate the theory to all orders, one would always get the correct result, independent of the choice of scale μ. This works like a handicap: the better one is at calculating, the less one relies on the crutch of sweeping the higher order corrections into the renormalized coupling constant, and the less ones answer will depend on the choice of μ. Thus, the sensetivity of a particular calculation on the choice of μ can be taken as an estimate of the uncertainty in the theoretical prediction.

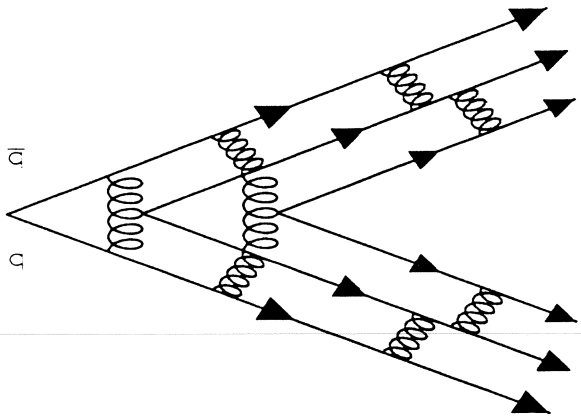

Figure 2.3: A cartoon showing the development of two jets from two quarks.

The situation is reminiscent of the parton model, since the calculation is again divided into a calculable part and a part which must be extracted from experiment. Is there a relationship? The answer is yes; we can now understand the phenomenologically motivated parton model as leading order QCD. The separation between the "hard" scattering and the "soft" PDF's now should be seen as somewhat arbitrary. This introduces a new scale into the problem, λ, which is the scale which separates the hard scattering from the PDF's. That means that now we will have PDF's which depend on some scale and on x. So now, $G_{a/A} = G_{a/A}(x, \lambda)$ as well as $\alpha_s = \alpha_s(\mu)$. This rather untidy situation is not quite as bad as it appears, because there is a natural scale for λ and μ, the momentum exchange for the process Q^2. It it natural and common to set $\lambda^2 = \mu^2 = Q^2$ in a given process. However, in order to make predictions,

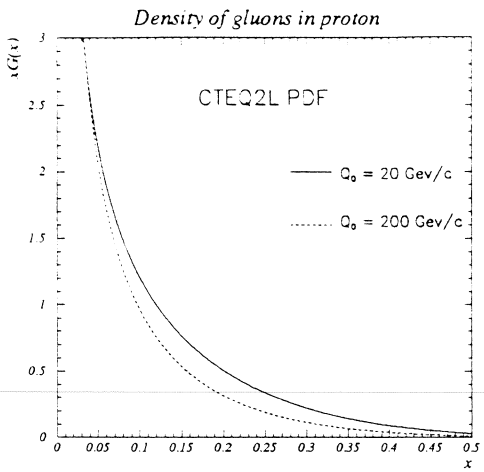

Figure 2.4: Plot of gluon PDF at two different fragmentation scales.

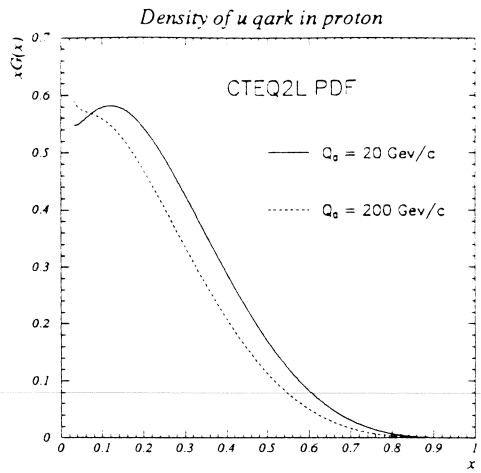

Figure 2.5: Plot of u quark PDF at two different fragmentation scales.

we must have a way to "evolve" the PDF's to any desired scale. This can be done in a spirit simular to the way one derives the dependance of $\alpha_s(\mu)$ on μ. The evolution equation is referred to as the Gribov-Lipatov-Alterelli-Parisi evolution equation (GLAP) and it allows us to calculate how the parton distribution functions evolve with Q^2 if they are specified at some $Q^2 = Q_0^2$ which is sufficiently large such that $\alpha_s(Q_0^2) \ll 1$ and a perturbative expansion in the coupling constant is possible. [6]

Figures 2.3 and 2.3 shows the PDFs for gluons and u-type quarks for two different scales of the exchanged momentum. The distributions have been extracted by making a fit to several different experiments using leading order QCD calculations by the CTEQ collaboration. [7]

Now consider briefly what qualitative features we would expect from QCD

for direct photon production in $p\overline{p}$ at $\sqrt{s} = 1800\,\mathrm{GeV}$ with a typical photon $E_T \approx 30\,\mathrm{GeV}$. First, we notice from the definition of $\hat{s}$ given earlier, that if the photon is produced near $\eta = 0$ (so that $E_T \approx E_\gamma$ and $\hat{s} = 4E_\gamma^2$) then $x_a \approx x_b \approx .035$. This is a relatively low x, and the partons most likely to carry such a small fraction of the proton momentum are gluons. From the diagram, we can estimate that at this x we are about five times more likely to find a gluon than a quark. We can therefore conclude that the dominant sub-process will be $qg \rightarrow \gamma q$,which is the so-called Compton diagram (illustrated in the top two diagrams of Figure 2.3). However, if one of the initial partons has a momentum fraction $x \geq 0.2$ it is more likely to be a quark than a gluon. We can look up the parton level two-body differential cross sections $d\hat{\sigma}/d\hat{t}$: [2]

$$gq \rightarrow \gamma q \qquad -\frac{\pi\alpha\alpha_s e_q^2}{3\hat{s}^2}\left[\frac{\hat{t}}{\hat{s}} + \frac{\hat{s}}{\hat{t}}\right] \tag{2.5}$$

$$q\overline{q} \rightarrow \gamma g \qquad \frac{8\pi\alpha\alpha_s e_q^2}{9\hat{s}^2}\left[\frac{\hat{u}}{\hat{t}} + \frac{\hat{t}}{\hat{u}}\right] \tag{2.6}$$

$$gg \rightarrow gg \quad \frac{9\pi\alpha_s^2}{2\hat{s}^2}\left[3 - \frac{\hat{t}\hat{u}}{\hat{s}^2} - \frac{\hat{s}\hat{t}}{\hat{u}^2} - \frac{\hat{s}\hat{u}}{\hat{t}^2}\right] \tag{2.7}$$

where e_q is the quark fractional charge. We note the t channel pole in the cross section for the Compton process. This gives a characteristic growth in the cross section as $1/(1 - \cos\theta^*)$, but only when the photon is moving along the direction of the quark. The annihilation cross section, on the other hand is symmetric, and also exhibits $1/(1 - \cos\theta^*)$ growth. Compare this with the cross section for purely hadronic interactions, which will be dominated by $gg \rightarrow gg$ because gluon PDF dominates at low x. Here again, there is a pole

at small $\hat{t}$, but it grows much faster as $1/(1-\cos\theta^*)^2$, when $\theta^* \to 0$, and it is symmetric about $\cos\theta^*$ (as it must be, since the two gluons are identical.) However, the major difference is that this cross section is much larger than direct photon production. We can estimate how much larger by noticing that α_s is about 15 times larger than α_{em} at these energy scales. Another factor of six comes from the difference in PDF density between gluon and quark and another factor of ten from the color factor and quark charge. In looking at the expressions for the cross sections, the value inside the parenthesis is about the same or slightly less for the $gg \to gg$ case because for $\eta \approx 0$, we have $\hat{s}/2 = -\hat{t} = -\hat{u}$. The result is that the jet cross section is three orders of magnitude larger than the direct photon cross section. In order to be able to extract the direct photon signal from the overwhelming jet background, the experiment must have excellent rejection against jets and an accurate means of determining the unavoidable residual contamination. This is the major drawback of using the photon signal, and any experiment with direct photons must deal with this topic extensively.

In practice, the full QCD predictions for the photon cross section and angular distribution are very complicated, because they must consider the acceptance of the detector and possible isolation cuts. The simplest, most flexible way to do this is by use of the Monte Carlo technique. In other words, the integration required to arrive at a prediction for some given observable is done by generating parton four vectors randomly over phase space, calculating a weight for the given configuration and by summing weight only for those configurations that fall in the regions of interest. Notice that such a program

is not an event generator– each iteration in itself can not be thought of as an "event" that we observe with a detector, even though there is a set of four vectors associated with each. The problem is the weight. In nature, we always either observe some given event, or we don't: the events are not weighted. In this analysis we use the program by Baer, Ohnemus and Owens to study the theoretical expectations. [8] This program includes not only the two to two subprocesses at leading order, but it also treats $2 \rightarrow 3$ subprocesses as well as one loop corrections to the two body cross section.

One more point is worth making. Because QCD requires the use of an arbitrary scale, there should only be one large scale in the problem. If there are two large scales, the assumptions used to arrive at GLAP equation may not be valid, and the results of calculations using this formalism may become unreliable. Such a situation may result if we allow θ^* to become small because then

$$\hat{t} = \frac{\hat{s}}{2}(1 - \cos\theta^*) \approx \frac{\hat{s}}{4}\theta^{*2}$$

and $\hat{t} \ll \hat{s}$. In such case, we can expect that the theoretical predictions will become less accurate, and may depend strongly on the scale parameter, μ. We can use the theoretical Monte Carlo program not only to derive a prediction for the angular distribution, but to see this dependence on the scale parameter, as well the effects of including the Next-To-Leading order contributions.

Chapter 3

The Detector

At the heart of high energy experimental physics is the detector. Very large general purpose detectors, like the DØ detector are extremely complicated. It is fair to say that no one person has a good understanding of all the various components of the detector, it's support equipment, the various systems for control and data acquisition. However, for the interested reader, many excellent descriptions are available, at different levels of detail. [9] serves as the "official" reference and a relatively detailed description of all the components and major systems. Other useful references are [10] for the Data AcQuisition system (DAQ), [12] for the Central Drift Chamber (CDC), [11] for the Forward Drift Chamber (FDC), [13],[14] for the calorimeter and many others. In view of the great volume and quality of the available literature, the description presented here will be limited to a thumb-nail sketch of the detector, with emphasis placed only on the components used for this analysis.

The DØ experiment is optimized for the study of high mass states and large P_T phenomenan, such as the top quark, W and Z bosons and pertur-

bative QCD. The heart of the detector is a thick sampling calorimeter based on detection of ionization in liquid argon. The calorimeter is subdivided in three cryostats. Inside the calorimeter is a compact non-magnetic tracking volume composed of four separate detectors, each optimized for unique duties. Outside the calorimeter is a muon detector with thick magnetized iron toroids surrounded by three "super" layers of proportional wire chambers.

The experiment uses a right handed coordinate system, with the z axis along the proton direction and the y axis pointing upward. The azimuthal angle, ϕ is measured from the x-axis, and the polar angle, θ is measured from the positive z axis. An overview of the detector is shown in Figure 3.1.

3.1 Detector Principles

Before embarking on a detailed discussion of some particular detector, it is useful to quickly summarize some of the relevant physics. Different detectors take advantage of different aspects of the interactions of particles with matter, and have various advantages and disadvantages. This section is meant to motivate the different kinds of detectors by highlighting the different aspects of physics they are designed to exploit, and explain some of the terminology used.

When an energetic ($\gamma \geq 4$) charged particles move through material, they interact primarily through Coulomb scattering with the atomic electrons and slowly deposit energy at a characteristic rate that is only weakly dependent on

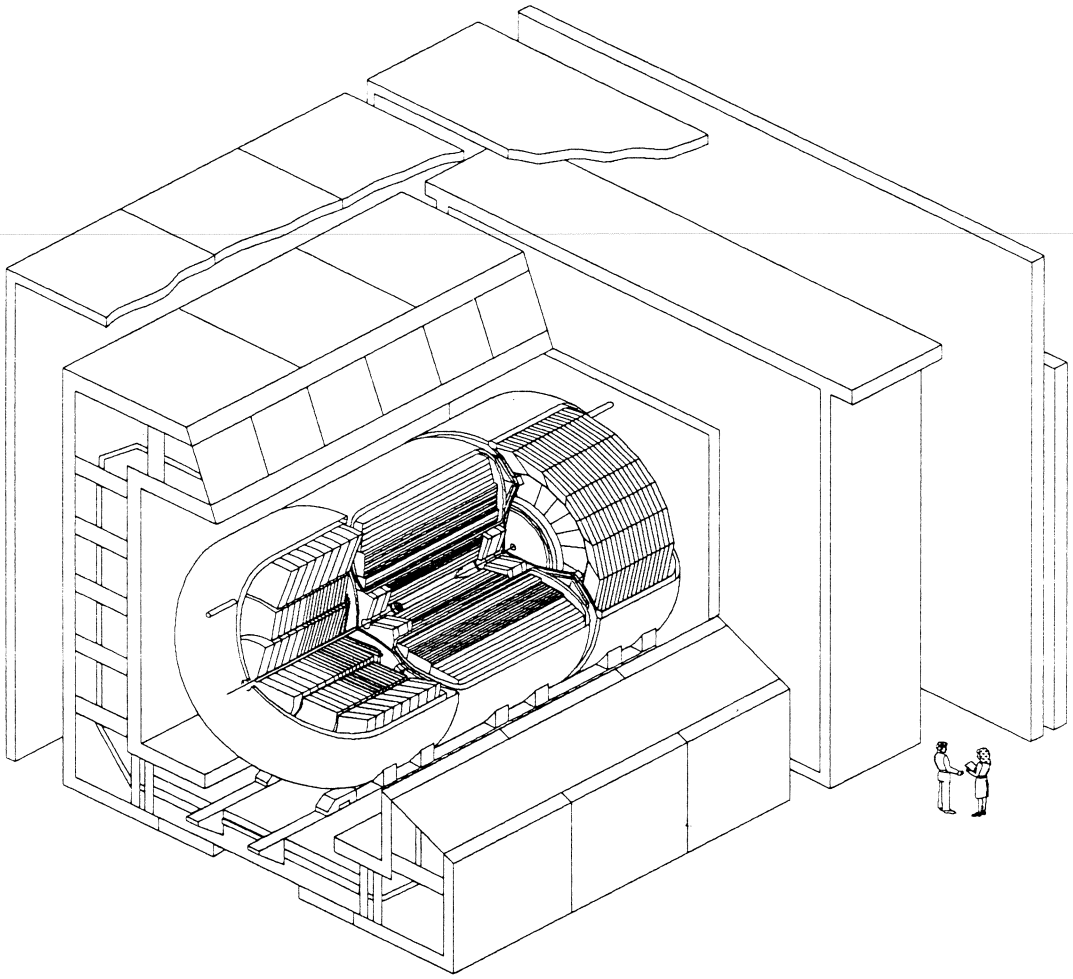

DØ Detector

Figure 3.1: A cutaway view of the DØ detector.

the particle or the material at a rate of roughly 1.5 to 2 MeV/g cm^{-2}. Such particles are called minimum ionizing (MIP). Although the energy loss per ionization event is quite small on the average, there are very many such events, even in material as tenuous as air. For example, MIP typically leaves about 100 electron-ion pairs in its wake per cm of argon at atmospheric pressure. This leaves a characteristic track of ionization that can be detected to precisely determine the path taken by the ionizing particle.

Although the Coulomb scattering is the most frequent process, much rarer interaction, in which the particle loses a large fraction of its energy can contribute significantly to the total energy loss. Such considerations are especially important for electrons because of their very low mass. For high energy electrons, the dominant energy loss mechanism is bremsstrahlung, whereby an electron may lose an important fraction of it's energy by radiating photons, and the photons can carry a large fraction of the electrons energy. Because the energy loss for high energy particles can be treated as a constant in many circumstances, we can define a very useful variable for describing energy loss by charged particles – the *radiation length*, X_0. It is defined by

$$\frac{dE}{E} = -\frac{dx}{X_0}. \tag{3.1}$$

So that a MIP losses approximately 2/3 of its energy after one radiation length.

The energy at which radiation loss becomes larger than energy lost to ionization is known as the critical energy. It varies inversely with Z, and can be approximated as

$$E_c \approx \frac{800\text{MeV}}{Z + 1.2}. \tag{3.2}$$

In addition, photons, which do not leave an ionized track like charged particles, may interact in the strong electric field near the nucleus to pair-produce. (Pair production is a process where a high energy photon converts into a low mass electron-positron pair). Pair production, sometimes also called photon conversion is related closely to the bremsstrahlung process and is characterized by the same length scale X_0. The mean free path for a photon is found to be [15]

$$\lambda_{pair} \approx \frac{9}{7} X_0. \tag{3.3}$$

Notice that for thin (in terms of radiation length) detectors, the preceding two processes do not contribute significantly, except for a small fraction of electrons, and thus the electrons leave energy primarily through collision with atomic electrons, the same as heavier particles. The resulting trail of ionization can be detected and used to accurately determine the direction and position of the particles crossing the detector. Devices of this type are tracking detectors.

The relationship between bremsstrahlung and pair production means that when an energetic electron moves through several radiation lengths of high Z material, it repeatedly produces energetic photons by the bremsstrahlung process, the photons in turn pair produce, and the resulting electrons bremsstrahlung again, and so on until the energy per electron falls below the critical energy. This cascade of particles is what is referred to as an electromagnetic shower. The number of particle in the shower grows at first, then declines. At its peak, the electromagnetic shower produces $N_{max} \approx E_0/E_c$ particles (where E_0 is the energy of the incident electron or photon and E_c is

the afore mentioned critical energy). The maximum energy deposition occurs at a depth of

$$t_{max} \approx \log(E_0/E_c) + 0.5 \quad \text{for photon induced showers} \tag{3.4}$$

$$t_{max} \approx \log(E_0/E_c) - 0.5 \quad \text{for electron induced showers} \tag{3.5}$$

The lateral extent of the shower is given by the *Moliere radius* defined as

$$R_M = \mathrm{X}_0 \frac{21.2\mathrm{MeV}}{E_c} \tag{3.6}$$

Most of the shower (about 90%) is contained within 2 R_M of the shower axis. Because of this showering phenomenon, the energy of a high energy electron/photon can be contained in a relatively small volume, especially if the detector uses high Z materials. This is the principle on which total absorption electromagnetic calorimeters are built.

For energetic hadrons, strong interactions with the nucleus are the dominant energy loss mechanism. The typical interaction involves multiple particle production with an average transverse momentum of 0.35 GeV/c. Producing mostly fast pions and nucleons, which in turn undergo similar interactions. Thus a hadronic cascade is formed in analogy to the electromagnetic shower described above. [16] The variable roughly equivalent to X_0 for describing hadronic showers is the nuclear absorption length λ which can be approximated as

$$\lambda \approx 35\mathrm{A}^{1/3} \tag{3.7}$$

However, hadronic showers are more complicated than electromagnetic showers

and not as easily described. There are several features of hadronic showers which limit the performance of hadronic calorimeters:

- Statistical fluctuations. The energy loss per interaction is relatively large, which results in fewer particles, and fewer interactions within the shower. As a result, hadronic showers suffer from large statistical fluctuations.

- Invisible energy. A significant fraction of the energy in a hadronic cascade is lost to nuclear excitation and break up, which may not be detectable.

- Neutrons may move far from the core of the shower and they may also be captured by nuclei and thus be lost from the shower.

- π^0/π^+ ratio. π^0's, once produced, decay very rapidly into two photons which form an electromagnetic shower. This ratio is subject to large fluctuations, and because of effects listed above, real detectors do not respond equally to electromagnetic and hadronic showers, and this introduces additional fluctuations in the measured energy of the shower.

3.2 Calorimeter

Because there is no magnetic field in the DØ detector, the calorimeter carries most of the burden of identifying electrons, photons and jets, and provides the only energy measurement for these objects. It also serves to establish transverse energy balance in events without muons. On the other hand, the lack of a magnet and the corresponding small size, allows the calorimeter to

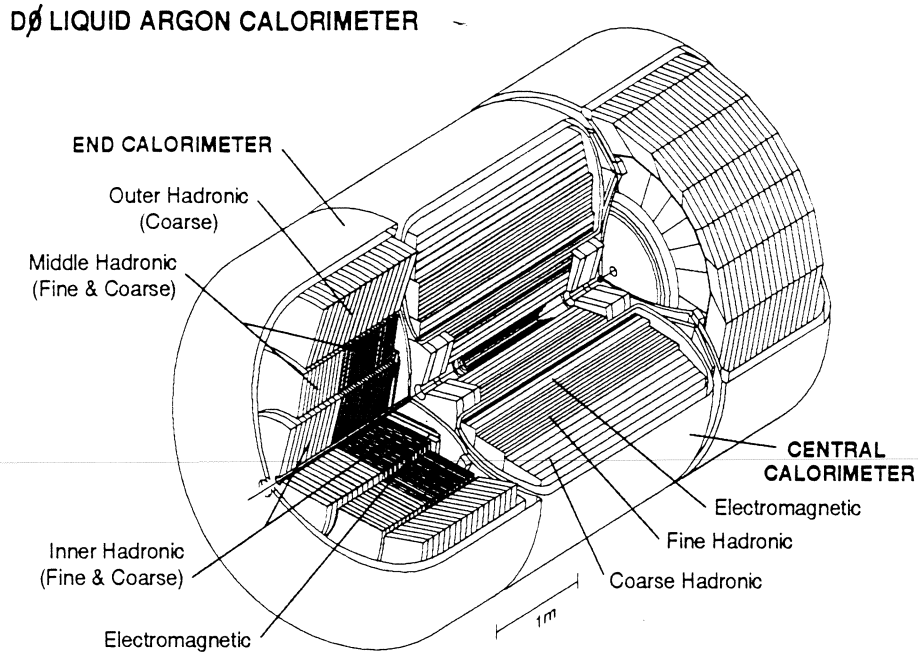

Figure 3.2: A cutaway view of the DØ calorimeter.

be more finely segmented, thicker, and more hermetic than would be possible with a larger device. As mentioned earlier, the calorimeter is divided into three cryostats in order to give access to the tracking volume: Central Calorimeter (CC), End Calorimeter South (ECS) and End Calorimeter North (ECN), often called simply EC when the distinction between North and South is unnecessary. Inside the cryostat, the calorimeter is organized in depth into electromagnetic (EM), fine hadronic (FH) and coarse hadronic (CH) section, as shown in Figure 3.2. In the CC, the sections consist of 32 EM modules and 16 FH and CH modules. Except for the smallest angles, the EC is also built up of 16 and 32 modules. Unfortunately, in the CC this means that there are unavoidable cracks which affect energy measurement for photons and electrons close to the module edge.

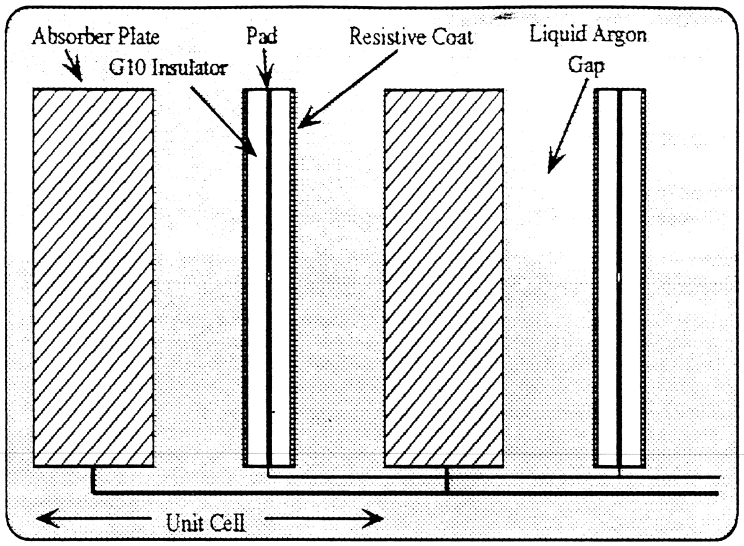

Figure 3.3: A schematic view of the liquid argon gap and signal board unit cell.

The DØ calorimeter is of the liquid argon sampling type, which means that it uses plates of high Z, high density absorber interspersed with gaps of liquid argon ionization chambers to "sample" the shower. This arrangement is illustrated in Figure 3.3. By applying high voltage to the gap between absorber plates and readout pads, the charge caused in the liquid argon by the particles of the shower may be collected. The advantages of such an arrangement result in a compact calorimeter able to stop all but the highest energy jets and all electrons and photons. The disadvantage is that only a small fraction of the actual energy of the shower is measured, which degrades energy resolution.

Some of the useful properties of using liquid argon as a sampling medium are described in [17] The relevant properties of liquid argon are listed in Table 3.1.

Table 3.1: Some relevant properties of liquid argon

Density	1.4 g/cm^3
Electron mobility	5mm/μs at 1KV/mm
Radiation length	13.5cm
Nuclear absorption length	84cm
Gap thickness	2.3mm
High voltage	2.0KV

Table 3.2: Some relevant properties of uranium

Z	92
Density	19g/cm^3
Radiation length	0.32cm
Nuclear absorption length	10.5cm
Plate thickness	3mm CC and 4mm EC

Because the radiation length X_0(g/cm^2) scales as very roughly 1/Z [16] (p.260) but the nuclear absorption, it is useful to make the absorber using a material with as high a Z as possible, in order to better distinguish between electromagnetic and hadronic showers, at least in the electromagnetic section of the calorimeter. DØ uses uranium as the absorber in the EM and FH sections and some of its properties are listed in Table 3.2. Copper is used as the absorber in the CH section of the CC and steel is used in the coarse hadronic sections of the EC.

The design of the calorimeter allows for fine segmentation. Groups of

Table 3.3: Some parameters of the Central Calorimeter

Section	EM	FH	CH
Rapidity coverage (η)	± 1.2	± 1.0	± 0.6
Number of Modules	32	16	16
Absorber and thickness	3mm U	6mm U	46.5mm Cu
Number of ionization cells	21	50	9
Number of readout layers	4	3	1
Cells per readout layer	2,2,7,10	20,16,14	9
Total radiation length (X_0)	20.5	96.0	32.9
Total nuclear absorbtion lengths (λ)	.76	3.2	3.2
Sampling fraction	11.8%	6.8	1.45

individual readout pads are ganged into cells to reduce the total number of readout channels. The segmentation in depth is used to help differentiate between hadronic and electromagnetic showers, as well as to locate the depth at which electromagnetic showers start, in order to differentiate between photon and π^0 induced showers. The details of the longitudinal segmentation and some other parameters of the CC are summarized in Table 3.3. The segmentation in the EC is very similar. [9]

For analysis and triggering purposes the calorimeter is segmented into readout towers in η and ϕ. The size of the readout cells in the transverse dimension was chosen to be comparable to the size of the shower and utilizes 'pseudo-projective' towers, so called because the centers of the cells in a tower lie on rays projecting from the center of the detector, but the cell boundaries

Table 3.4: Typical energy resolution of the calorimeter

Particle	Constant	Sampling	Noise
e^-	.003	$0.16\sqrt{GeV}$	$0.14GeV$
π^+	.032	$0.41\sqrt{GeV}$	$1.28GeV$

are aligned perpendicular to the absorber plates. The size of the readout towers is $.1 \times .1$ in $\eta - \phi$ throughout most of the calorimeter. In addition, cells located around shower maximum are segmented twice as finely in ϕ and η to allow more precise location of the EM shower centroids and to help differentiate between the transverse profiles from electrons, photons and pions. The segmentation of the calorimeter is shown in Figure 3.4.

The performance of the calorimeter has been measured extensively at the test beam and at the DØ interaction region. [19], [20], [14] The energy resolution is parametrized as

$$\left(\frac{\sigma}{E}\right)^2 = C^2 + \frac{S^2}{E} + \frac{N^2}{E^2}. \tag{3.8}$$

C is constant term, caused by errors in calibration, S is the sampling term, due to the statistical nature of the shower, and N is the noise term. Typical values for electrons and pions are listed in Table 3.4

The position resolution of the shower centroid for electrons is found to be about 1mm at 50 GeV and to vary as $1/\sqrt{E}$. [21],[22]

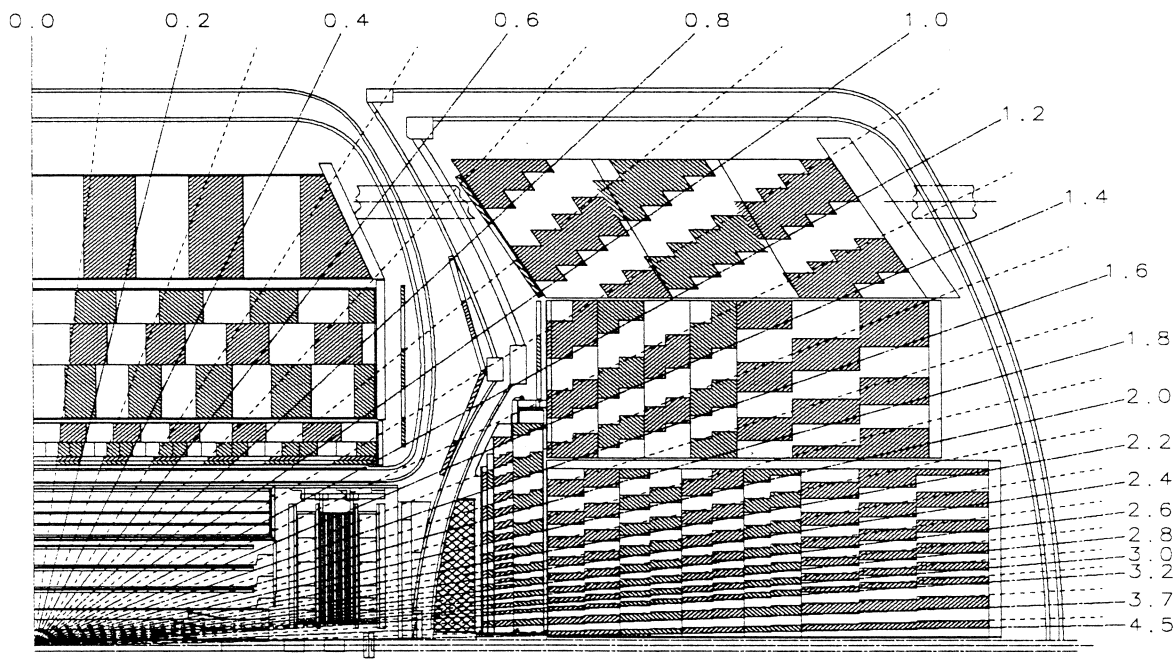

Figure 3.4: A schematic view of one fourth of the DØ calorimeter showing the transverse and longitudinal segmentation pattern. The shading pattern indicates the distinct cells for the signal readout. The rays indicate the psedorapidity intervals seen from the center of the detector.

3.3 Muon System

The calorimeter is surrounded by the muon system. The muon system is not used in the analysis described here, so the description is very brief. The DØ muon system consists five magnetized iron toroids which are surrounded by three layers of Proportional Drift Tubes (PDTs). At DØ the thick calorimeter combined with the rather thick toroid combine to give at least 13 nuclear absorption lengths over most of the detector. The advantage of this is that it is very unlikely that any charged particle that makes it through the detector is anything but a muon. The disadvantage is that multiple scattering, combined with the lack of central magnetic field seriously limits the momentum resolution of the muon system. The resolution is parametrized as

$$\left(\frac{\delta P}{P}\right)^2 = (0.18)^2 + (0.01P)^2. \tag{3.9}$$

3.4 Central Tracking

The space between the interaction point and the calorimeter is filled with detectors designed to detect and accurately measure the tenuous tracks of ionized gas left in the wake of an energetic subatomic particle. There are four separate detectors which constitute the central tracking system: the Vertex Drift Chamber (VTX) designed for maximum spatial resolution and positioned as close as possible to the interaction point. Surrounding the VTX is the Transition Radiation Detector, (TRD) designed to aid in electron identification. Next in radius is the Central Drift Chamber, (CDC) designed to

match electron tracks from the interaction vertex to the calorimeter shower. It is complemented in the forward region by a close relative, the forward drift chamber. Figure 3.5 shows the arrangement of the tracking chambers. With the exception of the TRD, the tracking chambers in DØ are drift chambers. Principles of drift chamber operation are described in detail in an excellent book by Blum and Rolandi. [18] Here we present only the barest outlines, the minimum necessary to address the features directly relevant to the analysis of direct photons. A drift chamber can be thought of as composed of a drift region followed by an amplification region. The drift region is established by applying a voltage of a few hundred volts per centimeter between the cathode and field wires,[1] which are typically grounded. The amplification region is established between the field wires and the anodes, or sense wires. The electrons liberated in the ionization due to a particle traversing the cell move through the drift region at a more or less constant speed towards the sense wires. In the amplification region, the electrons encounter a radial electric field due to the nearest sense wire. A a distance of about 100 μm from the wire, the electric field becomes strong enough to start an electron avalanche. This occurs when the energy an electron gains from the electric field exceeds the ionization energy of the gas. A typical avalanche liberates a few times 10^4 electrons for every electron which drifts to the wire. The signal induced on the wire by the avalanche is then large enough to be detected and amplified with conventional electronics. The distance of the original ionizing particle

[1] Somtimes also called guard wires or potential wires

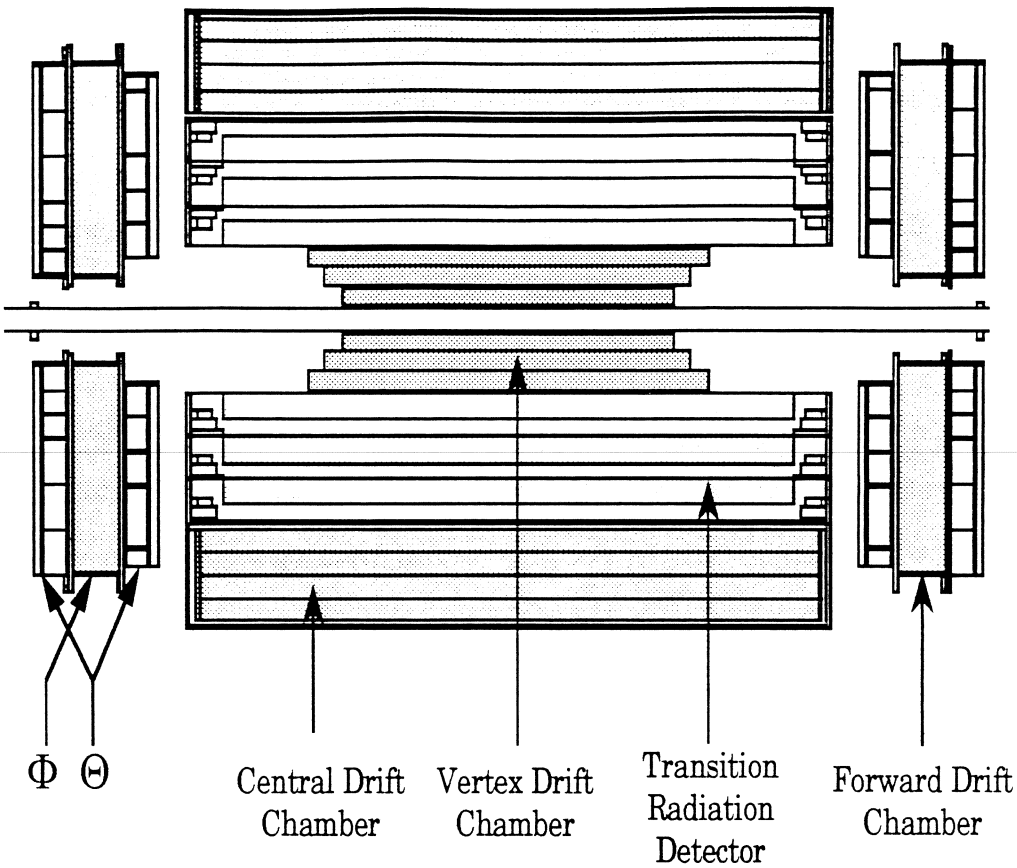

Figure 3.5: Side view of the DØ central tracking detectors.

from the sense wire can be determined from the time difference between the passage of the original particle and the time the avalanche is detected. The position of the track parallel to the wire must be determined by some other method.

3.5 The Vertex Chamber

VTX is the innermost part of DØIt has an inner radius of just 3.7cm and an outer radius of 16.2cm. It is composed of three layers with 16 cells in

the inner most layer, and 32 in the outer two. The drift velocity in the cell is 7.3μm/ns, giving a resolution of about 50μm in the drift direction. Each cell has eight sense wires, each of which is read out at both ends. The wires have a resistivity of 1.8kΩ/m, allowing the z coordinate to be measured with an accuracy of about 1% of the wire length. However, it has proven to be very difficult to achieve this performance in z in the very high multiplicity environment close to the beam pipe. As a result, the full three dimensional tracking efficiency has suffered. The chamber still shows excellent performance in the $R - \phi$ direction, but the two dimensional tracking information was not available at the time of this analysis, and as a consequence, the VTX was not used in the analysis presented here.

3.6 The Transition Radiation Detector

As it's name implies, the TRD is designed to detect transition radiation. Transition radiation happens when a very relativistic ($\gamma > 10^3$) particle traverses boundaries between media with different dielectric constants. In DØ this radiation is in the form of X-ray with the most probable energy of 8 keV. The TRD consists of three layer, with each layer containing 393 18μm thick polypropylene foils separated from each other by 150μm of nitrogen gas. The foils serve as the radiator. They are followed by a radial-drift wire chamber in each layer. The X-ray detection chamber is subdivided into 256 cells in ϕ and is filled with xenon gas in order to efficiently capture X-rays generated in the radiator. The PWC consists of a 15mm X-ray conversion stage followed

by a 8mm amplification stage. The TRD is able to differentiate between electrons and other particle, because for the same energy, electrons have a much higher γ and therefore produce more transition radiation than pions of the same energy. It is, however, important to realize that the signal measured in each TRD layer is a combination of track ionization and transition radiation, so that electrons can be separated from pions only on a statistical basis. The TRD has achieved a rejection factor of up to 50 for 90% electron efficiency. Because of the xenon gas and the radiator structures, the TRD accounts for most of the material before the calorimeter (8.1% at 90 degrees), and therefore photon conversions occur predominately here. Studies have shown that the TRD is useful in tagging photon conversions, but doing so involves a important loss in statistics because conversions tagged with the TRD must occur after the fist layer, and before the third detector region. For this and other reasons, such as the difficulty of calibration, the TRD was not used for this analysis.

3.7 The Forward Drift Chamber

The FDC is a close relative of the CDC, using similar dimensions for the cell structure, similar electrostatics, the same gas. However, its mechanical construction is completely different, as shown in Figure 3.6. The FDC is actually a pair of identical chambers positioned between the central detectors and the EC. Each half is composed of three separate chambers: a Φ module and two Θ modules. The Φ module is composed of 36 sectors with 16 anode

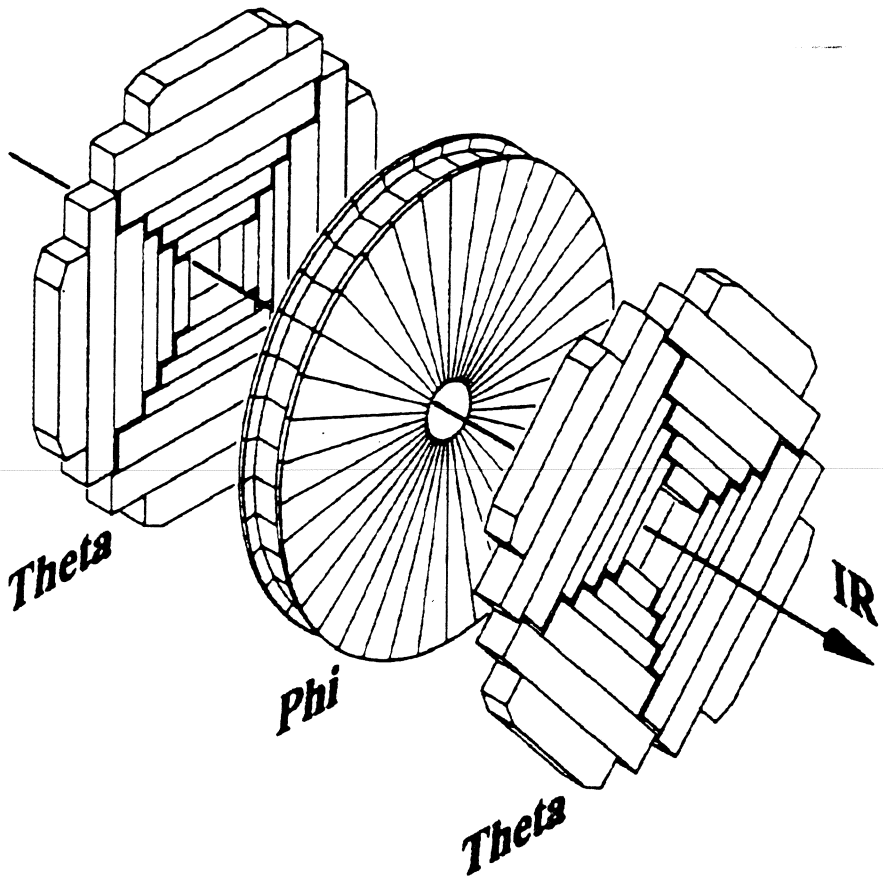

Figure 3.6: A view of one of two identical FDC halves. The Θ and Φ modules are shown separated for clarity.

wires running radially, separated from each other by a single guard wire. Each Θ module is composed of four quadrants of six cells, each with eight sense wires and a single delay line. The FDC achieves performance similar to that of the CDC. It is notable for extending down to within 5 degrees with respect to the beam. Because the analysis described here is restricted to photons in the central rapidity interval, the FDC is not used in this analysis.

3.8 The Central Drift Chamber

The CDC plays a key role in distinguishing between photons and electrons in the central region, by matching tracks to the position of electromagnetic showers in the CC. The CDC is a drift chamber with wires running parallel to the beam and drift in the ϕ direction. It is composed of four layers, made from 32 identical modules. Figure 3.7 shows three such modules. Notice that no single module contains a complete cell, but cells are formed when the modules are brought together. Each cell contains seven sense wires separated from each other an the drift region by two guard wires each. The position of the avalanche in z is determined by use of delay lines. Delay lines are transmission lines of carefully controlled inductance and capacitance and a minimum of resistance. In the idealized case, the complex impedance of the delay line is

$$Z = \sqrt{\frac{L}{C}}, \tag{3.10}$$

and the signal propagates through the delay line with velocity

$$v = \frac{1}{\sqrt{LC}}. \tag{3.11}$$

In the CDC, delay lines are imbedded in the support structure near the first and last (i.e. outer) wire of each cell. When an avalanche occurs on the outer wire, a small signal is induced in the delay line at that point. It propagates in both direction, and is read out at both ends, by knowing the time of the avalanche on the sense wire and the time of the signal on the delay line, the z position of the avalanche may be calculated. Because the delay line signal is induced, it is only a small fraction of the signal on the sense wire. As

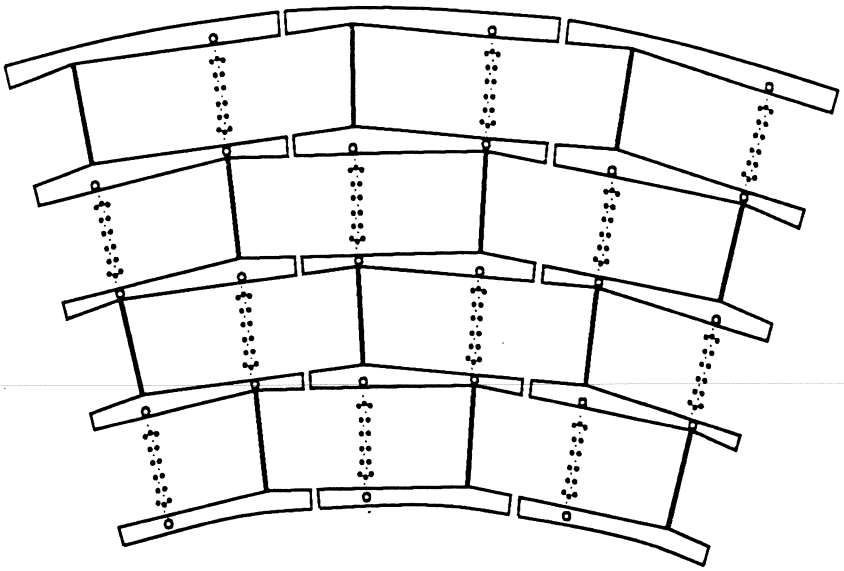

Figure 3.7: End view of three CDC modules.

a consequence the delay lines suffer from a poorer signal to noise ratio than the sense wires. In order to reduce the effect of the induced signals from the inner wires, the outer sense wires at a higher gas gain compared to the inner sense wires. Some CDC parameters are summarized in Table 3.5.

The the performance parameters of the CDC most important for the photon analysis are the dE/dX resolution, tracking efficiency and tracking accuracy. The limitation on track finding efficiency is due primarily to two factors: the structure of the CDC and the efficiency of track reconstruction. The structural limitation is due to the fact that cathodes and sense wires lie in the same line along ϕ, so that tracks very close to this region are lost. Other tracks are lost due to problems with mismeasured hits and other tracking

Table 3.5: Some parameters of the CDC.

Length of active volume	179.4cm
Inner radius of active volume	51.8cm
Outer radius of active volume	71.9cm
Number of sense wires	896
Number of delay lines	256
Drift field	620V/cm
Typical drift velocity	34μm
Sense wire potential (inner)	1.385kV
Sense wire potential (outer)	1.584kV
Gas gain	2,6 $\times 10^4$ nominal
Number of ionization samples	28
dE/dX resolution	$\approx$ 18%
Hit position resolution in the drift direction	$\approx$ 200μm
Delay line velocity	2.4mm/ns
Hit position resolution along the sense wire	$\approx$3mm

problems. It is known that certain systematic problems especially in the z coordinate reconstruction cause tracks that are poorly measured and may be lost. The track reconstruction efficiency has been measured by the photon group to be $92 \pm 2\%$ in the region of full acceptance for the CDC. The dE/dX resolution is important for the identification of conversions, which are used in the background subtraction as discussed in later chapters. This parameter is affected by several factors, chief among them the stability of the HV supplies, and the atmospheric pressure. The pressure is important because the CDC is kept at atmospheric pressure, so that the density of the gas varies as the atmospheric pressure varies. It is known that gas gain of the chamber increase with decreasing density of the gas. Fortunately it is straight forward to correct for this effect, and the CDC tracks are so corrected. [24] The stability of the HV supplies is a more complicated issue. In the begining of Run 1A the CDC sense wires were supplied by some 32 separate supplies, for reasons of safety and protection. This made it difficult to keep all supplies within required tolerance of 3 to 4 volts. On the other hand, small changes in supply voltage tended to be smeared out. During a maintenance shutdown about half way through Run 1A, this arrangement was changed so that there was only one power supply for the inner sense wires and one for the outer sense wires (because they run at different voltages). This was made possible by a unique current monitoring and protection system. [25] This system operates by measuring the current on the potential wires. When an abnormal situation such as a discharge is detected, the system is able to raise the voltage on the potential wires several hundred volts, thus reducing the electric field at

the sense wire, and as a consequence the gain. Using the new system has improved the reliability and stability of the gain, but when there is drifting in the supply, it affects the entire chamber. Corrections can be applied for the known changes, but the studies require to do so were not available at the time this analysis was finalized. [26] Since that time we have implemented a system to accurately monitor changes in the high voltage.

3.9 Trigger

The inelastic cross section in $p\overline{p}$ collisions at the Tevatron energy is approximately 55 milli-barns [28]. The cross section for direct photons in the central region above 30 GeV E_T is on the order of 500 pico-barns. In other words, only about one in a hundred thousand $p\overline{p}$ collisions will result in a direct photon candidate of this transverse energy. The same can be said of other processes at the Tevatron- the interesting ones are extremely rare. In addition, many studies require large statistics– there are over one hundred thousand direct photon candidates, but this angular distribution analysis still suffers from low statistics.

In order to be able to study such processes, the first requirement is a machine able to produce the required number of collisions in a reasonable amount of time. The Tevatron has done this with style, producing nearly a trillion proton anti-proton collisions during Run 1A just at DØ. But producing the events is only the begining- picking out the interesting ones can be quite a challenge as well. This is accomplished by the trigger system. The description

below is very brief and concerned mostly with the features relevant specifically to the direct photon analysis. However, excellent descriptions of the entire system exist and the interested reader is reffered to those. [10]

The challenge faced by the trigger system is daunting- the collisions in Run 1A at the Tevatron occur at a rate of about three hundred thousand per second. (In the Tevatron, bunches of protons and anti-protons meet at the center of DØ every 3.5 μs.) In order to meet this challenge the DØ trigger system is organized in to three separate stages: level-0, level-1 and level-2. The general layout of the trigger is shown in Figure 3.8.

3.10 Level 0

The level-0 trigger is a collection of the scintillators located between the Central Cryostat and each of the End Cryostats. The scintillators are very efficient ($> 99\%$) at detecting any nondiffractive inelastic collision within the detector. The timing of the signals from these scintilators can be used to roughly locate the position of the collision within the detector. A fast vertex determination is available within only 800ns, and a more accurate one, with a resolution of ± 3.5cm is available within a few microseconds.

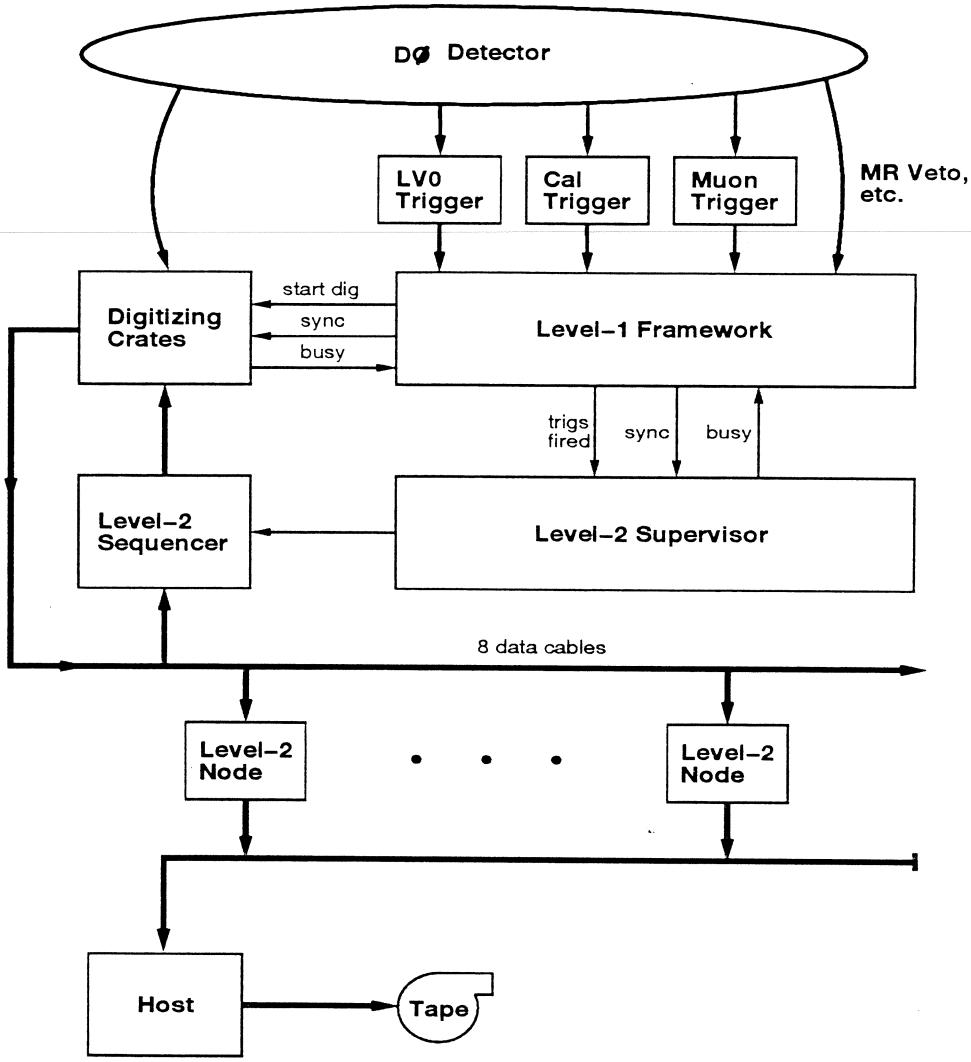

Figure 3.8: A general overview of the DØ trigger system.

3.11 Level-1

The level-1 trigger is composed of special hardware which looks at data coming from the fast pickoff of the calorimeter (described below) and some muon information, as well as signals from the accelerator and trigger scintillators. In order to avoid deadtime, the level-1 trigger decision must be reached in less than the 3.5μs available between crossings, and therefore only rather rough information is available. [2] This information is presented to the trigger framework a set of 256 *trigger terms*. Each trigger term is a single bit that represents some specific trigger condition such as "one of the calorimeter trigger towers has more than $12GeV$ of energy" or "there is a good signal present in the level-0 trigger". These 256 trigger terms are reduced to 32 level-1 trigger bits by a programmable and-or network. Each trigger bit can be fired by a combination of of the 256 trigger terms or their compliments. Each trigger also has a programmable prescale– in other words, the trigger will fire only after the required trigger terms have occurred N times since the trigger fired last.

Once a trigger does fire, a signal is sent to the digitizing hardware to start digitization of the analog signals from the detector. The digitizing hardware resides in the 86 front-end VME crates. Each crate is double buffered, so that a trigger can be received while the readout of a previous event is still in progress.

---

[2] Some triggers that require longer to reach a decision are referred to as level-1.5 triggers. In Run 1A all such triggers were muon triggers and we will not be concerned with them here

However, it may happen that several events occur in rapid succession, and the digitize signal is received while both buffers are busy. In this case a busy signal is sent back to the level-1 to indicate that the front-end crates are not ready to receive a trigger. This condition is called a "front-end busy" and is an important source of deadtime. The rate of front-end busies limits the rate at which the detector can be read out to about 200Hz. [27]

3.12 Calorimeter Trigger

The calorimeter trigger is derived from the fast trigger pickoff of the calorimeter shaper cards. [29] This signal is a sum of cells in towers of size 0.2×0.2 in $\eta - \phi$ space. A separate signal is provided for the EM and FH layers of the towers, resulting in 2560 separate signals. For use in the level-1 trigger, the inputs are flash digitized and compared to preprogrammed thresholds to derive the trigger terms for the calorimeter. Each tower can be compared to four different thresholds each for the hadronic and electromagnetic part of each tower, as well as another set of four thresholds for the tower as a whole. A trigger term is asserted for each threshold that is exceeded. This allows a level-1 trigger to require, for example "One EM tower above $14GeV\ E_T$". This in fact was the level-1 one trigger used for the analysis described here.

In addition the calorimeter trigger forms sums which can be compared to preprogrammed thresholds to provide triggers terms. These are:

- The total electromagnetic energy, $\Sigma_i E_i^{EM}$.

- The total hadronic energy, $\Sigma_i E_i^{had}$.
- The total (scalar) electromagnetic transverse energy, $\Sigma_i E_i^{EM} \sin\theta_i$.
- The total (scalar) hadronic transverse energy, $\Sigma_i E_i^{had} \sin\theta_i$.
- The total transverse energy, $\Sigma_i E_i^{EM} \sin\theta_i + E_i^{had} \sin\theta_i$.
- And the missing transverse energy, $\not{E}_T = \sqrt{E_x^2 + E_y^2}$, where

$$E_x = \Sigma_i(E_i^{EM} + E_i^{had} \sin\theta_i \cos\phi_i) \tag{3.12}$$

and

$$E_y = \Sigma_i(E_i^{EM} + E_i^{had} \sin\theta_i \sin\phi_i) \tag{3.13}$$

Although the level-1 is flexible and fast, it is not very efficient. The reason for this is in part the poor energy resolution of the trigger and in part the tower structure of the trigger. In triggers for EM objects, the level-1 often does not become efficient until the E_T of the triggering object is nearly twice the threshold of the corresponding level-1 trigger. The turn on curve for the level-1 trigger used in this analysis ($EM1_MAX$, which requires one EM tower above 10GeV in E_T) is shown in Figure 3.12.

(Figure courtesy of Sal Fahey.)

3.13 Level-2

The level-2 trigger is closely associated with the readout of the detector. It is a farm of some 50 general purpose computers running software filters on the

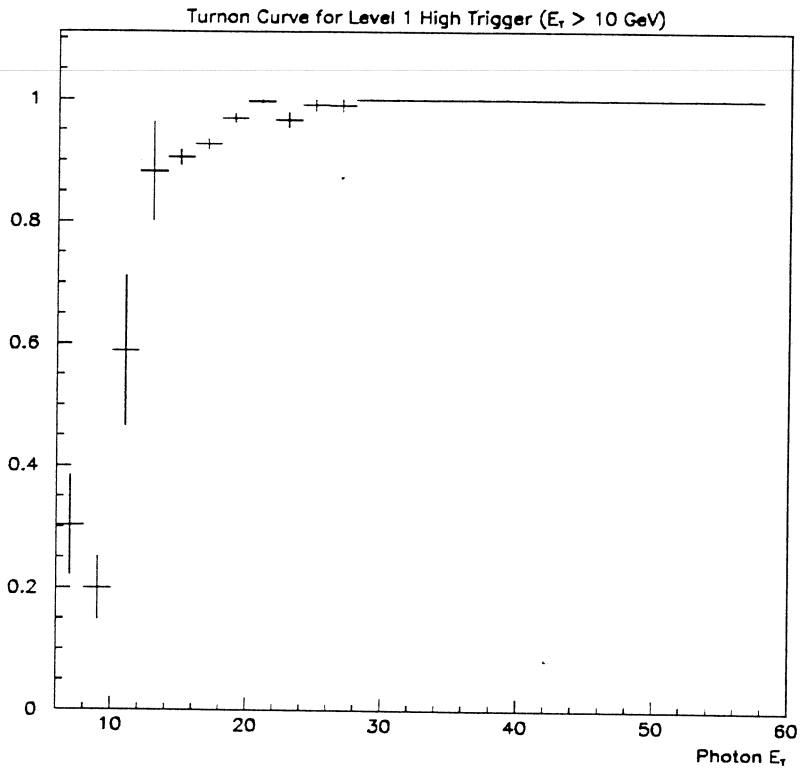

Figure 3.9: The turn-on curve for the level-1 photon trigger

complete data from each event. Thus, before level-2 can reach a decision, all the data collected by the detector during an event must be read out, digitized and brought together in a single place. The amount of time taken to move the enormous amount of data collected during each event is a fundamental limitation on the rate at which level-2 can accept data. However, because all the digitized data is available, the level-2 system is able to perform much more detailed event reconstruction than level-1, and as a consequence is much more accurate. Unfortunately, some things are too time consuming, and can not be done even in level-2. For example, an accurate vertex determination is not available. As a consequence, the E_T resolution does suffer somewhat. The event selection in level-2 progresses in several sequential steps.

- Using a list of candidate towers from level 1, a cluster is built around the most energetic cell in layer EM3, using a window of $\delta\eta \times \delta\phi = 0.3 \times 0.3$ and including all cells in the EM layers and FH1.

- The transverse energy of the cluster must be above the trigger threshold. For this analysis, the trigger threshold was $30GeV$.

- The energy in the FH1 layer must be less than 10% of the total cluster energy.

- The energy in the EM3 layer must be greater than 10% and less than 90% of the total cluster energy.

- A shower shape cut is applied based on the second moment of the energy deposition in a $\delta\eta \times \delta\phi = 0.5 \times 0.5$. [30].

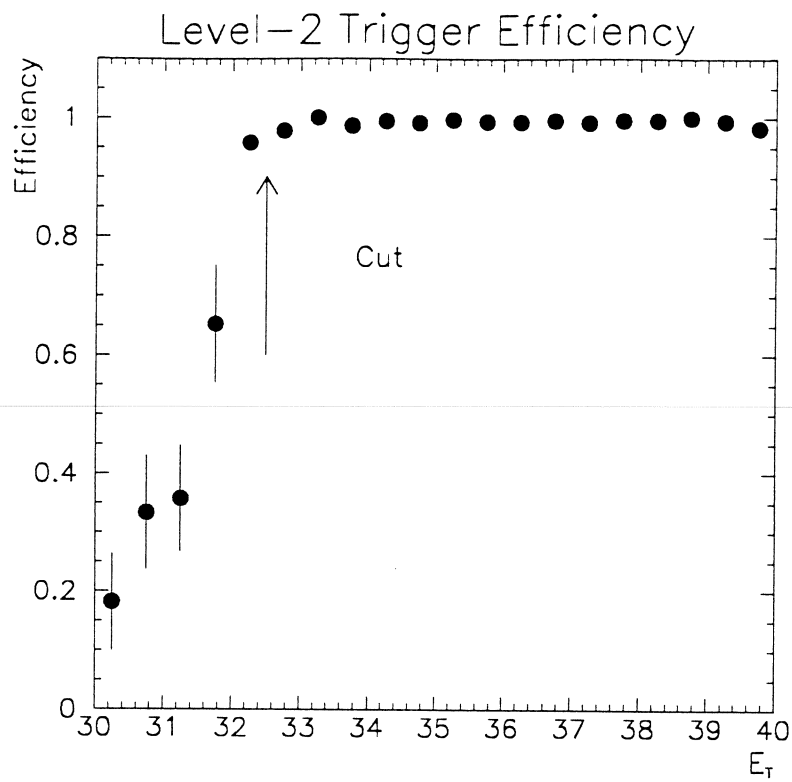

Figure 3.10: The turn-on curve for the level-2 photon trigger

- An isolation cut is applied so that the energy within a cone of radius 0.4 in $\eta - \phi$ space is no more than 15% larger than the cluster energy. That is, $E_{\text{isolation cone}} < 1.15 \cdot E_{\text{cluster}}$.

The turn on curves for the level-2 trigger is shown in Figure 3.10. Events that pass the trigger are written to tape. Further analysis takes place offline and is the subject of the next chapter.

Chapter 4

Candidate Event Selection

In this chapter we will address the issues involved in attempting to select events which are likely to be direct photons and are well measured enough to be useful in determining the angular distribution. We discuss the process involved in sifting out these candidates from the millions of events which pass the trigger. We have to address the criteria used to select photon candidates, and the efficiency of such cuts. In particular, we must understand how the efficiency changes depending on the angle of the photon, where the detector is trustworthy and where the events are poorly measured. For the most part, the main concern is choosing events with a well measured photon, but we must also discuss how jets are treated, since we must use the information derived from jets to reconstruct the angular distribution in the partonic center of mass system.

4.1 Reconstruction

The raw data flowing from the detector must be processed in order to reconstruct the particles produced in a $p\overline{p}$ collision. The signals coming from the various detectors are identified with specific physical objects, such as jets and leptons. This is done by the reconstruction program, DØRECO.

The identification of photons at DØ begins with the same properties as used in the trigger: a narrow, localized deposition of energy confined to the electromagnetic layers of the calorimeter. Since the photon shares these characteristics with electrons, the photon ID is able to take advantage of the tools developed for the electrons. However, because the physics issues addressed are somewhat different, the final selection criteria differ. Physics topics for which electron identification is most important, such as W/Z physics and the top search, have relatively small backgrounds but also small signals, and the selection criteria must be chosen to maximize efficiency while maintaining good background rejection. In photon selection, the problem is reversed. The efficiency is important, but the dominant concern is always the background. Particle ID proceeds in several stages, with the cuts becoming increasingly selective. The photons and electrons are treated identically until the very last stages of the process. This allows us to use electrons from W and Z bosons, which can be identified using kinematics, to check the efficiency of our selection cuts. [32]

DØRECO uses very loose criteria to identify electrons and photons. Candidates are build using a "nearest neighbor" algorithm [31], starting with the

highest E_T tower and adding adjacent towers above threshold. If at least 90% of the cluster energy is contained in the EM section of the calorimeter and at least 40% is contained within a single tower, the cluster is classified as a photon. (However, if there is a track within a "road" of $\delta\eta = \pm 0.1$, $\delta\phi = \pm 0.1$ pointing to the object, the object will be classified as an electron instead of a photon.) The energy deposited in the third EM layer is used to calculate the centroid of the cluster, which is used in determining the direction of the object, and to determine the road for track matching. The position resolution of the centroid is about 1mm [21].

4.2 Streaming

In order to reduce the number of events which must be analyzed, the reconstructed data is separated into various subsample's. This process is referred to as streaming, and the subsamples as streams. The photon analysis has its own stream which forms the basic sample from which the final candidate events are selected. This stream is composed of events which pass at least one photon trigger and have a photon (or electron) candidate which passes the trigger selection cuts offline. In other words, the cuts used in the trigger are applied to the objects reconstructed offline, and those events which did not have at least one object which passed the cut were excluded from the stream. Neither the trigger nor the streaming examine the tracking information, and therefore we do not differentiate between electrons and photons at this level.

4.3 Standard Cuts

DØRECO also computes certain quantities from each cluster which may be used during later analysis to reduce background contamination in the candidate sample. Some of the most important of these include the EM fraction, the isolation energy, and the χ^2 of the H-matrix. [33],[34], [32]

- The EM fraction is the fraction of the total energy of the cluster contained within the electromagnetic section of the "core" cone (which includes all calorimeter cells within $\Delta R = \sqrt{\Delta\eta^2 + \Delta\phi^2} < 0.2$).

- The isolation energy is defined as the energy deposited between two cones of radius $\Delta R = 0.2$ and $\Delta R = 0.4$ measured from the cluster centroid.

- To further improve the rejection of hadronic showers in the photon/electron sample, information about the longitudinal and transverse shower shape is taken into account with the H-matrix technique. A covariance matrix is calculated by measuring certain quantities E_i for electron showers,

$$C_{ij} = \langle (E_i - \langle E_i \rangle)(E_j - \langle E_j \rangle) \rangle. \tag{4.1}$$

The H-matrix is then simply:

$$H_{ij} = C_{ij}^{-1}, \tag{4.2}$$

and we can calculate an effective χ^2 for each event:

$$\chi^2 = \Sigma_{ij}(E_i - \langle E_i \rangle) H_{ij} (E_j - \langle E_j \rangle) \rangle. \tag{4.3}$$

The quantities included in the H-matrix are the fraction of the cluster energy in each of the EM layers except EM3 (3), the energies of a 6×6 array of cells in the EM3 layer (36), the logarithm of the total energy and the z position of the primary vertex (2), for a grand total of 41 elements. This gives a 41×41 matrix which was carefully built with detailed DØGEANT simulated electrons and checked on real data taken from the test beam. Cutting on the effective χ^2 gives a powerful tool for selection of photon and electron candidates. [35]

- Because of the physical structure of the calorimeter, there are 16 small cracks between modules of the CC which are projective in ϕ. Normally, photons which hit the crack fail one of the cuts described above. However, on a rare occasion photons near the crack pass all the quality cuts, but suffer some energy loss associated with the crack. In order to avoid the penalty of worsened energy resolution, and to avoid uncertainty in the efficiency, the photon group makes a cut requiring that photon candidates be further than 19.63 $mrad$ away from the center of the crack. This is simply the 20% of the calorimeter closest to the crack. This cut has a simple geometric efficiency of 80% , but it actually cuts very few photon candidates that would have passed otherwise. And those that are cut out by this cut tend to be mismeasured in energy. This is shown in Figure 4.1.

- In order to assure that the event is well measured, and to remove contamination from W boson decays, we impose a cut on missing E_T(after

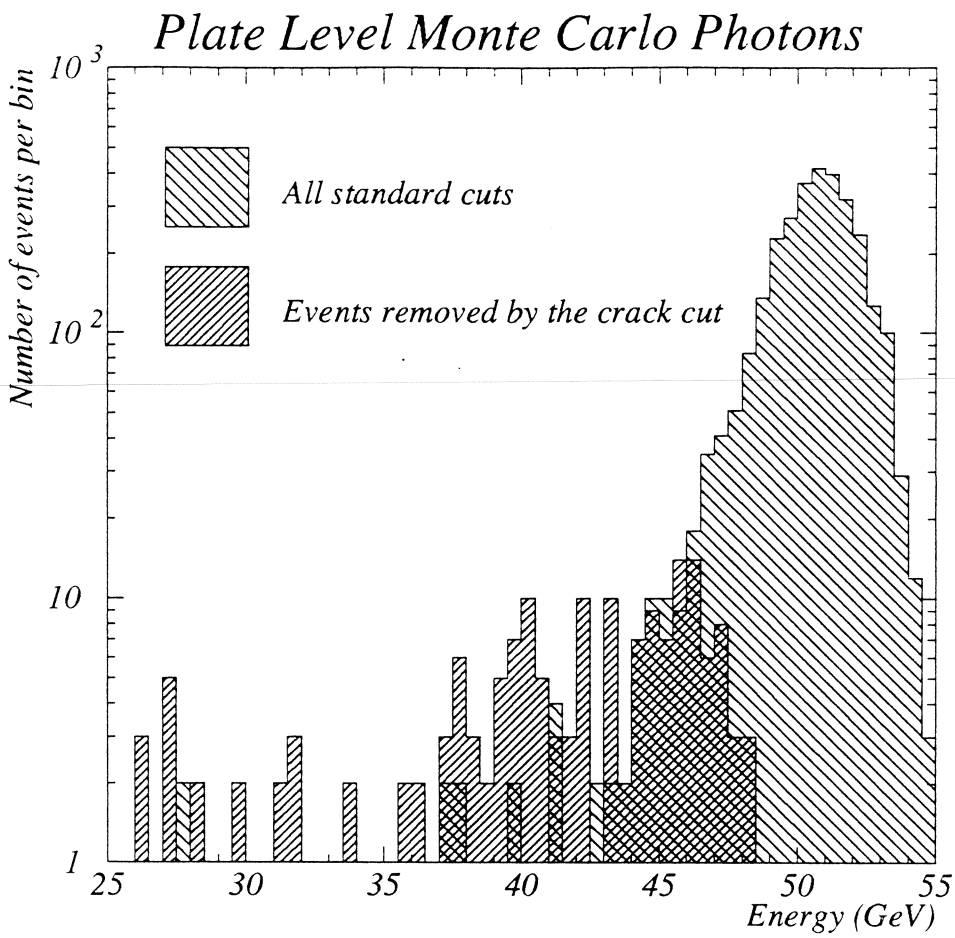

Figure 4.1: The reconstructed energy of monoenergetic $50GeV$ photons after all quality cuts. Most of the low energy tail is removed by the crack cut

all corrections) and require that $\not{E}_T < 20GeV$ in the event.

The cuts used in reconstruction and streaming are purposefully very loose, in order to be very efficient, and to allow studies of the backgrounds in the sample. The events which are included in the final candidate sample must pass much tighter offline cuts. These are cuts on the isolation energy, the EM

fraction and the H-matrix χ^2 of the candidate cluster described above. Since we know that showers from photons and electrons will appear nearly identical in the calorimeter if we do not look too closely at the very beginning of the showers (about the first 2 radiation lengths), we can check the efficiency and the rejection of the cuts by studying electrons from Z and W boson decays in the data. This is possible because of the kinematic properties of the W and Z. Since we know that the decay of the Z boson (for example) forms a sharp peak in the two electron mass spectrum, we can fit the peak and the inevitable "shoulders" to measure the number of true and fake electrons. Figure 4.2 through Figure 4.5 show an example of how this can be done. Similar studies can be done with the W data, and can be used to estimate the E_T dependence of the cuts. But a major advantage of the Z events is that we can get a very pure sample by making tight cuts on one electron and studying the second one. This is the cleanest and best way to study the cuts in the data, but this method suffers somewhat from low statistics.

Table 4.1 lists the results of such a study. These results were used to select the standard photon ID cuts. (All values are accurate to about $\pm$ 2%). The combination of cuts 1,4 and 5 is what is referred to as standard photon cuts.

When looking at the above table, it may appear to the reader that the isolation cut is a poor one. It has the lowest efficiency relative to its rejection.

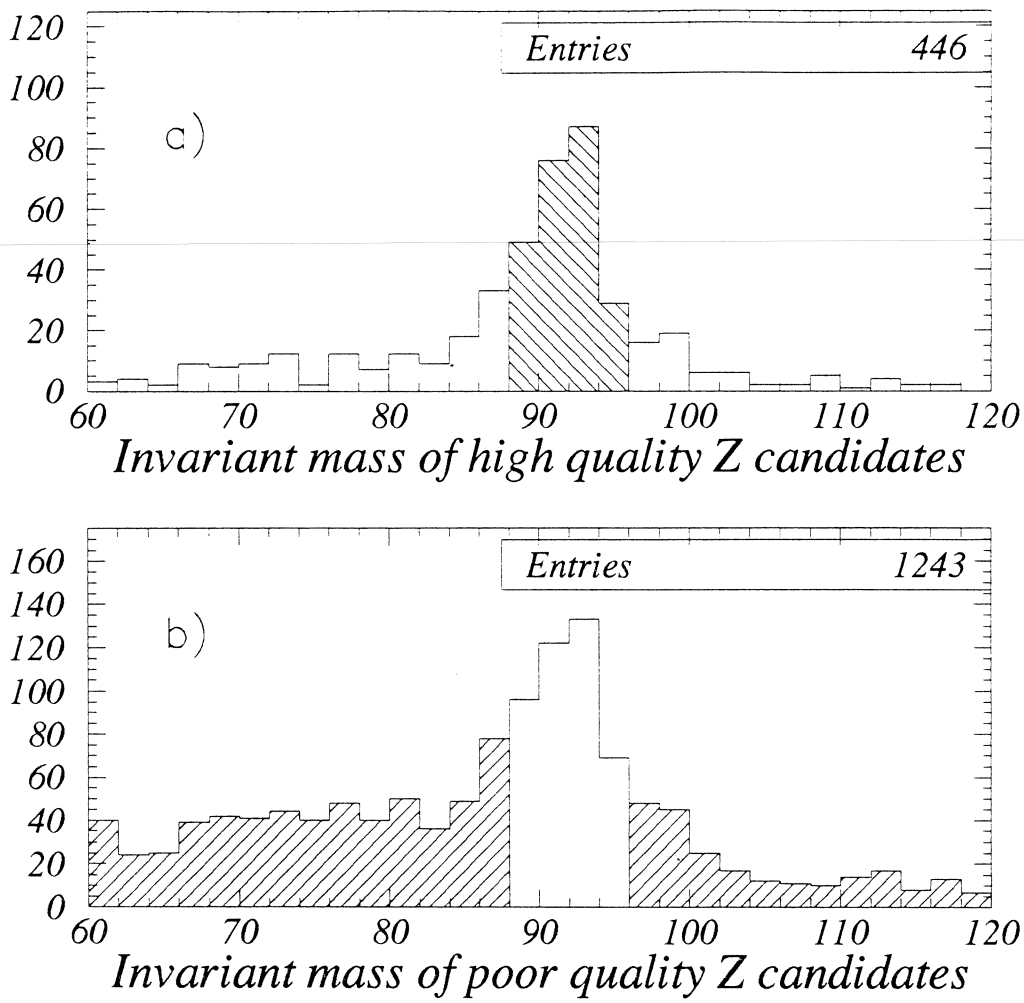

Figure 4.2: Invariant mass of the two highest EM clusters, where both objects have E_T above 25 GeV and the leading object is in the central region. Plot a) highlights events that have a invariant mass consistent with the Z boson, and are most likely to be real electrons. Plot b) highlights events that have an invariant mass that is inconsistent with the Z boson, and are defined to be background.

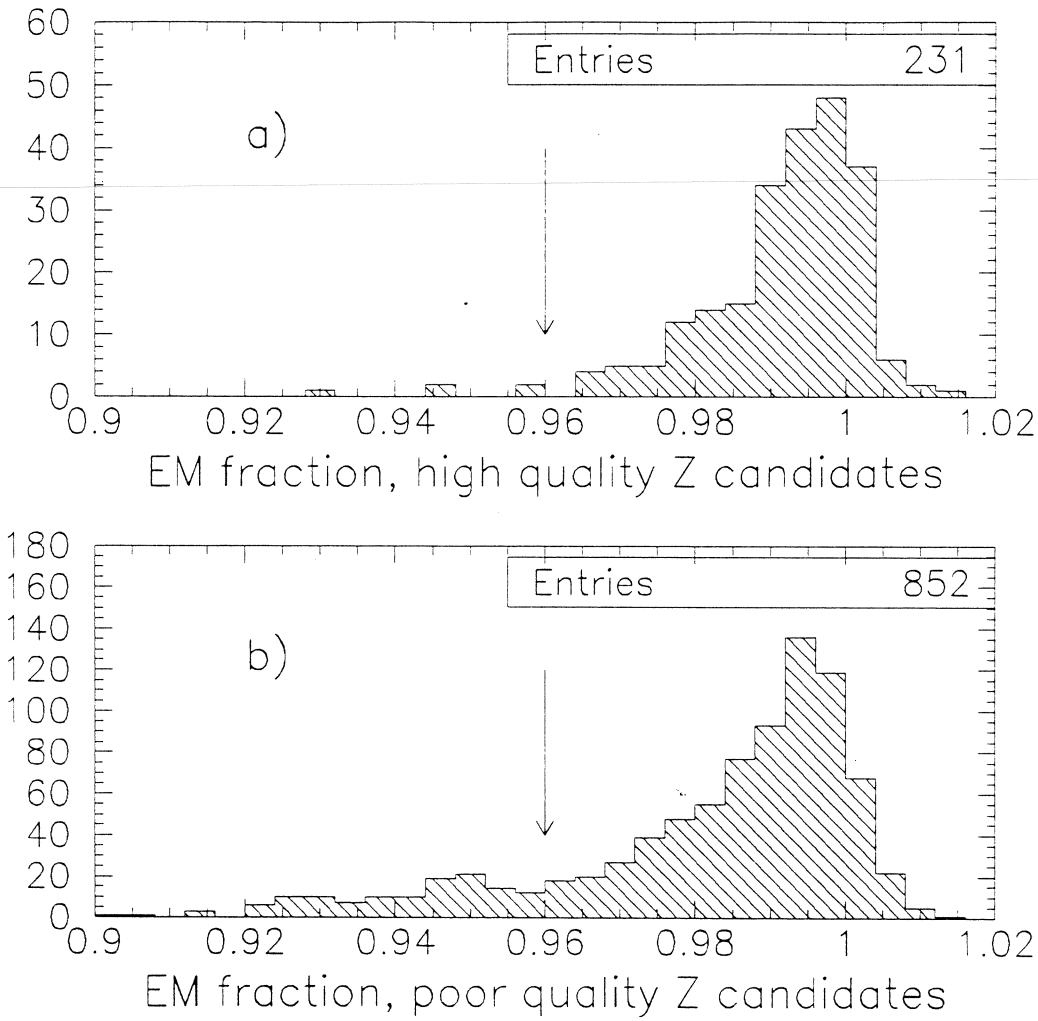

Figure 4.3: The electromagnetic fraction of electron candidates from Z boson decay. Plot a) shows events defined as in Figure 4.2 a). Plot b) shows events defined as in Figure 4.2 b).

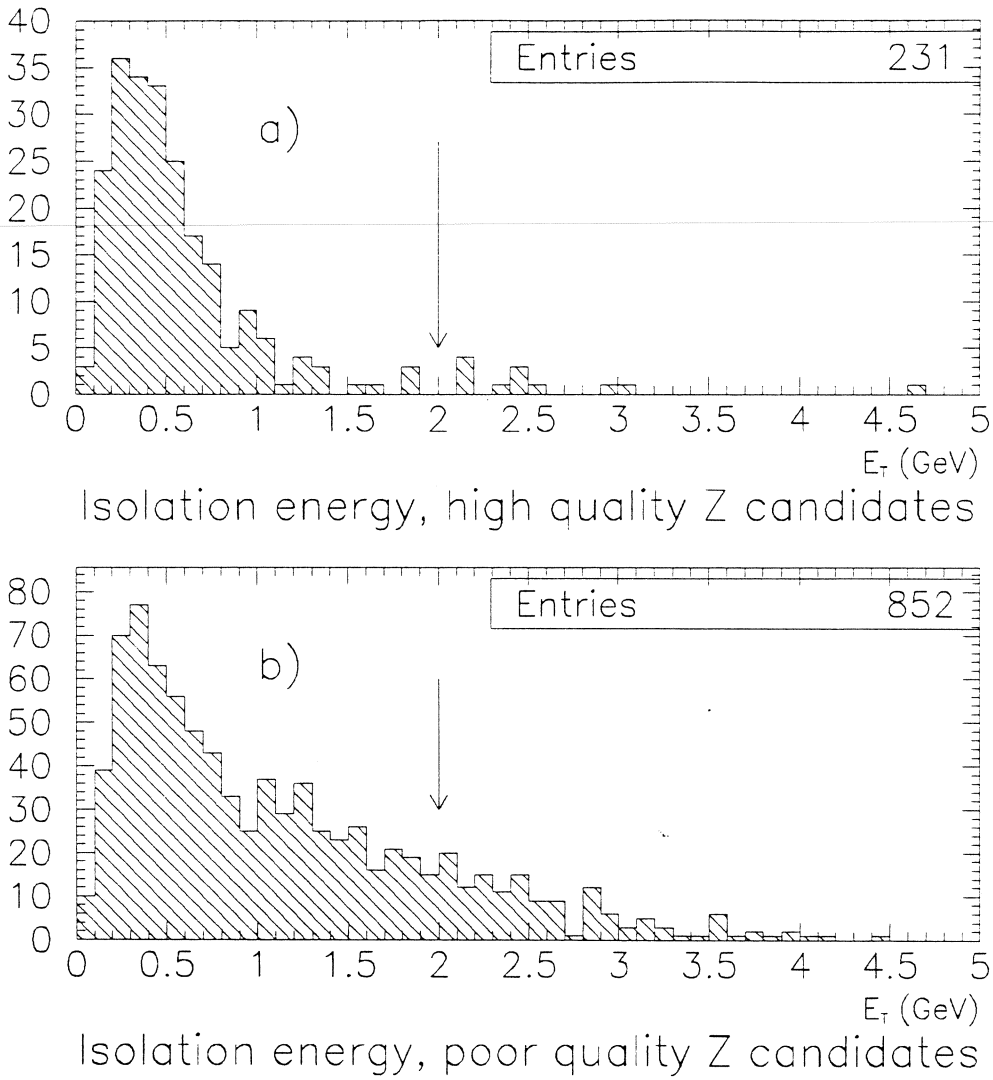

Figure 4.4: The isolation energy of electron candidates from Z boson decay. Plot a) shows events defined as in Figure 4.2 a). Plot b) shows events defined as in Figure 4.2 b).

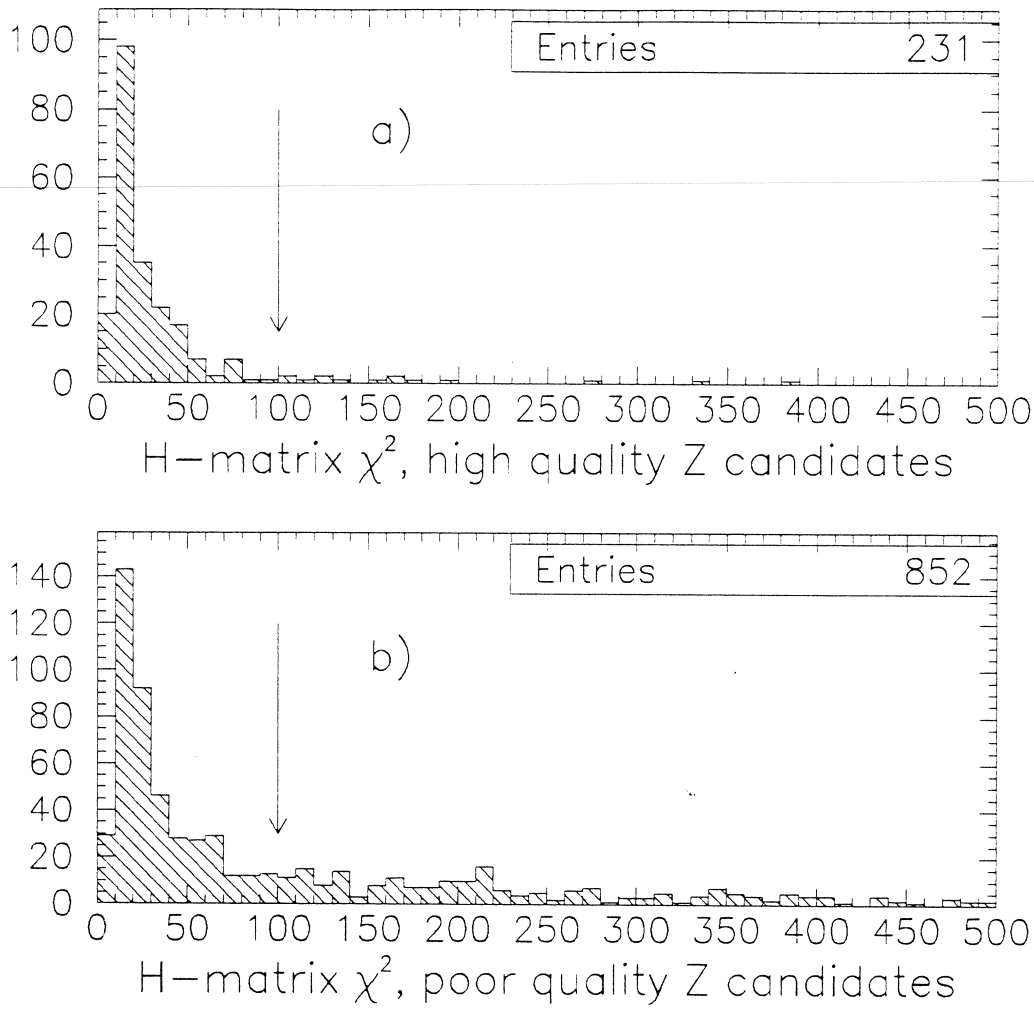

Figure 4.5: The H-matrix χ^2 of electron candidates from Z boson decay. Plot a) shows events defined as in Figure 4.2 a). Plot b) shows events defined as in Figure 4.2 b).

Table 4.1: Efficiency of standard photon ID cuts.

Cut	Variable(s)	Value	Signal Efficiency	Background Efficiency
1	H-matrix χ^2	<100	92%	74%
2	H-matrix χ^2	<50	85%	59%
3	Isolation .4 -.2	$< 3GeV$	92%	84%
4	Isolation .4 -.2	$< 2GeV$	80%	66%
5	EM fraction	$> 96\%$	96%	87%
6	cuts 1 and 3		86%	67%
7	cuts 1 and 4		76%	57%
8	cuts 4 and 5		78%	60%
9	cuts 1 and 4 and 5		74%	53%

It may also be argued that this cut would make more sense if it was a percentage of the photon energy, instead of a fixed energy. Indeed, this is the way the isolation variable is used in other analyses concerned with electron ID, such as electroweak physics and the top search. However, the fixed energy cut makes more sense when considering photons over a large energy range, because the underlying event and noise in the detector are expected to contribute a fixed amount of energy, independent of the photon energy, and therefore a fractional cut may vary in efficiency when applied to photons of very different energies.

Photons originating in the hard collision may interact in the material of the tracking chambers before the calorimeter. The most common such interaction is pair production, in which the photon produces an electron pair of low invariant mass. The two electrons can not be resolved and leave only

a single track in the detector. Thus, the photon appears to be an electron. Such events are referred to as photon conversions. This is the main reason for treating photons and electrons on the same footing: objects identified by DØRECO as electrons may in fact be converted photons. However, such tracks differ from single electron tracks because the two electrons of the pair will leave a track with about twice the ionization of that expected for a single electron, and can thus be identified as conversions with good efficiency. A plot of the ionization left in the CDC by tracks associated with photon candidates is shown in Figure 4.6. Because of the very wide roads used to find tracks in the vicinity of an electron candidate, random tracks from the underlying event may sometimes fall within the road. However, such tracks are almost always minimum ionizing, and are randomly distributed within the road. If we require that the track match accurately the position of the electron candidate, we see the two mip peak, characteristic of conversions, clearly separated from minimum ionizing tracks. The difference between the position of the one mip peak from random tracks and the one mip peak closely matched tracks (which are most likely energetic electrons) can be attributed to the relativistic rise in the dE/dx.

In order to determine the efficiency of tagging conversions, studies of the tracking variables have been done with W and Z bosons. The standard photon cuts for identifying conversions are *track match significance* < 5 and only one

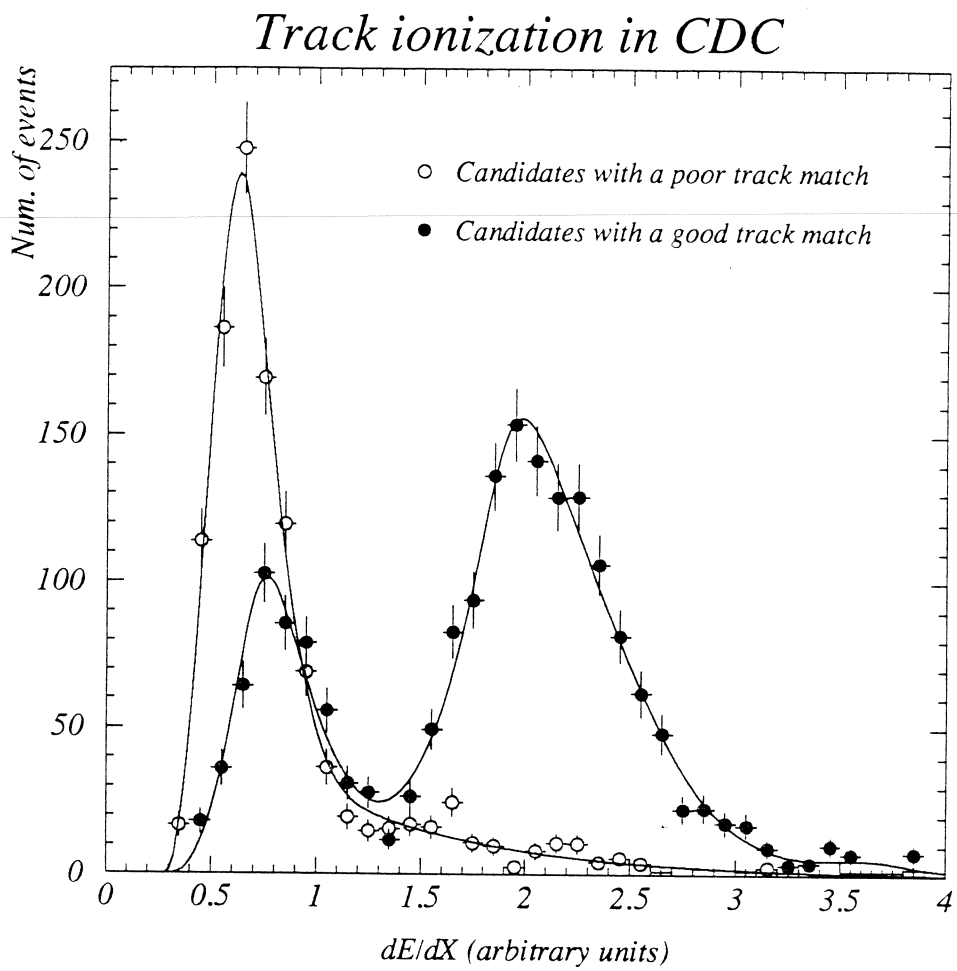

Figure 4.6: The ionization of tracks near a photon/electron candidate as measured by the CDC. Tracks that match the cluster more accurately are more likely to be the result of a photon conversion. Tracks that do not point accurately to the candidate cluster are more likely to be random overlaps.

track associated with the object. Track match significance is defined as:

$$S = \sqrt{\frac{\Delta\phi^2}{\sigma_\phi^2} + \frac{\Delta z^2}{\sigma_z^2}}, \tag{4.4}$$

where the $\Delta\phi$ and Δz is the measured distance between the centroid of the cluster and a particular track, and σ_ϕ and σ_z are the combined resolution of the CDC and calorimeter shower centroid. The tracking cuts have been measured to be 72$\pm$ 2% efficient for Z bosons decaying to two electrons. We will leave a detailed discussion of the tracking for the chapter on background subtraction.

4.4 Acceptance

In order to assure that the candidate events lie in the region of full acceptance within the calorimeter, we demand that the photon is safely away from edges of the central calorimeter ($|\eta| < 1.1$ for photons originating at the geometric center of the detector). This limits the angle over which the photon can be observed, which in turn depends on the position of the vertex. It is a simple matter to calculate what that maximum angle is for a given vertex position. However, when the data are examined, there seems to be an obvious loss of acceptance before that maximum angle is reached. We can study this from the data by looking at the η distribution of the photon candidates for different positions of the event vertex along the z axis. (For this study we require that the event has only one interaction vertex.) The position of the vertex is roughly gaussian, with a σ of almost 25 cm, (as shown in Figure 4.7, and events relatively far from the detector center are not uncommon. The

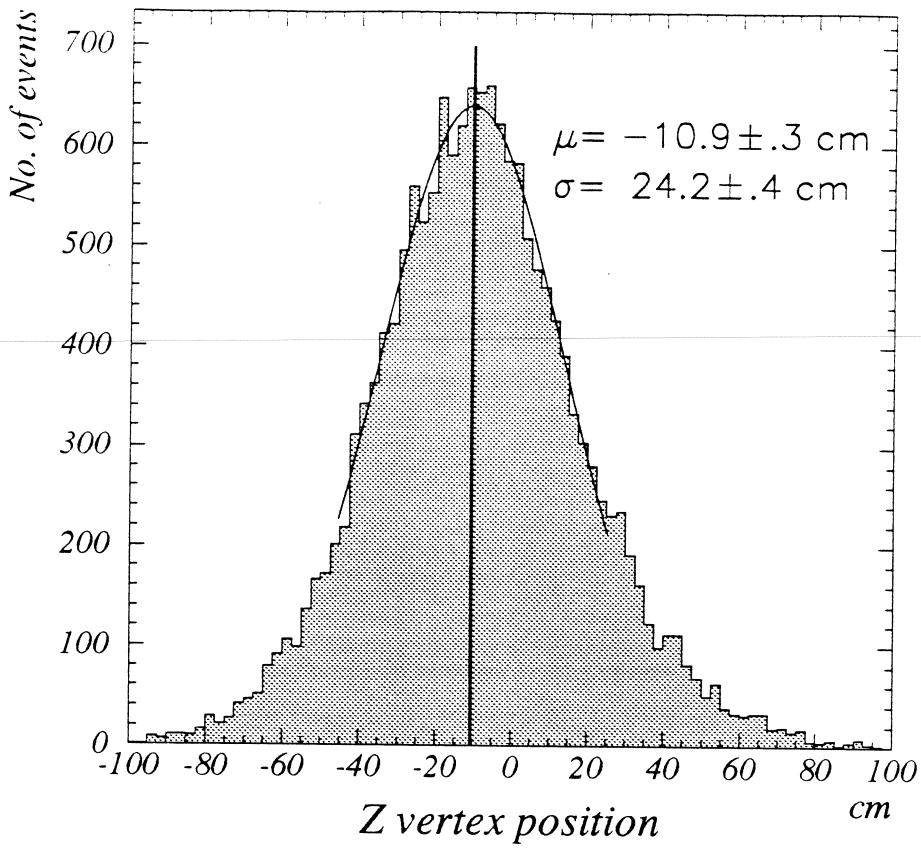

Figure 4.7: The position of the primary interaction along the z axis for a sample of direct photon candidate events. The events have been selected to be likely single interactions.

spread in the position of the interaction vertex is due to the length of the bunches in the accelerator. This is an unfortunate (but unavoidable) situation in that we must drop otherwise perfectly good events because they originated from a vertex far from the center of the detector, and therefore are not well measured. The situation in Run 1A was further complicated by the fact that the center of the interaction region did not coincide with the center of the

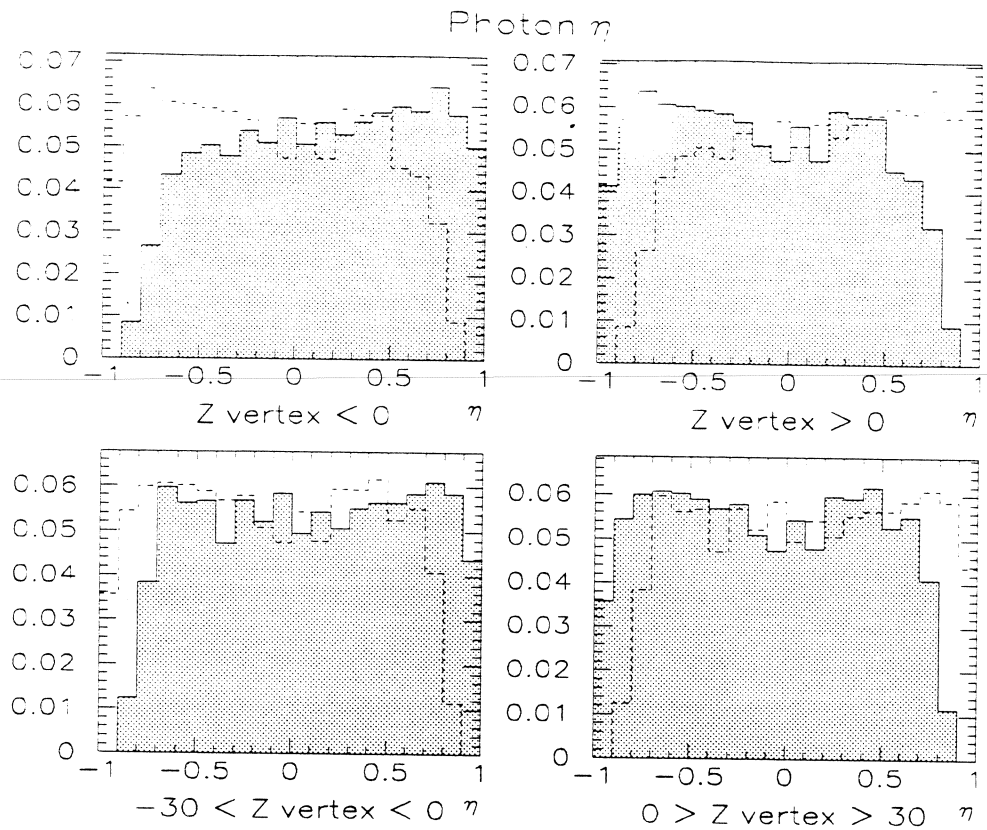

Figure 4.8: η distribution of photon candidates when the event vertex is less than zero or greater than zero. To emphasize the difference, the complementary histograms are also shown superimposed.

detector.

However, we can turn at least some of the problems caused by the wide spread in the vertex position to our advantage. We know that there can be no difference in the physics distributions due to the different vertex position. So we can assume that if we do see a difference, it must be due to detector inefficiency. Figure 4.8 shows the normalized number of photon candidates

$(\frac{1}{N}\frac{dN}{d\eta})$ as function of η for different positions of the vertex along the z axis.

Simply examining the plots, we can see that a) differs from b) significantly over all $|\eta| > .35$, but in c) and d), the distribution does not differ for $|\eta| < .7$. We can better quantify this by applying the Kolmogorov test. [36] This test compares two distributions and can be used to calculate the probability that they are compatible, that is, that they are samples taken from the same parent distribution, at a given confidence level. We take advantage of the HDIFF routine provided in HBOOK to do this. This returns the Kolmogorov probability, which has a flat distribution for random samples taken from the same parent distribution. The way we use this test to determine the edge of acceptance is as follows. We plot the η distribution of the photon candidates where the vertex is greater than zero up to some η_{max} and compare it to the η distribution of photons where the vertex was less than zero. We than vary the allowed maximum vertex position and the maximum η to determine the point at which the acceptance begins to drop. The geometry is illustrated in Figure 4.9. The results for three different vertex ranges are plotted in Figure 4.10. The probability varies somewhat, but in each case there is a clear edge where the probability drops drastically. By fitting a function of the form $\tan^{-1}(ax + b)$ to this edge, we can determine a safe combination of cuts on η and z of the vertex.

Based on the studies described above, we make the following fiducial cuts on the photons:

1. EM cluster detector $\eta \leq 1.0$.

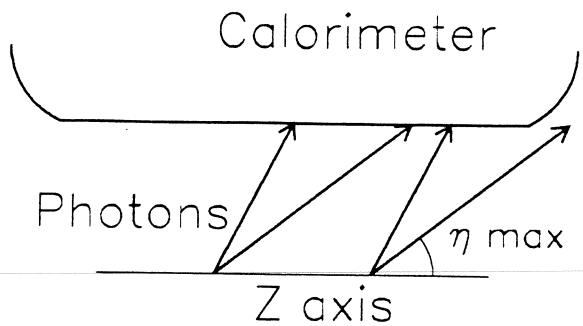

Figure 4.9: An illustration of how the photon acceptance can be determined by using the variation of the vertex position. For a given vertex position along the Z axis, a photon at an angle η_{MAX} no longer hits the calorimeter.

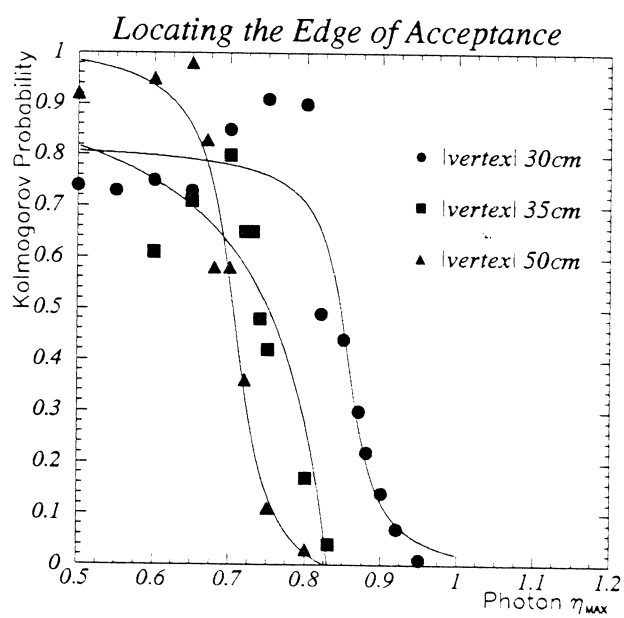

Figure 4.10: The Kolmogorov probability as a function of η_{MAX} for different vertex ranges. Notice the three different "edges".

2. If photon candidate $\eta > 0 \rightarrow z$ position of vertex $\in [-50, 35]$ cm.

3. If photon candidate $\eta \leq 0 \rightarrow z$ position of vertex $\in [-35, 50]$ cm.

4.5 Efficiency as a Function of Angle

We must also be concerned about the η dependance of the detection efficiency of photons. Such a dependance may come about because the calorimeter towers are projective: they point to the nominal interaction vertex at the geometrical center of the detector. Such a geometry offers significant advantages for observing interactions originating at the center of the detector, but if a photon originates from a point on the z axis far from 0, the photon may strike the calorimeter at an angle such that it may deposit energy in more than one tower. But the clustering is tower based, and a photon that crosses towers will appear to leave a shower that is much wider along the z direction than a photon that is parallel to the calorimeter tower where it showers. Unfortunately, this effect can not be studied with the data. We must rely on Monte Carlo simulations. We use the fully detailed detector simulation, DØGEANT, to simulate the response of the calorimeter to photons at various angles and from different vertices. We generate the events with the proper distribution of the z vertex position, in order to take into account the difference between the angle of the photon and the angle of the projective towers. All the cuts are applied to the simulated events, including the fiducial cuts, but excluding the trigger. Notice, however that we are not interested in the absolute value of the efficiency, but rather just the dependence of the efficiency on the angle.

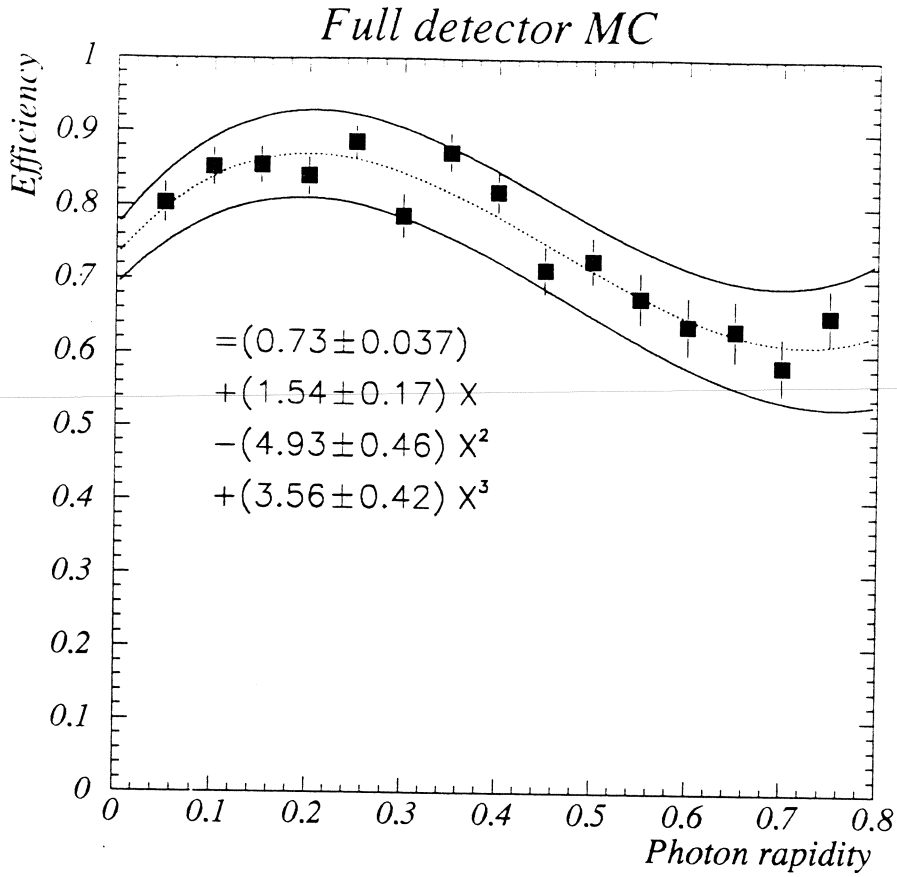

Figure 4.11: The efficiency of the standard photon selection cuts on simulated events. The fit and the errors are shown on the plot. All errors are purely statistical.

We then fit a third order polynomial to the data, in order to parametrize this dependence, with η as the independent variable. The plot is shown in Figure 4.11. With the parameterization of the efficiency in hand, we can correct the photon candidate distribution on an event by event basis, by giving each event a weight equal to the reciprocal of the selection efficiency.

4.6 Energy scale correction

Because the DØ detector does not have a central magnetic field, the absolute energy scale of the calorimeter was determined with a test beam of electrons and pions of known energy. However, in the detector at DØ, the slighlty difference in conditions from those at the test beam resulted in a slightly higher energy scale. This can be corrected by measuring the energies of the electrons from Z boson decays. The mass of the Z has been measured with great precision at LEP, [37] and the energy scale at DØ has been adjusted to give the same mass. This results in about a 5% increase in the energy scale from the test beam calibration. All the analysis described here has been done with this corrected energy scale.

4.7 Jet Reconstruction

We are primarily interested in the measurement of photons, but in order to fully reconstruct the event kinematics, we must also measure the jets in the event. The DØ experiment reconstructs jets using a cone algorithm. This way of defining jets is based on the "Snowmass accord" which was designed to address the thorny question of relating the partons of a theoretical calculation to the "jets" of roughly collinear particles observed in experiments. DØ reconstructs jets with several cone sizes, but for this analysis, we use the $\Delta R = .7$ cone size. That is, all the energy within a distance $\Delta R = \sqrt{\Delta\eta^2 + \Delta\phi^2} < .7$ of the jet axis is summed to form the energy of the jet. The steps used in the

DØ version of this algorithm are as follows:

- Precluster: The calorimeter towers are sorted in descending order in E_T, and a precluster is formed for each tower in turn from all contiguous towers within $|\Delta\eta| < 0.3$, $|\Delta\phi| < 0.3$ with $E_T > 1GeV$. For each precluster, the E_T weighted centroid of the precluster is used to define the axis of the jet candidate. Once a tower has been used in a precluster, it is removed from further consideration. This proccess continues until all towers have been assigned to a precluster or have less than $1GeV$ E_T.

- Cone Clustering: A cone is built for each precluster by including all cells within $\Delta R < 0.7$ and a new centroid is computed. This procedure is then repeated until the centroid becomes stable.

- Merging and Splitting: If two jets share cells after the clustering is done, the fraction of the energy that is shared is examined. If the fraction is greater than 50%, the clusters are merged to form a single jet, and the centroid is recomputed using all the cells of the two clusters. If the shared energy fraction is less than 50%, the clusters are split, and each cell is assigned to the closest cluster.

- E_T Cut: All clusters with more than 8 GeV E_T after merging and splitting, but before jet energy scale corrections, become jets.

Jet reconstruction efficiency, energy corrections and jet resolution have been studied extensively at DØ [39] [40] [41]. The jet energy scale corrections are arrived at using direct photon candidates and the *Missing Projection Fraction*

(MPF) technique. The basic idea is that one chooses events where a good photon candidate is balanced by a single jet and derives the jet energy scale by requiring that the jet balances the photon (on the average, and ignoring the small out of cone corrections). The MPF is defined as:

$$MPF \equiv \frac{\not{E}_T \cdot \hat{n}_j}{E_T{}^j} \tag{4.5}$$

where $\not{E}_T$ is the missing E_T vector, $\not{E}_T \cdot \hat{n}_j$ is the projection of the missing E_T vector into the plane containing the jet axis and the beam axis. Then the jet energy scale can be related to the EM energy scale by:

$$\frac{E_T{}^j}{E_T{}^\gamma} = \frac{1}{1 + MPF} \tag{4.6}$$

All the jets used in this analysis have been so corrected. We will discuss jets in a bit more detail in the next chapter, where we discuss how the parton center of mass system is reconstructed.

Chapter 5

Kinematics

Since the purpose of this analysis is the measurement of the direct photon angular distribution in the center of mass of the hard scattering (CM), we must reconstruct the kinematic variables of the original partonic system. This implies the need to consider jets. This is a drawback, because jet energy resolution is much poorer than the electromagnetic energy scale.

5.1 Jet Energy Resolution

The jet energy resolution is used to smear the theoretical predictions used in this analysis. It has been studied extensively at DØ as it is critical to many analysis such as the inclusive jet cross section or the triple differential jet cross section, and has been described extensively elsewhere. [39] Essentially the jet energy resolution is studied by looking at direct photon events with one jet back to back in ϕ with the photon for jets with relatively low energy, and by di-jet balance for jets of high energy or in the forward region. The result is

Table 5.1: Parameters of the jet energy resolution

η	$N(GeV)$	$S(\sqrt{GeV})$	C
0.0 - 0.8	1.74	0.86	0.016
0.8 - 1.5	7.81	0.349	0.117
1.5 - 3.0	1.97	1.10	0.034

parametrized in the usual way:

$$\left(\frac{\sigma_{E_T}}{E_T}\right)^2 = \frac{N^2}{E^2} + \frac{S^2}{E} + C^2 \tag{5.1}$$

The parameterization is done separately in three regions η corresponding loosely to the CC, ICD and EC. The parameters used for this analysis are listed in Table 5.1.

5.2 Jet η Bias

The accuracy with which the jet is reconstructed is an important issue, because the η of the jet is used to reconstruct the boost of the CM frame relative to the lab frame. Again, the studies done to determine this are fully described elsewhere (see [39], p.130). It was found that there is a bias in the reconstructed η position of the jet, due to the width of the jet in the calorimeter. The bias can be thought of as:

$$\eta_d^{parton} = \eta_d^{reco} + \rho(E, \eta_d), \tag{5.2}$$

where the d subscript refers to the detector coordinates, measured from the center of the detector, as opposed to the the angle measured from the event vertex. This bias is extracted from a Monte Carlo simulation of the detector and fit to a polynomial. A third order polynomial is used in the range of η_d up to 1.8, and a second order fit is used in the range of η_d from 1.8 to 3. The parameters for the fits (which are done in bins of E) are shown in Table 5.2

$$\rho(E, \eta_d) = \alpha + \beta E + \gamma E^2 + \delta E^3 \quad \text{for} \quad |\eta_d| < 1.8 \tag{5.3}$$

and

$$\rho(E, \eta_d) = \alpha' + \beta' E + \gamma' E^2 \quad \text{for} \quad 1.8 < |\eta_d| < 3.0 \tag{5.4}$$

The jets in the data are corrected for this η bias, and the corrected η's are used for the calculations described in the next section.

5.3 Reconstructing CM variables

In principle three variables are required to describe the relationship between the CM frame and the lab frame. However, in practice, the motion of the two incoming partons is assumed to be along the z axis only.

Therefore we require only one variable to describe the relative motion of the two systems. It is convenient to use η_{boost} to describe the Lorentz boost required to transform from the lab frame to the CM frame. As described in Chapter 2, this has a particularly simple form in the case of $2 \rightarrow 2$ process:

$$\eta_{boost} = \frac{\eta_\gamma + \eta_{jet}}{2}. \tag{5.5}$$

Table 5.2: Parameters of the jet η bias fits

Jet Energy	α	β	γ	δ
20 - 40	0.0030	-0.021	0.079	-0.036
40 - 70	0.0016	-0.0011	0.043	-0.022
70 - 100	0.00047	-0.0036	0.039	-0.020
100 - 100	0.00047	0.0074	0.0095	-0.0072
200 - 300	-0.00095	0.0068	0.010	-0.0076
300 - 500	-0.00094	0.016	-0.0086	0.00053
Jet Energy	α'	β'	γ'	δ'
20 - 40	-0.059	0.044	0.0	
40 - 70	-0.072	0.047	0.0	
70 - 100	0.046	-0.077	0.030	
100 - 200	0.0055	-0.026	0.014	
200 - 300	0.012	-0.027	0.012	
300 - 500	0.0059	-0.019	0.0089	

Note that although this can not be thought of as a pseudo-rapidity, because there can be no "massless" approximation for the center of mass, we still call it η_{boost} instead of y_{boost} for simplicity.

In the case where more than one jet must be considered, the η_{boost} may be written as :

$$\eta_{boost} = \tanh^{-1} \frac{p_z}{E}, \tag{5.6}$$

where

$$E = \sum_{i=jets,\gamma} E_i \quad \text{and} \quad p_z = \sum_{i=jets,\gamma} E_{T_i} \sinh \eta_i \tag{5.7}$$

Having reconstructed η_{boost} it is easy to get η^*:

$$\eta^* = \eta_\gamma - \eta_{boost} \tag{5.8}$$

The process is illustrated in the two diagrams which show a hypothetical event in the lab frame (5.1) and in the CM frame (5.2). All the jets are drawn to scale so the interested reader with a ruler and a protractor may verify the claims above.

5.4 Choosing Jets

Because the jet finding algorithm requires a seed tower with a fairly large E_T ($> 1\,\text{GeV}$), the reconstruction of jets is not efficient until above $15\,\text{GeV}$ (d0note2369). We can gauge how well we are able to reconstruct the kinematics

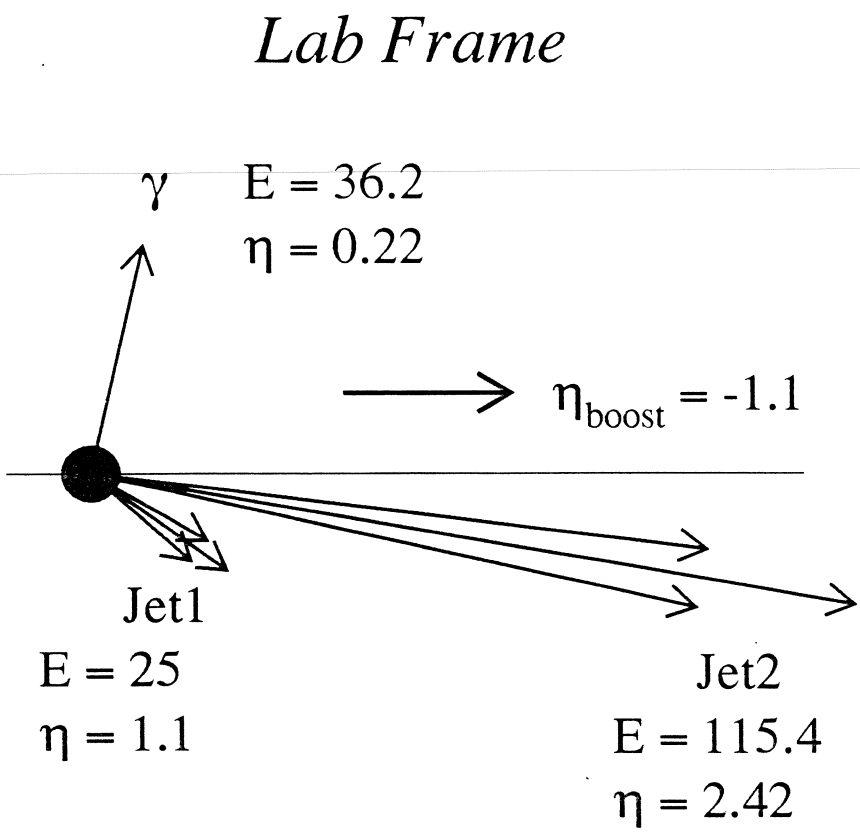

Figure 5.1: A diagram of a hypothetical event in the lab frame.

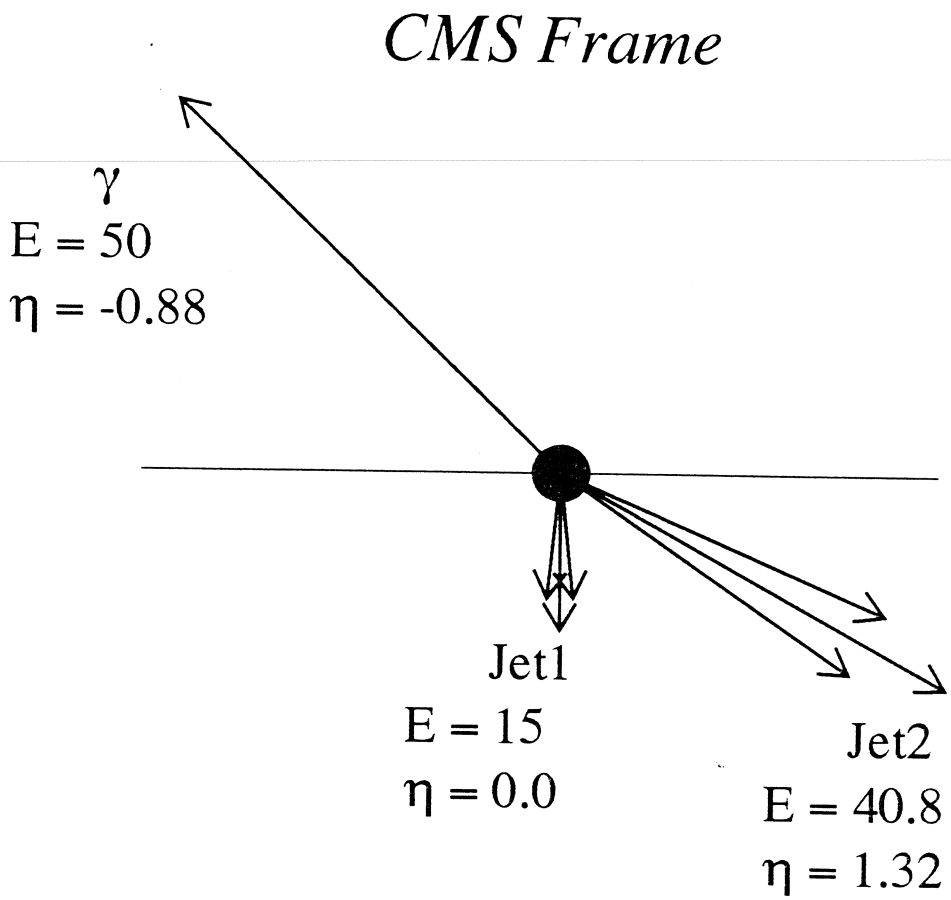

Figure 5.2: A diagram of a hypothetical event in the center of mass frame.

of the event by checking that the vector sum of the momenta of the jets and photons is consistent with small missing E_T.

It is tempting to consider reconstructing the CM variables using only the events with a single jet, because that would allow one to constrain the energy of the jet by assuming that it must have the same E_T as the well measured photon. However, most of the photon candidate events have more than one jet, as shown in Figure 5.3.

Furthermore, the angle in ϕ between the leading jet and the photon shows that even for events that do have only one jet, the improvement in definition of the event is not large compared to the loss of statistics. This is illustrated in Figure 5.4. In other words, the leading jet does as good a job of balancing the photon in events were there is more than one jet as in events where there is only one jet. We conclude that it is not worth discarding the events with more than one jet in order to improve the accuracy with which we can reconstruct the partonic system.

However, it is important to restrict the number of jets allowed in an event. This is due to the low jet reconstruction efficiency for low energy jets. [42], [43] If the jets share energy equally (which is the worst case in terms of jet finding efficiency), then many of the jets may be lost, but the chance that this will happen depends on how the jets are distributed. Unfortunately we can not do an adequate job of simulating the effect this might have on the data, because the next-to-leading order Monte Carlo we use to generate the

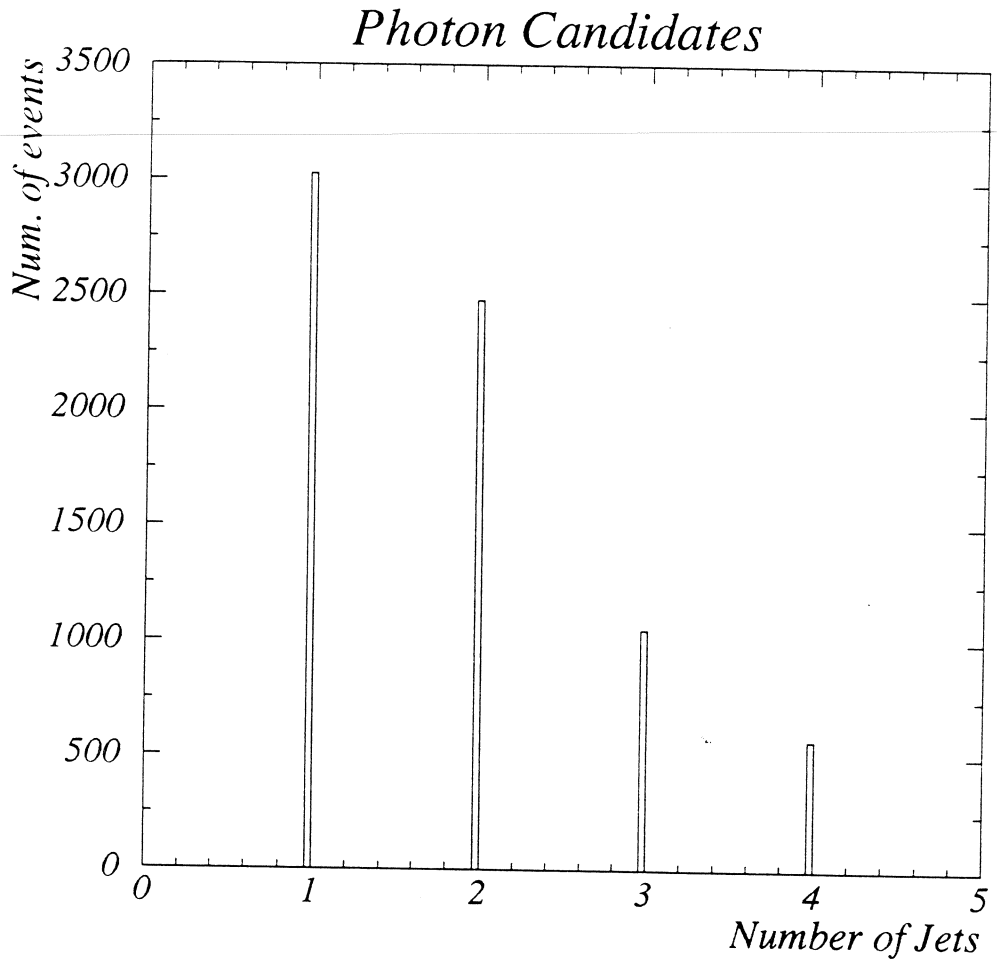

Figure 5.3: Number of jets in photon candidate events.

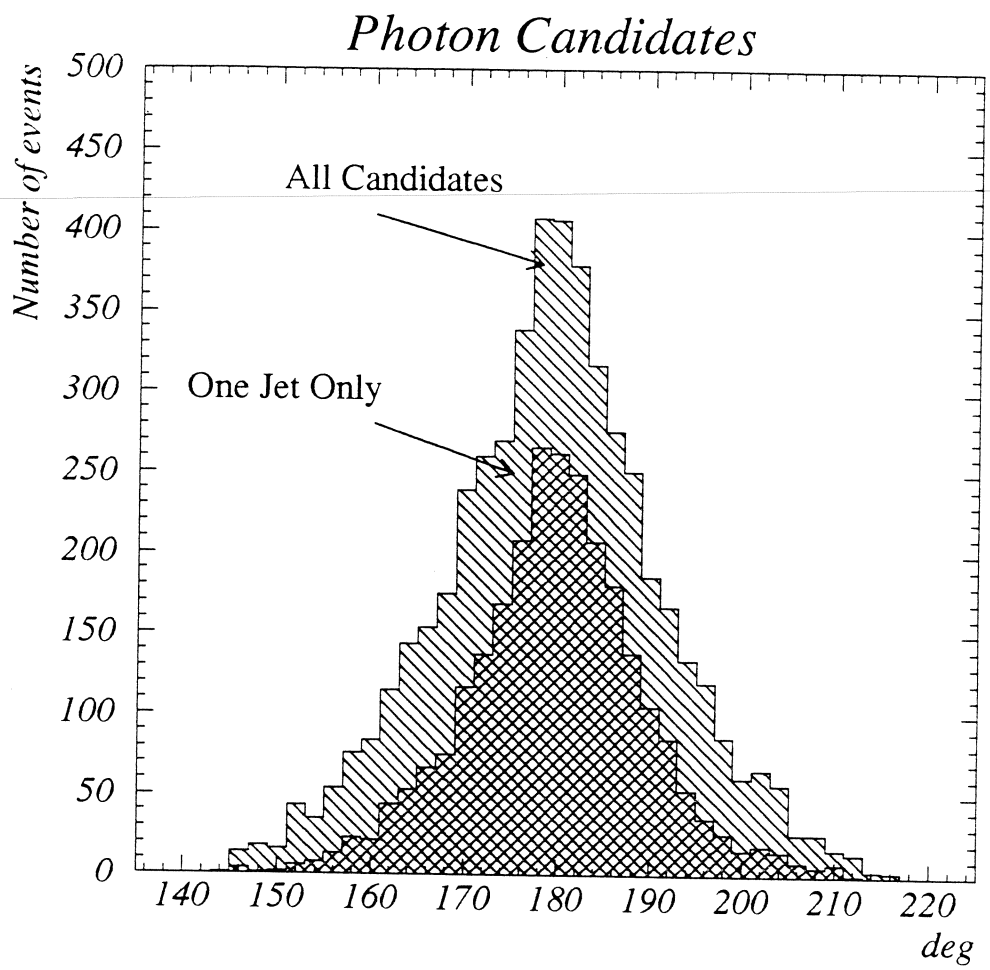

Figure 5.4: The angle in the transverse plane between the photon candidate and the leading jet, in events where only one jet was found, and in events where up to four jets were found.

theory can generate at most only two jets. In view of the above, we choose to limit the analysis to events with only one or two jets.

5.5 Missing E_T cut

As mentioned earlier, the only quantitative information we have on the accuracy with which the jets and photon have been reconstructed is the E_T balance of the event. We can construct a variable which is simply the vector sum of the E_T's of the measured objects in the event and make a cut on this quantity:

$$\not{E}_{T\ reco} = |\vec{E_{T_{jet_1}}} + \vec{E_{T_{jet_2}}} + \vec{E_{T_\gamma}}| < 20GeV. \tag{5.9}$$

Note that this number is not directly related to the $\not{E}_T$ cut made for photon id, because this cut is placed only on the reconstructed objects, whereas the normal $\not{E}_T$ cut uses all the energy in the calorimeter, whether it is associated with a jet or not. The distribution seen in the data for $\not{E}_{T\ reco}$ is in very good agreement with the predictions for this quantity from the smeared Monte Carlo, as shown in Figure 5.5.

5.6 Event Selection

In summary, events must satisfy several different criteria in order to be included in this analysis.

- The event must have a photon candidate with an E_T above 32.5 GeV.

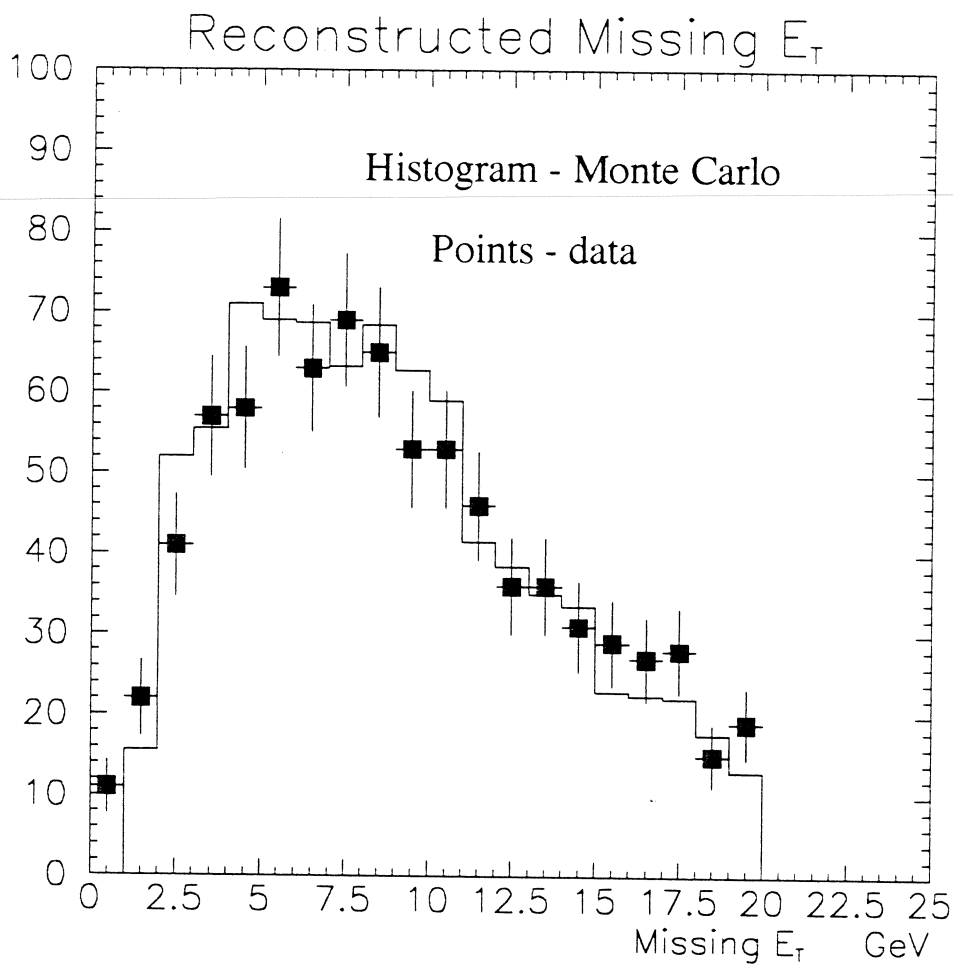

Figure 5.5: The $\not{E}_{T\ reco}$ comparison between data and smeared Monte Carlo. The Monte Carlo has been normalized to the total number of events in the data.

- The photon candidate must pass all standard photon cuts.
- The photon must have $|\eta| < 0.75$
- Events with photon candidates that have positive (negative) η must have a primary vertex which lies within +30 to −50 cm (−30 to +50 cm) of the detector center along the z axis.
- The event must have at least one jet.
- The vector sum of the photon E_T and the E_T's of the two leading jets (ordered in E_T) must be less than $20GeV$. If there is only one jet in the event, then it must balance the photon to within $20GeV$
- Events must lie in regions of phase space where all of the above conditions allow full acceptance.

5.7 Acceptance

At this time, the photon id and background subtraction is not sufficiently well understood in the forward region, and therefore the photon must be constrained to the central region. This constraint has some implications for the kinematic regions accessible for this analysis. By rearranging equation 5.8 we see that a constraint on the maximum η of the photon in the lab frame is equivalent to a constraint on the sum of η_{boost} and η^*:

$$\eta_\gamma = \eta^* + \eta_{boost}. \tag{5.10}$$

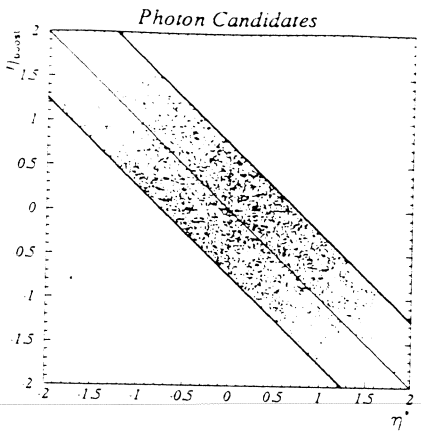

Figure 5.6: A plot of the η_{boost} vs. η^* for photon candidates constrained to lie within $|\eta_\gamma| < 0.75$

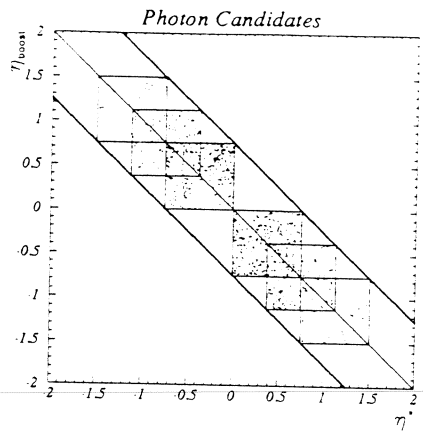

Figure 5.7: Six regions of flat acceptance in η_{boost} and η^* for photon candidates constrained to lie within $|\eta_\gamma| < 0.75$

In other words, the possible photon candidates must lie within a distance of $0.75/\sqrt{2}$ from a diagonal line through the origin on the plot of η_{boost} vs. η^*. This is illustrated in Figure 5.6.

We would like to extract the dependence only on the η^* variable and to integrate over the η_{boost} variable. But that means that we need to pick regions of phase space which are flat in η_{boost}. In other words, we need to choose regions which have borders that run parallel to η_{boost} and η^* axes. We can choose many such regions, six of which are illustrated in Figure 5.7. Since the photon does not distinguish between the proton and the anti-proton, there is no reason to distinguish between $+\eta^*$ and $-\eta^*$, so from we need to consider only $|\eta_{boost}|$ and $|\eta^*|$, but with the understanding that $\text{sign}(\eta^*\eta_{boost}) = -1$.

However, this is not the end of the story for acceptance: we must also be concerned about the momentum of the photon in the CM frame, p_γ^*. This is so because a cut on the photon $p_T$in the lab frame amounts to an implied cut on the p_γ^*, because they are related through

$$p_\gamma^* = p_{T\gamma} \cdot \cosh \eta^* \tag{5.11}$$

and therefore we must require that

$$p_{\gamma min}^* = p_{T min} \cdot \cosh \eta_{max}^* \tag{5.12}$$

and

$$p_{\gamma max}^* = p_{T max} \cdot \cosh \eta_{min}^*. \tag{5.13}$$

This is illustrated in Figure 5.8, which shows the implied cut on p_γ^* which results from the minimum p_T requirement of the trigger. And Figure 5.9 shows how cuts are applied to p_γ^* to assure that each region has flat acceptance in this variable.

So the data for this analysis must be organized into regions which have flat acceptance in η^*, η_{boost} and p_γ^*. For this analysis, we pick three regions, as listed in Table 5.3.

With data restrict to regions of flat acceptance, we can simply project the observed event onto the η^* axis, to get a histogram of $dN/d\eta^*$; or by simple transformation of variable, ($\cos\theta^* = \tanh\eta^*$) a histogram of $dN/d\cos\theta^*$. Such a histogram is shown in Figure 5.10.

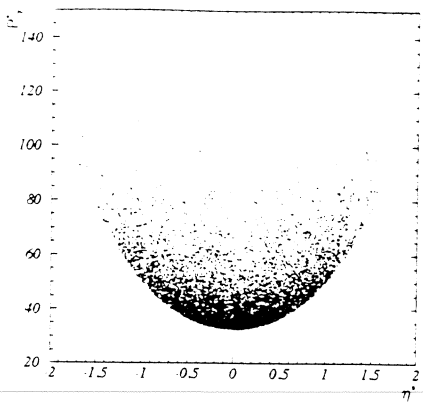

Figure 5.8: The effect of the p_T cut on the data is to exclude events that have $p_\gamma^* < p_{Tmin} \cdot \cosh \eta^*$. This introduces a non-uniform acceptance for events at different values of η^*.

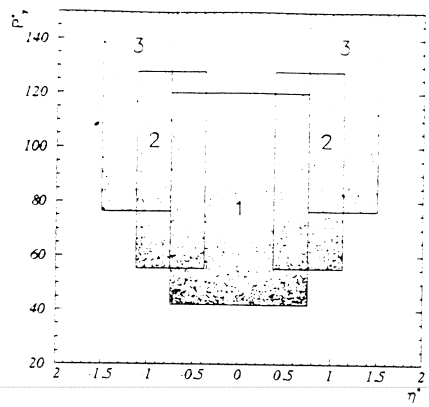

Figure 5.9: An explicit cut on p_γ^* to assure flat acceptance as a function of η^*. Notice that different regions have different cuts. The regions are labeled with numbers.

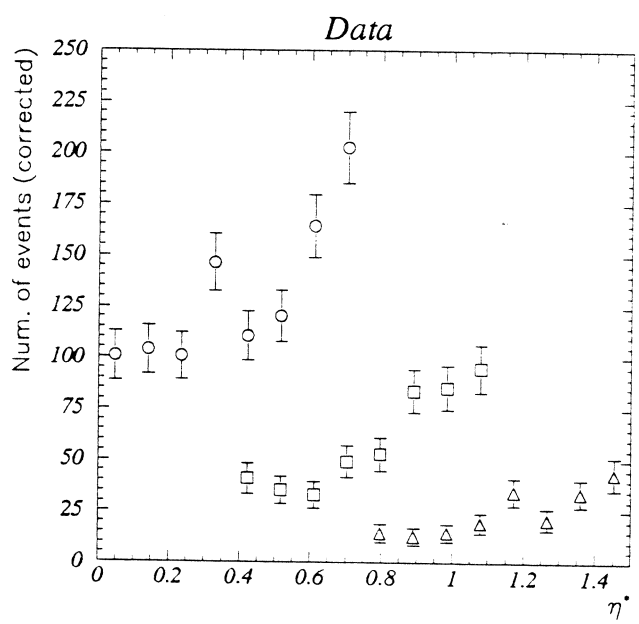

Figure 5.10: The observed number of events plotted vs. η^*, from three different regions.

Table 5.3: Parameters for regions of flat acceptance

Region	$\lvert\eta^*\rvert$ (min - max)	$\lvert\eta_{boost}\rvert$ (min - max)	p_γ^* (min - max) GeV
1	0.0 - 0.75	0.0 - 0.75	42.1 - 120
2	0.375 - 1.125	0.375 - 1.125	55.3 - 128
3	0.75 - 1.50	0.75 - 1.50	76.5 - 155

5.8 Normalization

It is clear from Figure 5.10 that we must somehow normalize the cross section from the three different regions in order to extract one continuous distribution. This can be done by normalizing between the regions in the range of overlap. We can then compare the observed distribution to Monte Carlo based theoretical predictions treated in the same way. However, the question arises immediately as to how meaningful such a procedure is. In other words, is it fair to call a distribution which we extract by some complicated procedure of slicing up phase space into little boxes and gluing them back together a measurement of $dN/d\eta^*$? After all, when someone claims to show a distribution such as $dN/d\eta^*$, there is an unstated implication that the other variable on which the observed cross section depends have been integrated over in some range. This is clearly not the case for the present analysis. But we can still claim that the measured distribution may be fairly called $dN/d\eta^*$ if it is the case that our normalization procedure gives the same result as picking a single bin of η_{boost} and p_γ^* to integrate over. We can not test this hypothesis with data, but we can test it using the direct photon Monte Carlo. We can run

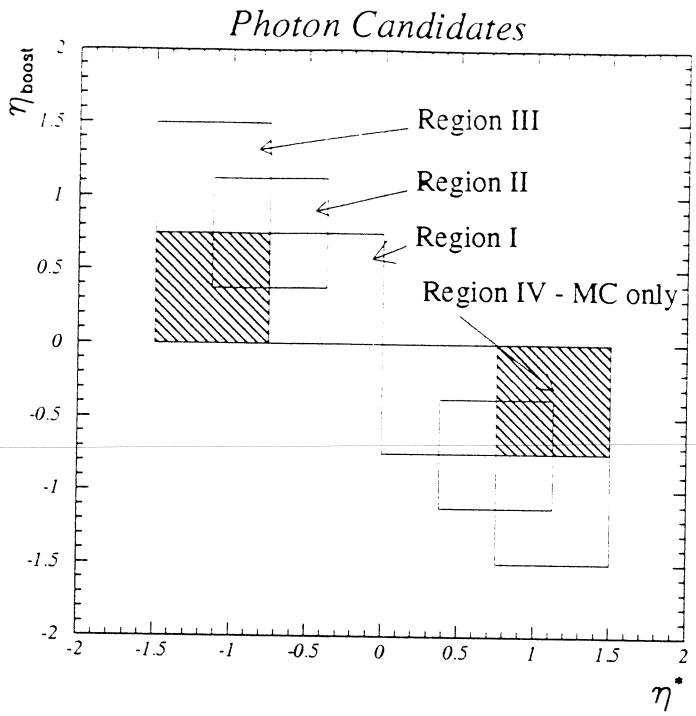

Figure 5.11: The regions of flat acceptance in η_{boost} and η^* used for the data. Since we are interested only in $|\eta^*|$, there are really only three distinct regions. An additional region, which can be studied with Monte Carlo, but not with data is also shown.

the Monte Carlo to simulate the procedure followed in the data and we can also choose a region such that no normalization is required. The relationship of this region to the regions used for the data is illustrated in Figure 5.11

Figure 5.12 shows the simple projection of the three different regions onto the η^* axis. Figure 5.13 shows the result after the normalization procedure. Figure 5.14 shows that in fact, the normalization procedure does not alter significantly the distribution that might be measured in an "ideal" detector. One additional point is worth making again. The difference between the $dN/d\cos\theta^*$

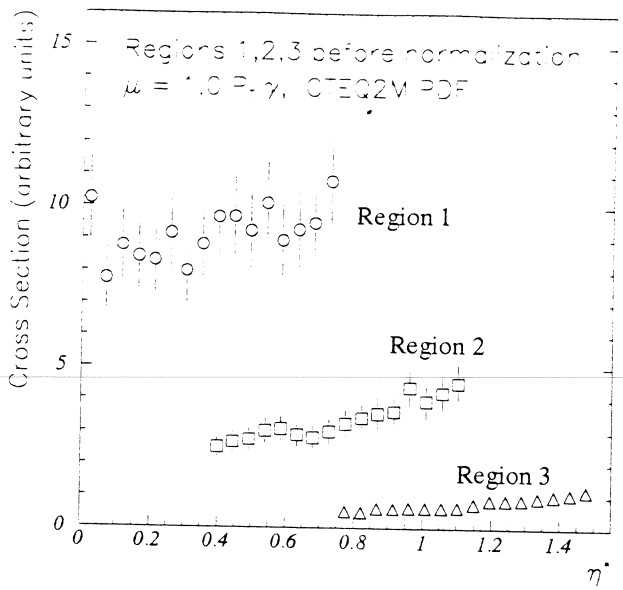

Figure 5.12: Monte Carlo based theoretical prediction of cross section in the three regions as defined in the text.

and $dN/d\eta^*$ is only a change of scale on the x axis; the normalization need not be done separately for the two cases. It is easier to do in the case of $dN/d\eta^*$ because the various regions have simple geometric relationships. The results of applying the normalization used for Figure 5.13 to $dN/d\cos\theta^*$ produces the distribution shown in Figure 5.15 which can be compared to the non-normalized distribution from regions one and four as shown in Figure 5.16.

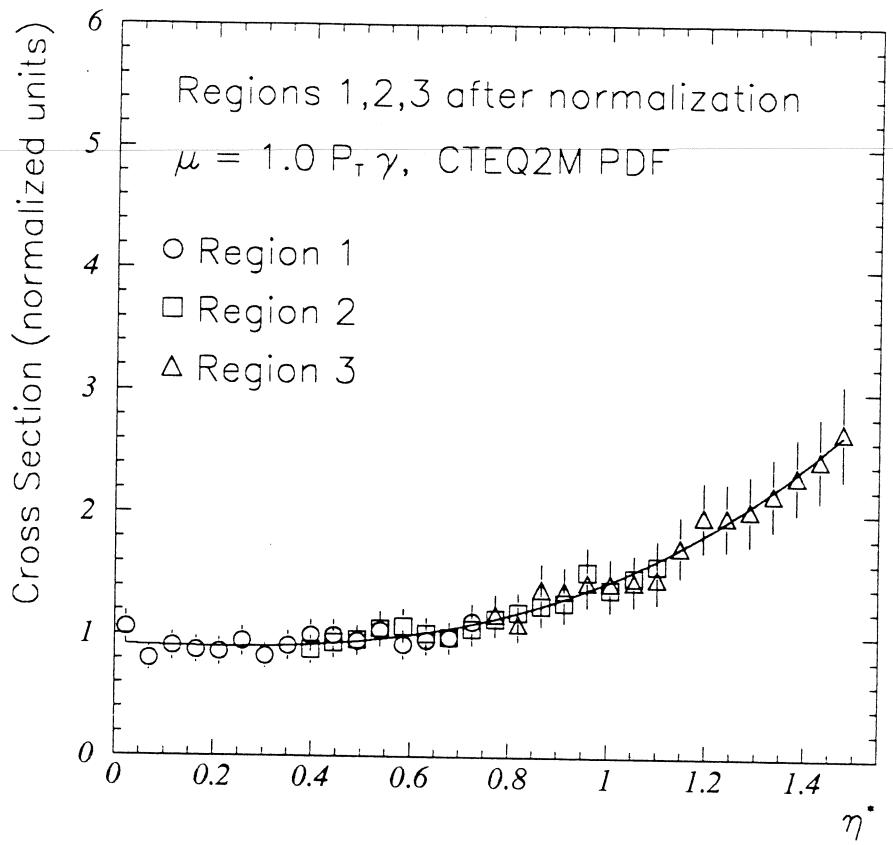

Figure 5.13: Results from Monte Carlo based NLL prediction are shown after being subjected to the same treatment as the data. Monte Carlo was generated in three regions described in the text, and normalized between regions based on the overlap in the same way as the data. The solid line is a polynomial fit to the points.

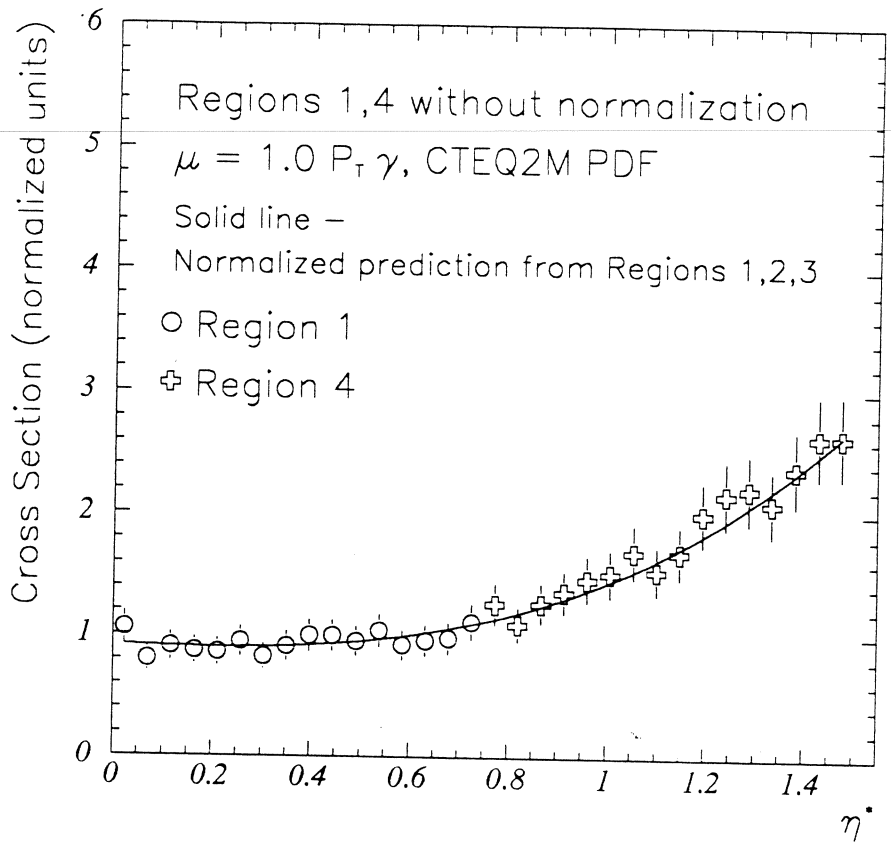

Figure 5.14: Results from Monte Carlo based NLL prediction are shown integrated over a single bin η_{boost} and p_γ^*. The two symbols indicate a division between a region accessible to the real detector and region not accessible in the data. The solid line is a spline fit to the points shown in 5.13.

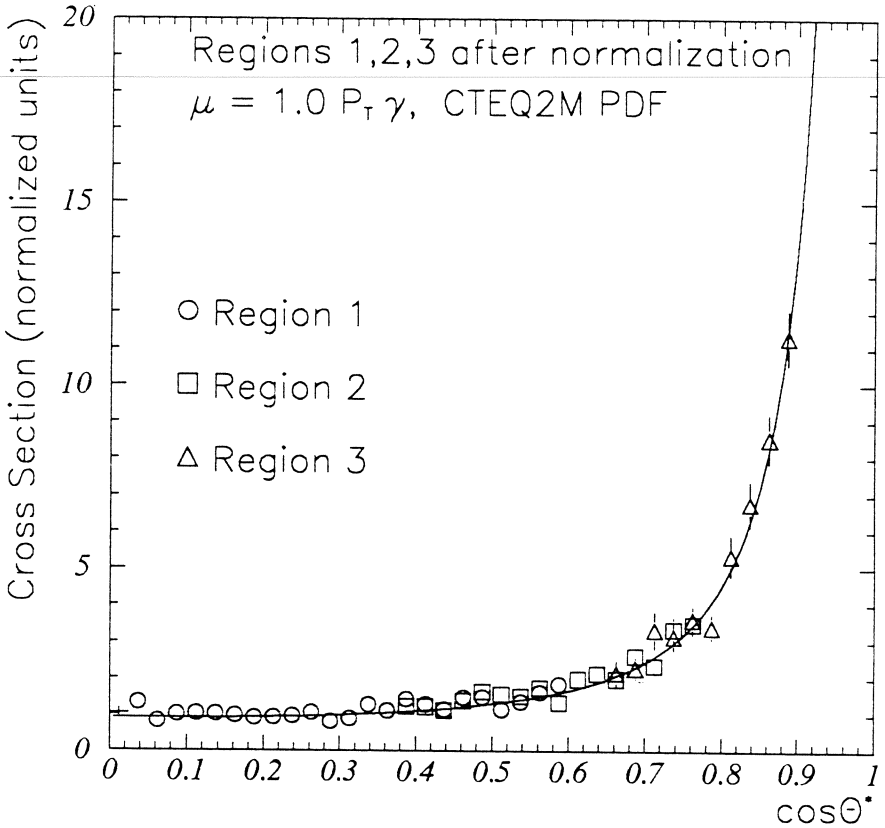

Figure 5.15: Same as 5.13, but plotted vs. $\cos\theta^*$

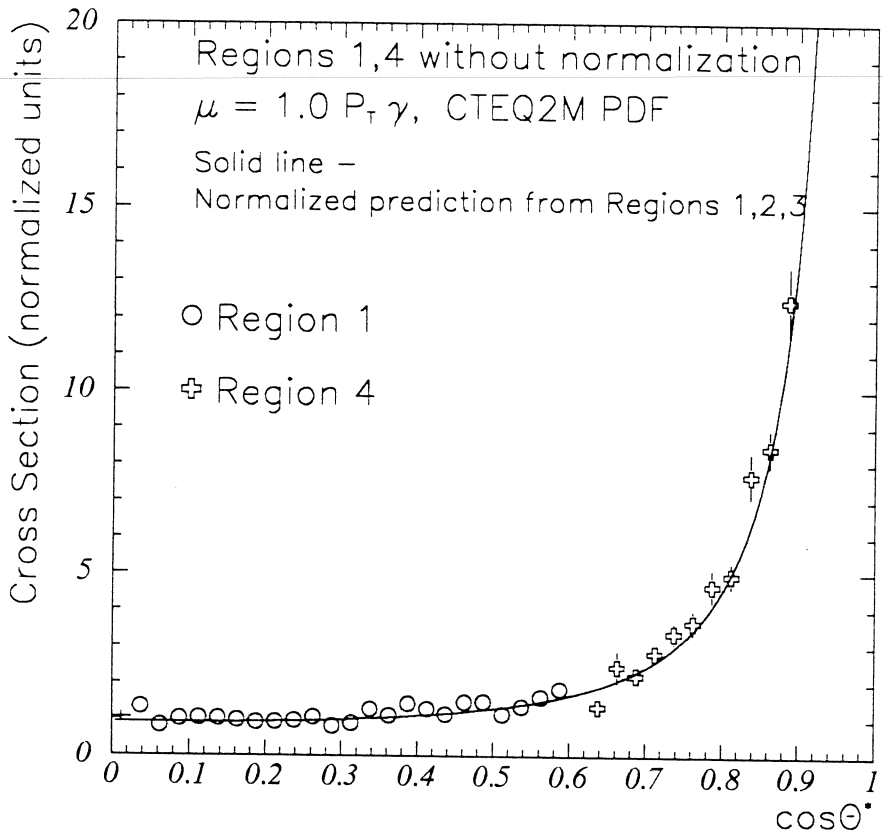

Figure 5.16: Same as 5.14, but plotted vs. $\cos\theta^*$

5.9 Details of the Normalization Procedure

The distributions shown in Figures 5.10 is simply the number of events in each of the regions, in bins of η^*, corrected for efficiency as explained in Chapter 3. There are sixteen bins in the range of $\eta^* \in (0, 1.5)$, with each region covering eight bins, and overlapping the next one in four. There are nine bins in $\cos\theta^*$, each bin being 0.1 units wide, but the region boundaries do not coincide with bin edges.

The actual values are shown in Tables 5.4 and 5.5. The errors are the sum, in quadrature, of the Poisson error on the observed number of events and the error in the efficiency correction.

The data in region 1 is normalized so that the average value for $\cos\theta^*$ in the range of 0.0 to 0.3 (the first three bins) is 1. This gives the first normalization constant, N_0. Other constants are found by taking the ratio of the number of events in the higher region and dividing by the lower region.

$$N_0 = \sum N_{Region1}(\cos\theta^* < 0.3) \tag{5.14}$$

$$N_1 = \frac{\sum N_{Region1}(0.375 < \eta^* < 0.75)}{\sum N_{Region2}(0.375 < \eta^* < 0.75)} \tag{5.15}$$

$$N_2 = \frac{\sum N_{Region2}(0.75 < \eta^* < 1.125)}{\sum N_{Region3}(0.75 < \eta^* < 1.125)} \tag{5.16}$$

The normalized values are found by

$$N^{norm}_{Region1} = \frac{N_{Region1}}{N_0} \tag{5.17}$$

Table 5.4: Observed number of events, binned in η^*

	Region 1			Region 2			Region 3		
Bin	Num. of events	Eff. num of events	Err.	Num. of events	Eff. num of events	Err.	Num. of events	Eff. num of events	Err.
1	87	115.3	12.8						
2	103	131.0	13.5						
3	99	120.5	12.6						
4	140	168.2	15.1						
5	122	147.0	14.0	36	48.8	8.3			
6	123	151.1	14.4	37	47.0	7.9			
7	141	179.8	16.1	32	39.2	7.0			
8	184	246.9	19.7	41	49.2	7.8			
9				61	73.9	9.7	9	11.6	3.9
10				65	81.0	10.3	11	14.2	4.3
11				75	95.7	11.4	10	12.5	4.0
12				95	128.8	13.8	10	12.1	3.8
13							26	31.2	6.2
14							23	28.7	6.1
15							24	31.0	6.4
16							35	48.3	8.3

Table 5.5: Observed number of events, binned in $\cos\theta^*$

	Region 1			Region 2			Region 3		
Bin	Num. of events	Eff. num of events	Err.	Num. of events	Eff. num of events	Err.	Num. of events	Eff. num of events	Err.
1	98	129.6	13.7						
2	107	134.9	13.7						
3	116	140.1	13.7						
4	168	202.3	16.8						
5	165	201.3	16.8	47	60.6	6.4			
6	231	297.8	21.5	56	68.4	9.0			
7				93	112.1	12.1	11	13.9	4.2
8				197	253.6	19.6	29	36.5	6.9
9							96	122.0	13.0

Table 5.6: Normalization coefficient

	Value	Error
N_0	85.8	2.2
N_1	3.83	0.87
N_2	5.28	2.19

$$N^{norm}_{Region2} = \frac{N_{Region2}}{N_0} \cdot N_1 \tag{5.18}$$

$$N^{norm}_{Region3} = \frac{N_{Region3}}{N_0} \cdot N_1 \cdot N_2 \tag{5.19}$$

The errors are propagated in the usual manner as

$$\sigma_y^2 = \sum_i \left(\frac{\partial y}{\partial x_i} \right)^2 \tag{5.20}$$

The results of the normalization procedure are shown in Table 5.7 and Table 5.8 in numerical format and in Figures 5.17 and 5.18 show the results in a graphical format. Figure 5.17 does not show the data from separate regions with different symbols to emphasize that the data lie on a smooth curve. When combining data, in the regions of overlap, only the point with the smaller error is taken.

Since the data is not background subtracted, and we expect a significant amount of background, the difference between theory and data seen in Figure 5.15 and 5.18 is expected. We have to subtract the background and repeat

Table 5.7: Normalized number of events, binned in η^*

	Region 1			Region 2			Region 3		
Bin	N_{norm}	Stat. err.	Tot. err.	N_{norm}	Stat. err.	Tot. err.	N_{norm}	Stat. err.	Tot. err.
1	0.86	0.10	0.10						
2	0.97	0.10	0.10						
3	0.89	0.09	0.10						
4	1.25	0.11	0.11						
5	1.10	0.10	0.11	1.42	0.24	0.28			
6	1.12	0.11	0.11	1.37	0.23	0.27			
7	1.33	0.12	0.12	1.14	0.21	0.24			
8	1.83	0.15	0.15	1.44	0.23	0.27			
9				2.16	0.28	0.36	2.54	0.85	1.00
10				2.36	0.30	0.39	3.13	0.95	1.14
11				2.79	0.33	0.44	2.74	0.87	1.04
12				3.76	0.40	0.55	2.668	0.84	1.00
13							6.86	1.36	1.95
14							6.32	1.33	1.85
15							6.81	1.41	1.97
16							10.611	1.82	2.83

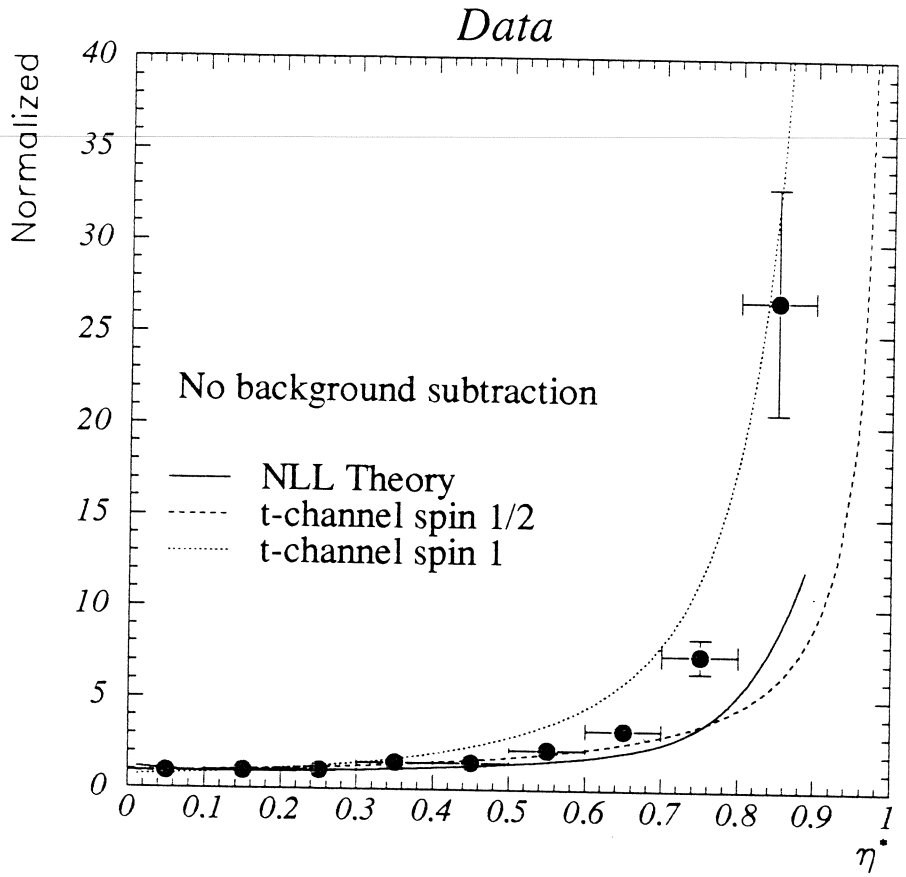

Figure 5.17: Normalized data plotted in bins of $\cos\theta^*$. Inner error bars are statistical only. The outer error bars include the errors in the normalization coefficients.

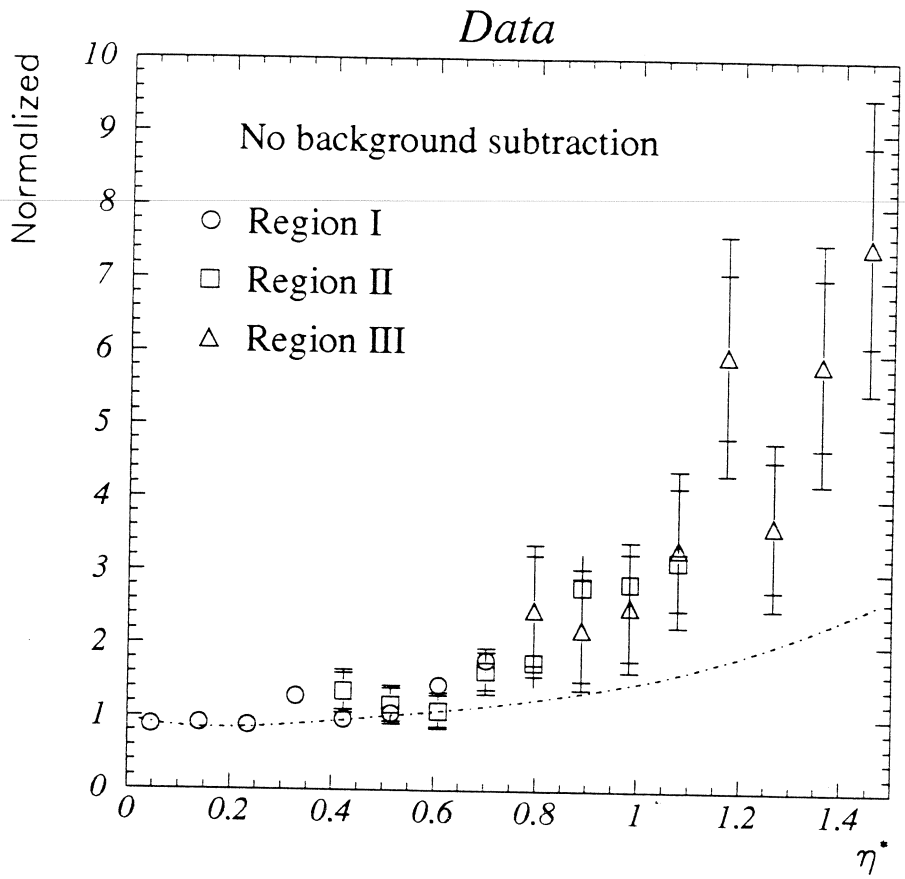

Figure 5.18: The data in bins of η^* after normalization. The line is the theoretical prediction as found in Figure 5.15. In the area of overlap, only the smaller error bars are drawn. Inner error bars are statistical only. Outer error bars include correlated errors due to normalization. The dotted lines are the parton model expectations for the t-channel pole with spin 1 or spin 1/2 exchange.

Table 5.8: Normalized number of events, binned in $\cos\theta^*$

	Region 1			Region 2			Region 3		
Bin	N_{norm}	Stat. err.	Tot. err.	N_{norm}	Stat. err.	Tot. err.	N_{norm}	Stat. err.	Tot. err.
1	0.96	0.01	0.01						
2	1.0	0.01	0.01						
3	1.04	0.01	0.01						
4	1.50	0.12	0.13						
5	1.49	0.13	0.13	1.8	0.26	0.32			
6	2.21	0.16	0.16	2.0	0.27	0.34			
7				3.3	0.35	0.49	3.1	0.93	1.1
8				7.4	0.57	0.95	8.0	1.5	2.2
9							26.8	2.9	6.2

the normalization procedure described here. The background subtraction is the subject of the next chapter.

Chapter 6

Estimation of the Background

We argued in Chapter 2 that the jet cross section can be expected to be about a thousand times larger than the cross section for direct photons at an E_T of about $30GeV$. But only a small fraction of the jets survive the cuts, because jets tend to be composed of many hadrons, which leave significant amounts of energy in the hadronic layers of the calorimeter, and in the isolation cone, at a distance ΔR between 0.2 and 0.4 . However it may happen occasionally that a jet will fragment in such a way that only one particle carries most of the energy of the jet. Furthermore, if this particle happens to be a neutral hadron that decays into photons, it may leave a signature in the detector essentially identical to that of a direct photon. This background is primarily due to π^0 and η mesons with a small additional contribution from K_s^0 [44], but we also considered other mesons such as ρ,ω and $\eta\prime$. Table 6.1 lists the relevant properties of some of these mesons.

Previous experiments studying direct photon production, have been capable of reconstructing the invariant mass of the relevant mesons in at least some

Table 6.1: Properties of electromagnetic neutral meson decays

Particle	Mass (GeV/c^2)	Production cross section relative to π^0	Decay	Branching ratio
π^0	.135	1	$\gamma\gamma$	.99
η	.547	.6	$\gamma\gamma$	.39
η	.547	.6	$3\pi^0$	.32
K_s^0	.498	.4	$2\pi^0$	.31

of the phase space being studied [44]. This requires that the decay products of the meson be separately measured. However, at the energies of interest for this analysis, the DØ calorimeter, although excellent in other ways, does not have anywhere near the spatial resolution required to reconstruct separately the photons resulting from π^0 or η decays. The minimum angular separation for the two photons depends on the energy of the meson in the lab frame and its mass and is given by:

$$\delta = \frac{2m}{E} \tag{6.1}$$

where m is the mass and E is the energy of the meson under consideration. As mentioned in Chapter 3, the size of the cells in the calorimeter is about $.1 \times .1$ in $\eta - \phi$ space. At the first layer of the calorimeter, which is at a radius of about 75cm, this implies cells are approximately square with dimensions 7.5cm on a side. The comparison of the separation between the photons from meson decays to this dimension in shown Figure 6.1. (Figure curtesy of Sal Fahey.)

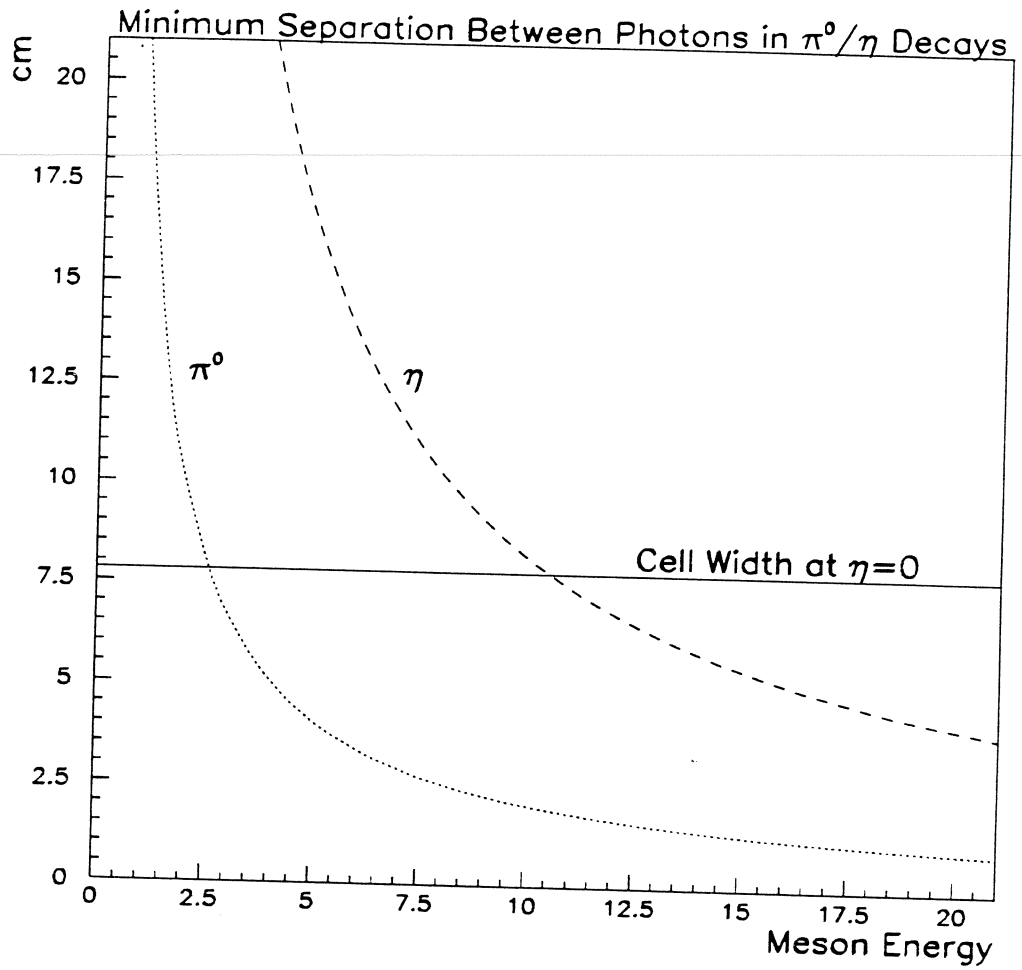

Figure 6.1: Minimum separation between photons from π^0 and η meson decays. The horizontal line denotes the characteristic cell size in the central region.

If the photons from the decay are not separated by at least one full tower, the clustering algorithm will coalesce the two to form a single shower. Therefore, we are unable to reconstruct the invariant mass of neutral mesons using the calorimeter, except for very low energies. However, we can still exploit the fact that showers associated with mesons are composed of more than one photon, in contrast to showers associated with real photons produced directly in the hard scattering.

The basic idea is that high energy photons interact with the matter in the detector primarily through pair production ($\gamma + N \rightarrow e^+e^- + N$). When this pair production happens before the CDC, there is a doubly ionized track left in the tracking chamber. When the pair production occurs in the calorimeter, the electromagnetic shower starts. But given the relatively thin first calorimeter layer, there is a reasonable chance that a photon may not convert there, and therefore leave very little energy in the first layer.

By determining what fraction of photon candidates converts before the CDC, or after the CDC but before the EM1 layer, we can determine on a statistical basis how many of the candidates were single photons, and how many were clusters of coalesced photons from neutral meson decays. If we call the probability that the photon converts before some particular point in the detector ϵ_γ, then the probability that π^0 will convert before that point is closely approximated by

$$\epsilon_{\pi^0} = 2\epsilon_\gamma - \epsilon_\gamma^2 \ . \tag{6.2}$$

That is, the multi-photon backgrounds are more likely to convert than genuine

single photons. The formula is not exact, because the two photons from the meson decay carry only part of the energy of the candidate cluster, and therefore will interact with the detector slightly differently from the single photon with the same total energy. Additionally, although most π^0's will decay into photons of nearly equal energies, some may decay asymmetrically, so that one of the photons is undetectable because its energy is too low.

6.1 Calorimeter Method

Ideally we would like to measure the number of converted photons at a point where the difference between ϵ_{π^0} and ϵ_γ is as large as possible. Because the cryostat in DØ is fairly thin, the first layer of the calorimeter is a good candidate for such a measurement. A substantial fraction of photons will traverse the first layer leaving very little energy, while the decay products of a neutral meson are much more likely to deposit a substantial fraction of the total energy. This is illustrated in Figure 6.2. (Figure courtesy of Sal Fahey.)

If we choose a cut that has an efficiency ϵ_γ, ϵ_π for photons and background respectively, and we observe that our sample has efficiency ϵ_{data} for this cut, then we can model our data as a mixture of photons and background:

$$\epsilon_{data} N_{data} = \epsilon_\gamma N_\gamma + \epsilon_\pi N_\pi \tag{6.3}$$

The cut used for this analysis is

$$\frac{\text{energy in EM1}}{\text{total cluster energy}} < 1\%. \tag{6.4}$$

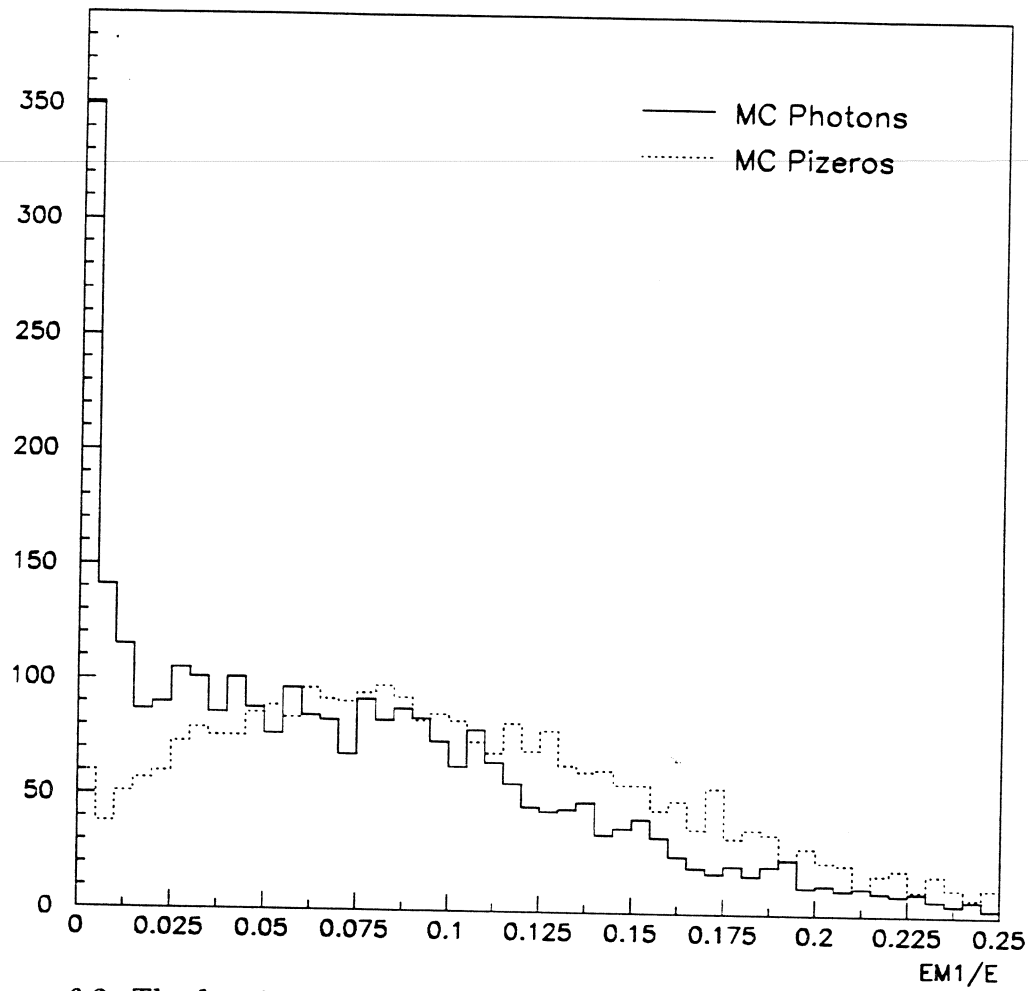

Figure 6.2: The fractional energy deposited in the first layer of the calorimeter for simulated photons and π^0s.

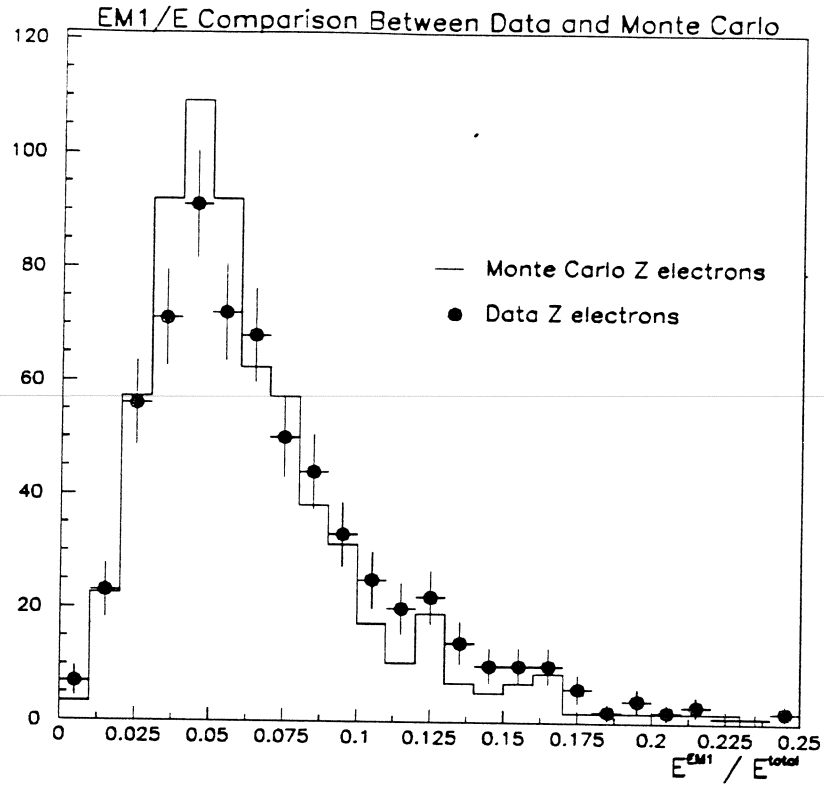

Figure 6.3: The fractional energy deposited in the first layer of the calorimeter for simulated photons and π^0's.

The value of the cut is chosen in order to maximize the difference between ϵ_γ and ϵ_π, but the final result for N_γ should, in principle, be independent of the cut value. Because of differences between Monte Carlo and data, the result is not completely independent, but varies slightly. This is included in the estimate of the systematic error for the background subtraction. Another way data can be compared with Monte Carlo is by comparing the energy deposited in the first layer by electrons from Z boson decays to the Monte Carlo predictions. This check indicates that the Monte Carlo is in good agreement

with the data as shown in Figure 6.3 (Figure courtesy of Sal Fahey.)

6.2 Calculation of the Signal Fraction in the Data

Knowing ϵ_γ,ϵ_π and ϵ_{data} is sufficient to calculate what fraction of the candidate sample is signal. But in practice, we know that ϵ_γ and ϵ_π are functions of the photon E_T and η. The dependance on η is especially easy to understand, because the central calorimeter is cylindrical, the amount of material upstream of the first EM layer varies inversely with $\sin\theta$ where θ is the angle of incidence with respect to the normal. That means that the Monte Carlo used to calculate ϵ_γ and ϵ_π must match the η and E_T distributions of the candidate events found in the data. This is possible if one of the distributions is particularly simple. For example in the direct photon cross section analysis, the η distribution of the candidate events is expected (and found) to be flat in η, independent of E_T. In that case it is possible to generate Monte Carlo data with a flat η distribution at several different points in E_T and by fitting a smooth curve to the points, to arrive at the appropriate estimates of the signal and background efficiency. This is the approach taken in the analysis of the inclusive direct photon cross section. [30]

However, this approach is not practical for the angular distribution analysis – because the η distribution of the candidates is not flat, and it is critically important to have the correct background estimate as a function of η. In or-

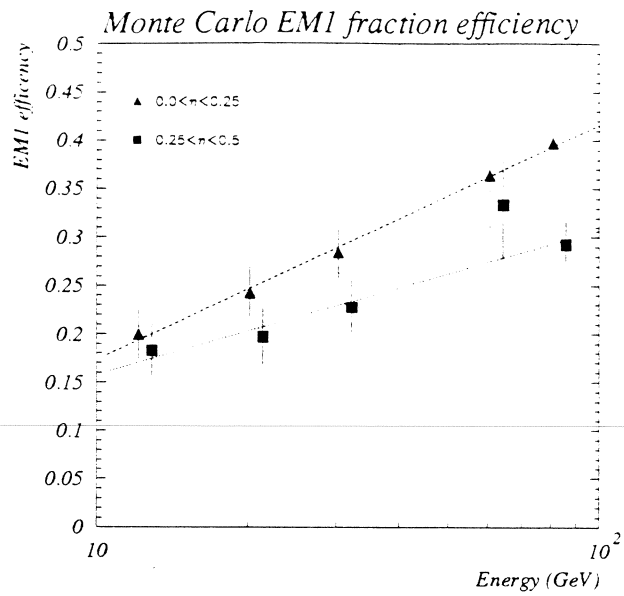

Figure 6.4: A plot of ϵ_γ for two different ranges of η as a function of E. Notice the log scale on the x axis.

der to accomplish this we must explicitly parametrize the efficiencies for pure background and pure signal as functions of η and E_T by fitting a smooth function to the Monte Carlo at several different points. The variation of ϵ_γ and ϵ_π is shown in the Figures 6.4 and 6.5.

$$\epsilon_\gamma = f(\eta, E), \quad \epsilon_\pi = g(\eta, E) \tag{6.5}$$

Then, we can assign a weight to each event, according to whether it has passed the discriminant cut (EM1 energy $< 1\% E_\gamma$) or failed as follows:

$$\text{If / } E_{EM1} < 1\% E_\gamma \quad \rightarrow w = \frac{1-\epsilon_\pi(\eta,E)}{\epsilon_\gamma(\eta,E)-\epsilon_\pi(\eta,E)}. \tag{6.6}$$

$$\text{If / } E_{EM1} > 1\% E_\gamma \quad \rightarrow w = -\frac{\epsilon_\pi(\eta,E)}{\epsilon_\gamma(\eta,E)-\epsilon_\pi(\eta,E)}. \tag{6.7}$$

With written the ϵ_γ and ϵ_π as functions of η and E_T as a reminder that these

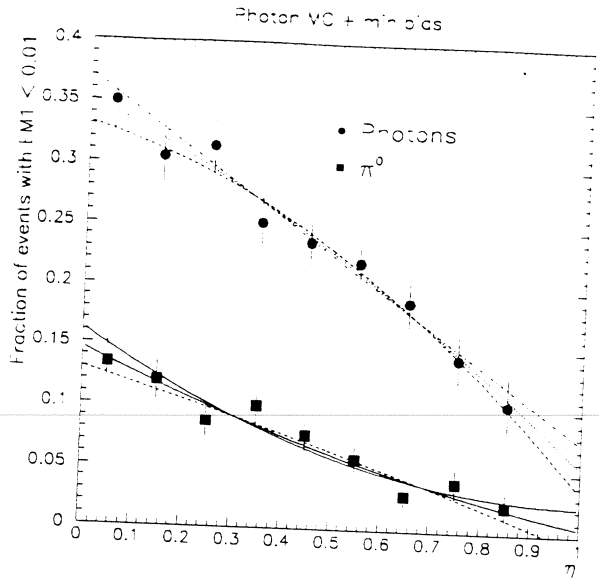

Figure 6.5: A plot of ϵ_π and ϵ_π as a function of η.

will in general be different for every candidate event. Then the sum of the weights is our best estimate of the number of direct photons in any given sample, and the statistical error on this estimate is simply the sum of the squares of the weights:

$$N_\gamma = \sum_{i=1}^{N_{pass}} w_{pass} + \sum_{i=1}^{N_{fail}} w_{fail} \tag{6.8}$$

$$\sigma_{N_\gamma} = \sum_{i=1}^{N_{pass}} w_{pass}^2 + \sum_{i=1}^{N_{fail}} w_{fail}^2 \tag{6.9}$$

This formulation is identical to the usual form,

$$N_\gamma = N\frac{\epsilon_{\text{data}} - \epsilon_\pi}{\epsilon_\gamma - \epsilon_\pi}, \tag{6.10}$$

in the case where we know the proper estimate of ϵ_π and ϵ_γ for the given candidate sample under consideration. The advantage of summing the weights is that this is done automatically. An example of how this works is shown in

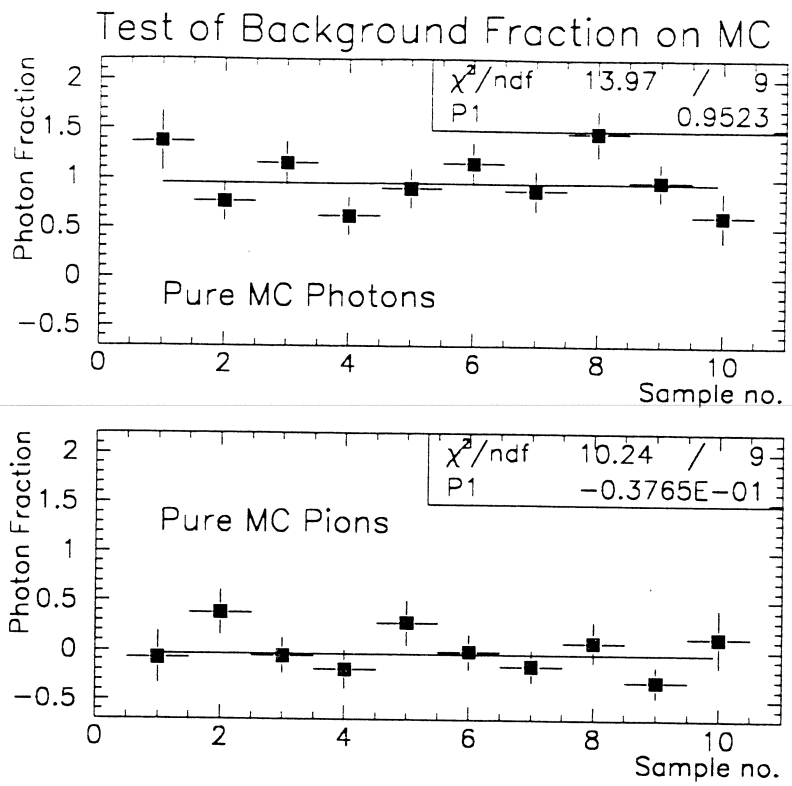

Figure 6.6: N_γ/N for Monte Carlo pions and photons over the range of interest for the angular distribution analysis.

Figure 6.6. We plot N_γ/N for Monte Carlo photons and π^0 for events at several different energies from 30GeV to 120GeV E_T and covering η from 0 to 0.75.

The parameterization used for this analysis was

$$\epsilon_\pi = -0.03 + 0.043\log(E) + 0.072|\eta| - 0.209|\eta|^2 \tag{6.11}$$

$$\epsilon_\gamma = -0.015 + 0.10\log(E) - 0.351|\eta| + 0.191|\eta|^2 \tag{6.12}$$

It has been optimized to give the best agreement with Monte Carlo in the regions of ϵ_γ and ϵ_π of interest for this analysis:

$$\eta \in [-0.75, 0.75] \text{ and } E \in [30, 80]$$

Table 6.2: Signal Fraction in the Data Sample

Region	Fraction	Statistical Error	Systematic Error
1	0.62	0.087	0.06
2	0.50	0.13	0.06
3	0.66	0.21	0.06

The disadvantage of this background subtraction method is a small additional systematic error, associated with the accuracy of the parameterization. This error has been estimated to be 0.03 by varying the points and redoing the fits. In addition the error due to uncertainty in the modeling of the detector and the variation of the η/π^0 production ratio is estimated to be the same as for the cross section analysis. [50]

The results of applying the calorimeter background subtraction method to the events under consideration is summarized in Table 6.2

6.3 Central Drift Chamber Method

As described earlier, the difference in the rate of conversions between true direct photons and backgrounds from neutral meson decays can be applied to the probability that a candidate event is found with an associated track in the CDC [1]. In order to do this, events in the candidate sample are divided into

[1]The work described here is explained in more detail in [51]

three categories:

- Candidates without a track. These events must have no track pointing to the centroid of the calorimeter cluster within the full tracking road ($\delta\eta = \pm 0.1, \delta\phi = \pm 0.1$).

- Candidates with track ionization compatible with one minimum ionizing particle (*mip*). These events are consistent with a single minimum ionizing track within the CDC, pointing closely to the candidate cluster (track match significance < 5). For the purposes of this analysis, tracks with ionization below 1.4 in the CDC are said to be minimum ionizing. This is the type of event most likely to be caused by a high energy electron.

- Candidates with a two *mip* track. These events are consistent with a single doubly ionizing track within the CDC, pointing closely to the candidate cluster (track match significance < 5). For the purposes of this analysis, tracks with ionization above 1.4 in the CDC are said to be doubly ionizing. This is the type of event most likely to result from a conversion of a photon in the material upstream of the CDC.

Events which do not belong to one of the above three categories are excluded from the analysis. Notice that the sample for this background subtraction method is a superset of the candidates for the calorimeter method. In both samples, candidates that have a track within the full road, but failing the track significance cut are excluded.

6.4 Matrix Formulation

The three categories of candidates are used to reconstruct the three types of particles on a statistical basis, by determining a matrix that describes the probability that a particular particle will be observed as an event of a certain category. In other words we construct a 3×3 matrix such that

$$\begin{pmatrix} 0\,mip \\ 1\,mip \\ 2\,mip \end{pmatrix} = \begin{pmatrix} 3 \times 3 \\ transformation \\ matrix \end{pmatrix} \begin{pmatrix} N_\gamma \\ N_e \\ N_\pi \end{pmatrix}. \tag{6.13}$$

By inverting this transformation matrix, we can solve for the signal fraction of the original sample, based on the number of candidates that fall into each of the three categories. In order to construct the transformation matrix, we break down in detail the process of how particles interact with the detector. This clearly requires very good understanding of the detector and it's performance. In many cases it is possible to measure the required quantities, but in some cases, we must rely on the Monte Carlo to model some aspects of the detector. The desire to rely as little as possible on Monte Carlo is what accounts for the apparent complexity of the matrix formulation.

The first step is to consider the possibility that the underlying event contributes a neutral meson close to the candidate event. Such an overlap may cause a direct photon event to appear as background if the neutral meson from the underlying event converts and leaves a track within the road. This parameter can be estimated directly from the data by studying the probability of charged particle overlaps, (which is discussed in more detail below), and estimating that about 1/3 of the particles in the underlying event are neutral

mesons. This parameter (V_1) is quite small ($< 1\%$), and is known to have a very small effect on the final estimate of the signal fraction. But it is included here for completeness. The matrix that is applied to the vector of 'true' particles is:

$$\begin{pmatrix} neutral \\ overlaps \\ matrix \end{pmatrix} = \begin{pmatrix} 1-V_1 & 0 & 0 \\ 0 & 1 & 0 \\ V_1 & 0 & 1 \end{pmatrix} \tag{6.14}$$

The next step describes the probability that a photon will convert into a e^+e^-pair as well as the various possibilities for the disposition of tracks in the detector to account for the finite efficiency and ionization resolution of the CDC. Some of the parameters in this step can be measured from data. Others must be deduced from Monte Carlo simulations of the detector. The matrix is:

$$\begin{pmatrix} conversions\ \& \\ ionization \\ matrix \end{pmatrix} = \begin{pmatrix} 1-P & 0 & (1-P)^2 \\ L_1P & Y & 2L_2P(1-P) \\ S_1P & X & 2S_2P(1-P) \end{pmatrix} \tag{6.15}$$

The probability that a photon converts is P. It must be deduced from Monte Carlo. The L parameter represents the limitations of the ionization measurement. L_1 is the probability that a track from a converted photon is categorized as single ionizing. L_2 is the corresponding probability for neutral meson. This can be caused by multiple scattering of the electrons in the pair making the track, and as consequence depends on the energy of the electrons themselves, and the photon before the conversion. This is why L_1 and L_2 are different. These parameters are are extracted from Monte Carlo. S_1 and S_2 are the complimentary parameters that quantify the probability that a converted photon or neutral meson are identified as doubly ionizing tracks. These must

also be independently determined from Monte Carlo, because $L_1 + S_1$ and $L_2 + S_2$ need not equal one. Finally, X and Y represent the probability that a track left by a single charged particle (such as an electron) will be identified as singly ionizing (Y) or doubly ionizing (X). These parameter are determined from the data, based on the observed ionization of electrons in Z boson decays.

The next step in the chain is to account for the possibility that the underlying event will contribute a charged particle (such as a pion) that leaves a track close to the photon candidate by "accident". The matrix is:

$$\begin{pmatrix} charged \\ overlaps \\ matrix \end{pmatrix} = \begin{pmatrix} 1-V_3 & 0 & 0 \\ V_2 & 1-V_3 & 0 \\ 0 & V_2 & 1-V_3 \end{pmatrix}. \tag{6.16}$$

There are two different values, V_2 and V_3 [2] because of track match requirement: a charged track anywhere within the very wide ($\delta\eta = \pm 0.1, \delta\phi = \pm 0.1$) tracking road will disqualify the event as "photon", but the track must have track match significance < 5 in order for the event to be characterized as a singly ionizing candidate. As mentioned earlier, the value of V can be determined from the data. By looking at Z events, and constructing a fictitious road perpendicular to the plane of the decay, we can measure the rate of accidental overlaps. The details of the determination of these quantities may be found in [51]

The final step in the construction of the full matrix is the tracking efficiency matrix, which accounts for the loss of good tracks in the CDC due to physical limitations of the chamber, or limitations of the reconstruction soft-

[2] Recall that V_1 is the neutral particle overlap probability

ware. The tracking efficiency has been measured using Z and W boson events. The matrix is:

$$\begin{pmatrix} tracking \\ efficiency \\ matrix \end{pmatrix} = \begin{pmatrix} 1 & 1-T & 1-T \\ 0 & T & 0 \\ 0 & 0 & T \end{pmatrix}. \tag{6.17}$$

The final matrix, then is constructed as follows:

$$\begin{pmatrix} 0\,mip \\ 1\,mip \\ 2\,mip \end{pmatrix} =$$

$$\begin{pmatrix} tracking \\ efficiency \\ matrix \end{pmatrix} \begin{pmatrix} charged \\ overlaps \\ matrix \end{pmatrix} \begin{pmatrix} conversions\ \& \\ ionization \\ matrix \end{pmatrix} \begin{pmatrix} neutral \\ overlaps \\ matrix \end{pmatrix}$$

$$\times \begin{pmatrix} N_\gamma \\ N_e \\ N_\pi \end{pmatrix} \tag{6.18}$$

This final matrix is inverted with the aid of $MAPLE$ mathematics package, and the inverted matrix is applied to the observed numbers of candidates in each of the three categories (0 mip, 1 mip and 2 mip). The results of this method of background estimation are found to be consistent with the estimates from the calorimeter method. [30] However, because of the larger errors, we use the CDC method only to confirm the calorimeter result.

But, the estimate of the background fraction is far from the end of the story for background subtraction. There are several data points that we wish to measure in each region, and therefore one estimate of the background region for the *entire* region is inadequate. We must somehow find the background

Table 6.3: CDC Conversion Method Parameters.

Parameter	Value
V_1	0.01 ± 0.010
V_2	0.01 ± 0.002
V_3	0.075 ± 0.005
X	0.022 ± 0.001
Y	0.931 ± 0.005
L_1	0.009 ± 0.004
L_2	0.031 ± 0.010
S_1	0.940 ± 0.005
S_2	0.852 ± 0.050
P	0.100 ± 0.005
P	0.087 ± 0.040

fraction changes from point to point in each particular region- in other words, we must find the *shape* of the background.

6.5 Background Shape

The obvious way to get shape of the background is to measure it by selecting the "poor quality" photon candidates. However, if we could reliably identify fake photons, we would simply remove them from the sample. Instead, we apply the same idea, but in a sightly different way. We know that isolated neutral mesons are formed in the jet fragmentation process, so they should have the same angular distribution as jets. Since jets are very plentiful, it is not difficult to get an accurate distribution. In order to justify the validity of this approximation in the face of experimental evidence that quarks are more likely to fragment in to a single particle than gluons [48], we studied the fraction of gluon jets as a function of $\cos\theta^*$. This can be done using the HERWIG [3] event generator. [52] The results of the study are shown in Figure 6.7. We conclude from the results that the approximation is justified.

The procedure to measure the jet angular distribution is as close as possible to that used for photon candidate data. The standard QCD inclusive jet sample from Run 1A is taken as the starting point. For each event, a jet in the range $|\eta| < 0.75$ and with $E_T$above some threshold is chosen to serve as

[3]Herwig is a Monte Carlo event generator for simulating Hadron Emission Reactions With Interfering Gluons.

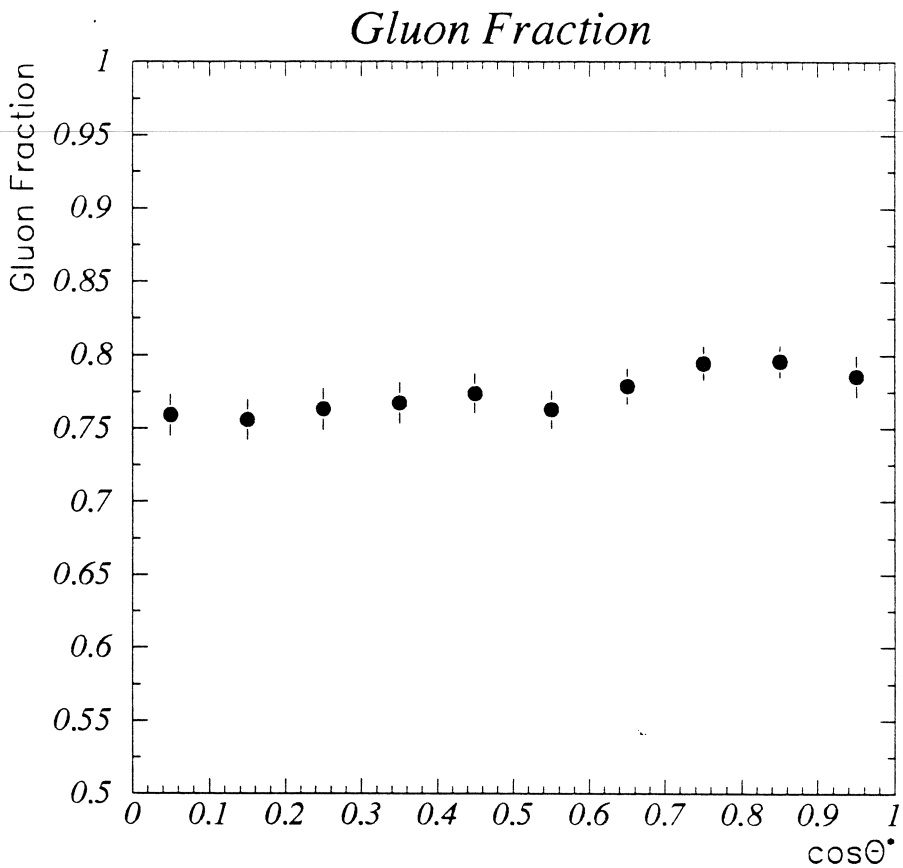

Figure 6.7: The predicted ratio of gluon jets to all jets as a function of $\cos\theta^*$ using the HERWIG Monte Carlo.

the "photon". If there is more than one jet which satisfies these requirements, one is chosen at random. This avoids bias without unnecessarily losing events. Once a jet is chosen, it's identity is changed in software into a perfect photon. In other words, variables used to select photon candidates are filled with ideal values – the electromagnetic fraction is set to 100%, the energy in the isolation cone is set to zero, and so on. Then the event is written out in standard format, and from then on, it goes through the analysis like any other photon candidate. The only information remaining from the jet is the η and the E_T. In this way, we can determine the angular distribution of jets.

Unfortunately, things are not quite that simple. The jet data is taken with different triggers from the photon data, and is heavily prescaled (not surprisingly). It happens that there is no trigger with a threshold close to that of the photon trigger, but there is one that turns on around $30GeV$, called JET_MIN, and one that turns on at a little above $40GeV$, called JET_LOW. [39](p.104) The lower trigger, JET_MIN, has less data. We can choose to use the lower of the two triggers, and impose the same E_T threshold as on the photon candidate data, and accept the lower statistics. Or we can use a higher threshold on the JET_LOW trigger, and risk introducing a bias. In the end, we chose the later – we use the JET_LOW trigger, with a $43GeV$ threshold because the statistics for this trigger are *much* better and because it turns out that the two sets of data are very nearly equal, and within statistical errors of each other in every bin except one (out of 24 bins). Note that the angular distribution of jets has been studied previously at DØ [53] and the results presented here have been found to be in good qualitative agreement with the previous analysis. The

Table 6.4: Observed number of jet events, binned in η^*

	Region 1			Region 2			Region 3		
Bin	Num. of events	Eff. num of events	Err.	Num. of events	Eff. num of events	Err.	Num. of events	Eff. num of events	Err.
1	352	465.4	28.4						
2	379	483.1	28.7						
3	459	564.5	31.3						
4	553	666.3	34.6						
5	629	756.2	37.7	151	197.8	17.1			
6	815	996.6	45.9	196	245.6	19.0			
7	1030	1297.8	56.1	224	274.4	20.1			
8	1318	1734.6	70.6	276	331.1	22.2			
9				384	461.3	27.3	43	53.6	8.3
10				494	609.1	32.9	51	62.5	8.9
11				594	759.4	38.5	63	76.1	9.8
12				787	1056.3	49.2	79	94.1	10.9
13							93	112.7	12.1
14							126	156.5	14.7
15							176	231.2	18.7
16							238	328.1	23.4

observed number of jets as a function of η^* are shown in Figure 6.8 and listed in Table 6.4 for each region.

Assuming that the angular distribution of jets represents the angular dis-

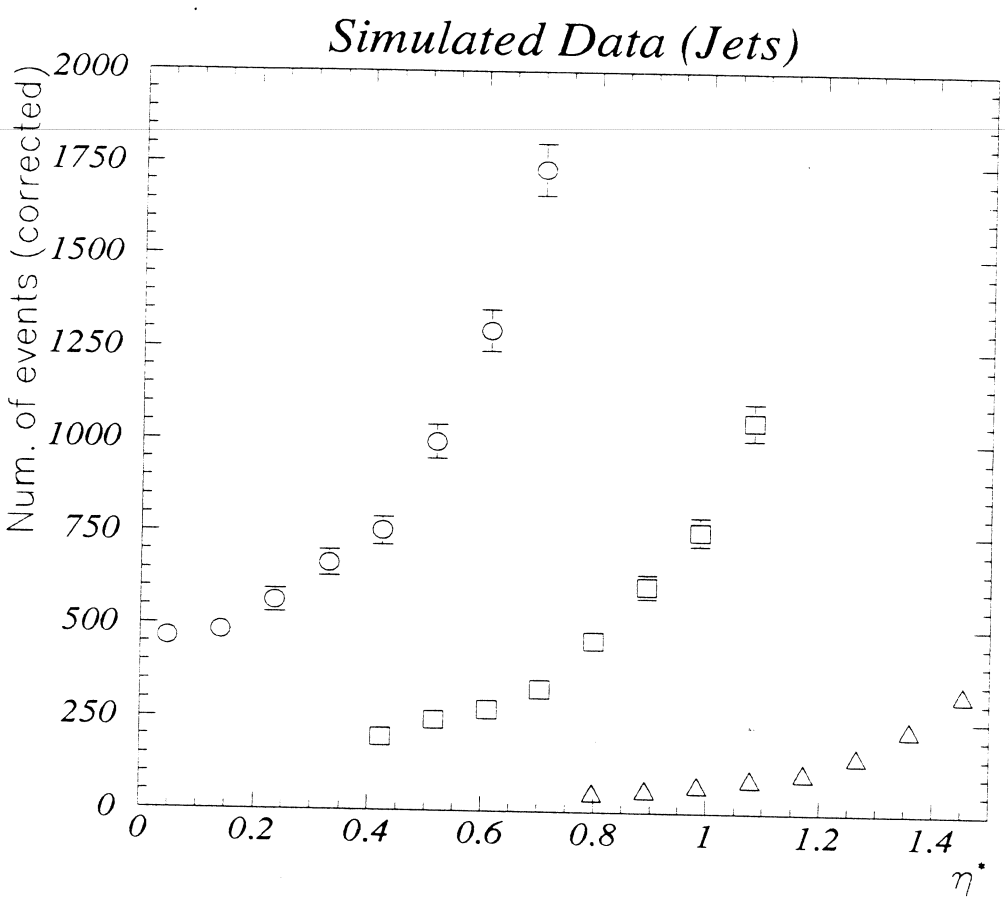

Figure 6.8: Simulated photon data plotted in bins of η^*.

tribution of photons, we can model the data as:

$$N_i^{data} = N_i^{\gamma} + N_i^{\pi} \tag{6.19}$$

with the constraint that

$$\sum N_i^{\gamma} = F_{\gamma} \times \sum N_i^{data} \tag{6.20}$$

where F_{γ} is the photon fraction listed in Table 6.2. So that if we also have the measured jet distribution, N_i^{jet}, we can find the signal and background for each bin:

$$N_i^{\pi} = \frac{\sum N_i^{data}}{\sum N_i^{jet}}(1 - F_{\gamma})N_i^{jet} \tag{6.21}$$

and

$$N_i^{\gamma} = N_i^{data} - N_i^{\pi}. \tag{6.22}$$

More importantly, we have

$$\sigma^2_{N_i^{\pi}} = \left(\frac{\sum N_i^{data}}{\sum N_i^{jet}}\right)^2 \times \left[\left(N_i^{jet}\sigma_{F_{\gamma}}\right)^2 + \left((1 - F_{\gamma})N_i^{jet}\right)^2\right] \tag{6.23}$$

and

$$\sigma^2_{N_i^{\gamma}} = \sigma^2_{N_i^{\pi}} + \sigma^2_{N_i^{data}}. \tag{6.24}$$

It is clear that the error grows very quickly as N^{π} grows, because the final result depends on taking the difference of two large numbers. The error due to the uncertainty in the background subtraction is also an important contribution to the total error. The final results are summarized and discussed in the next and final chapter.

Chapter 7

Results

The previous chapters have presented the ingredients required for the measurement of the direct photon angular distribution. This chapter presents the final result and its interpretation. The required ingredients are:

- **Theoretical motivation.** Direct photons present a unique probe of QCD because they are better defined theoretically and better measured experimentally than jets. The measurement of the direct photon angular distribution is complementary to the direct photon cross section measurement.

- **Photon candidate selection.** DØ is well equiped to select and identify photon candidates. The efficiency and acceptance for photons in the central region is well understood.

- **Reconstructing the angle in the center of mass frame.** Photons are produce in the hard scattering between individual partons, and may have a large longitudinal boost relative to the lab frame. Using the

recoiling jets, we are able to reconstruct the center of mass kinematics. We check the accuracy of the reconstructed recoil jets by E_T balance.

- **Photon identification and purity estimation.** Photon identification is a very difficult problem in any hadronic experiment because of the large background from neutral mesons. It is especially difficult at DØ because we are unable to reconstruct the invariant mass of the neutral mesons. We rely on statistical methods of background subtraction based on the probability of observing a twice minimum ionizing track in the CDC and the expected differences in electromagnetic shower development.

- **Background subtraction.** The photon purity estimation is not accurate enough to be able to determine the number of photons in each bin independently. We use the observed angular distribution for jets to estimate the angular distribution of the photon background.

By pulling together the above ingredients, we are able to arrive at our estimate of the direct photon angular distribution in the center of mass frame, as shown in Figure 7.1 and Table 7.1 Overlaid on the data are lines indicating the prediction of the parton model for t-channel scattering with spin 1 particle exchange (dashed line). Also shown are theoretical predictions in the leading logarithm (LL) and next-to-leading logarithm (NLL) approximations. Many NLL predictions with different scales have been overlaid to show the dependence of the theory on the scale parameter μ as it varies from $.5E_T^\gamma$ (upper edge) to $2.0E_T^\gamma$ (lower edge). Since CDF has previously shown results binned in $\cos\theta^*$ the analysis has been repeated using similar binning. The results are

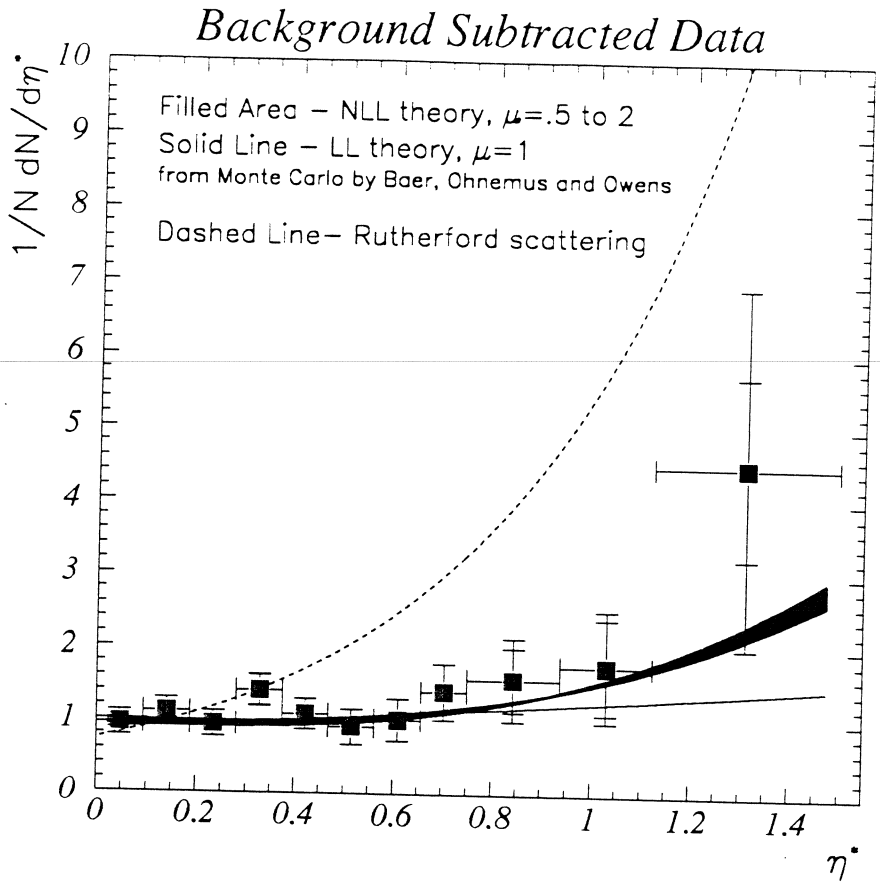

Figure 7.1: The observed angular distribution of direct photons in the center of mass frame after background subtraction. The overlaid curves are theoretical predictions, as explained in the text. The inner error bars exclude the error due to normalization between regions. The outer error bars correspond to the total error.

shown in Figure 7.2 and summarized in Table 7.2. For completeness, we also show the results of the previous analysis published by CDF [45] in Figure 7.3 Please note that the CDF analysis was carried out with different cuts and can not be thought of as being directly comparable to the analysis described here.

Table 7.1: The background subtracted direct photon angular distribution.

Bin	Range of η^* (min-max)	Normalized cross section	Error	Nominal NLL theory $\mu = E_T^\gamma$	Nominal LL theory $\mu = E_T^\gamma$
1	0.00000 - 0.09375	0.95	0.17	0.93	0.93
2	0.09375 - 0.18750	1.11	0.18	0.89	0.90
3	0.18750 - 0.28125	0.95	0.18	0.90	0.90
4	0.28125 - 0.37500	1.40	0.21	0.87	0.88
5	0.37500 - 0.46875	1.08	0.22	1.00	0.89
6	0.46875 - 0.56250	0.91	0.24	1.00	0.89
7	0.56250 - 0.65625	1.02	0.29	0.94	0.90
8	0.65625 - 0.75000	1.40	0.38	1.04	0.90
9	0.75000 - 0.93750	1.60	0.57	1.21	0.95
10	0.93750 - 1.12500	1.78	0.77	1.49	1.00
11	1.12500 - 1.50000	4.59	2.52	2.17	1.14

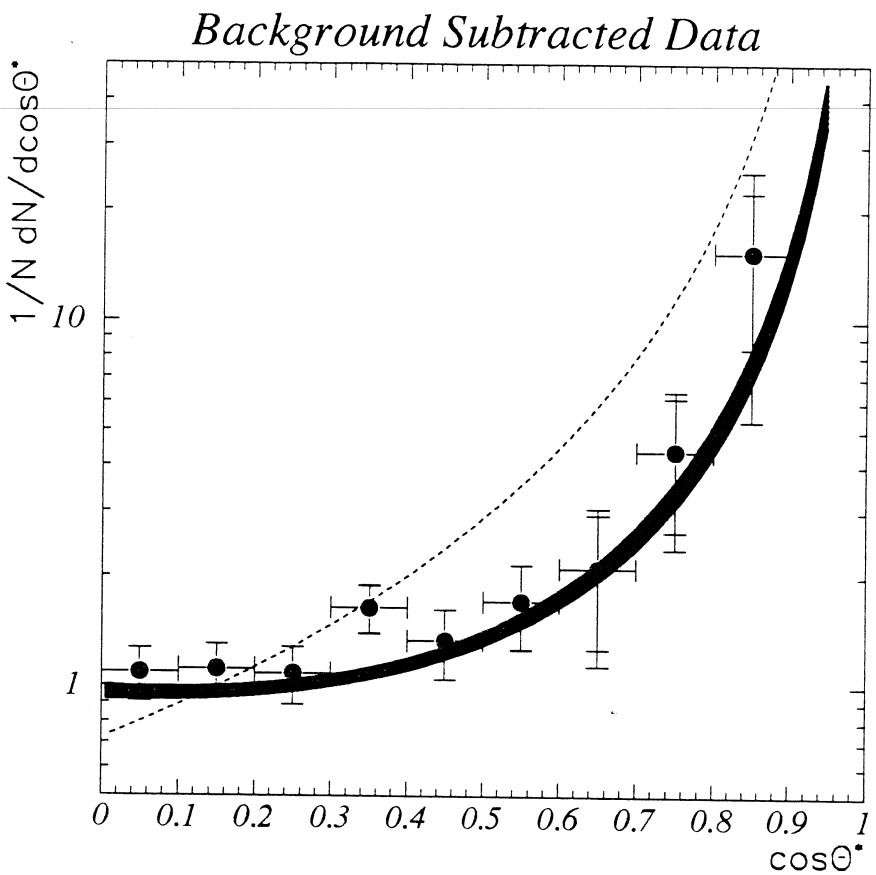

Figure 7.2: Same as Figure 7.1, but binned in $\cos\theta^*$. Leading order prediction is not shown. The dashed line corresponds to Rutherford scattering.

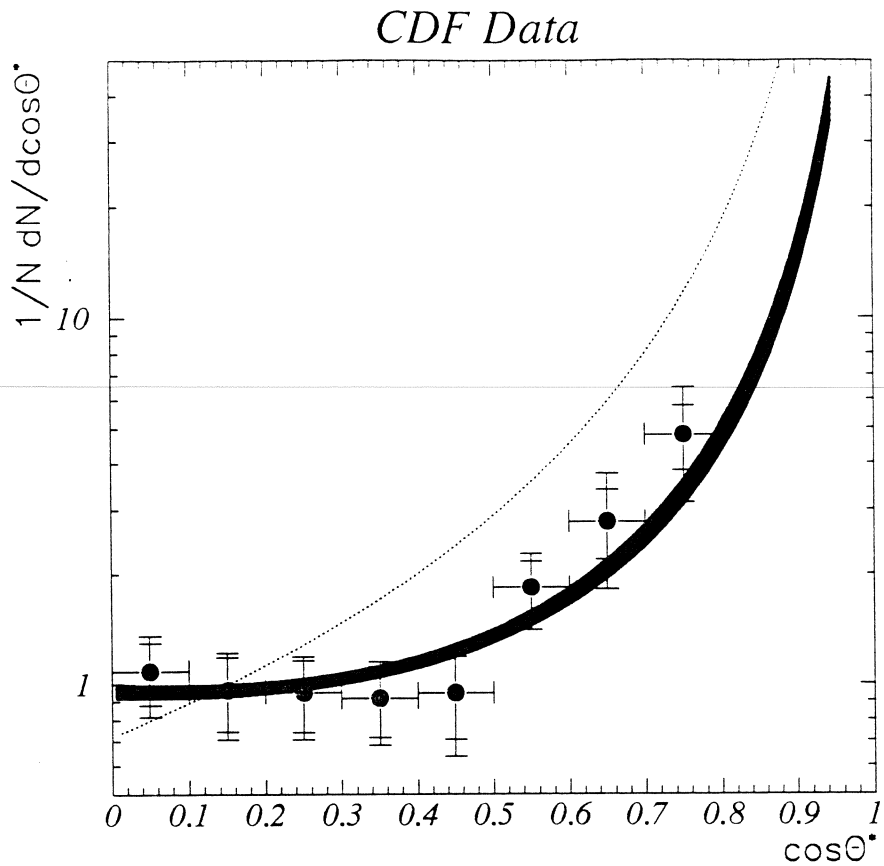

Figure 7.3: Results from an earlier analysis by CDF are shown over the theoretical predictions shown in Figure 7.2.

7.1 Conclusions

This dissertation presents the details of the first analysis of the direct photon angular distribution with the DØ detector. It is based on the data collected during the 1992-93 Tevatron run, during which the experiment accumulated approximately 15 inverse picobarns of data. This analysis extends the kinematic region explored previously. [47],[45]. The results show qualitative

Table 7.2: The background subtracted direct photon angular distribution.

Bin	Range of $\cos\theta^*$ (min-max)	Normalized cross section	Error	Nominal NLL prediction $\mu = E_T^\gamma$	Nominal LL prediction $\mu = E_T^\gamma$
1	0.0 - 0.1	0.95	0.17	0.93	0.93
2	0.1 - 0.2	1.11	0.18	0.89	0.90
3	0.2 - 0.3	0.95	0.18	0.90	0.90
4	0.3 - 0.4	1.40	0.21	0.87	0.88
5	0.4 - 0.5	1.08	0.22	1.00	0.89
6	0.5 - 0.6	0.91	0.24	1.00	0.89
7	0.6 - 0.7	1.02	0.29	0.94	0.90
8	0.7 - 0.8	1.40	0.38	1.04	0.90
9	0.8 - 0.9	1.60	0.57	1.21	0.95

agreement with QCD predictions, but favor next-to-leading order predictions over leading order predictions. The data is inconsistent with a simple Rutherford scattering hypothesis.

The result is dominated by statistical errors and by difficulty in background subtraction. DØ has accumulated an additional $100pb^-1$ of during the 1994-955 Tevatron run. However, this is not expected to fully alleviate the problem of statistics because the threshold of the lowest unprescaled photon trigger has increased to 45 GeV from $30Gev$. It is hoped that a better measurement of the angular distribution will be possible once the background subtraction methodology in the forward region has matured sufficiently. [54]

Bibliography

[1] I. Aitchison and A. Hey, **Gauge Theories in Particle Physics**, Adam Hilger, 1989.

[2] J. Owens, *Rev. Mod. Phys.*,**59**(2):465, 1987.

[3] V. Barger and R. Phillips, **Collider Physics**, p 193. Addison-Wesley, 1987.

[4] G. Kane, **Modern elementary Particle Physics** Addison-Wesley, 1993.

[5] R. Astur, (DØ), Experimental Results on Jet Shape and Subjet Analyses. To appear in *Proceedings of the $\overline{p}p$ Workshop* Fermilab, May 1995.

[6] G. Sterman, Introduction to the Parton Model and Perturbative QCD. Lecture notes from the CTEQ Summer School on QCD Analysis and Phenomenology, Aug 10-18, 1994. Unpublished.

[7] J. Botts, *et al.*, *Phys. Lett.* **B304**:159, 1993.

[8] H. Baer, J. Ohnemus, and J. Owens, Phys. Rev. **D42**(1):61, 1990.

[9] S. Abachi *et al.*, (DØ). *Nucl. Inst. Meth.*, **A338**:185, 1994.

[10] S. Snyder, *Measurement of the Top Quark Mass at DØ*, Chapter 3. Ph.D. Dissertation, SUNY at Stony Brook, Stony Brook, New York, May 1995.

[11] S. Rajagopalan, *The dE/dx Capabilities of the DØ Tracking System.* Ph.D. Dissertation, Northwestern University, Evanston, Illinois, June 1992.

[12] D. Pizzuto, *DØ Central Tracking Chamber Performance Studies.* Ph.D. Dissertation, SUNY at Stony Brook, Stony Brook, New York, December 1991.

T. Behnke, *The Central Drift Chamber for the DØ experiment: Design, Construction and Test.* Ph.D. Dissertation, SUNY at Stony Brook, Stony Brook, New York, August 1989.

[13] J. Kotcher, *Response of the DØ Calorimeter to Cosmic Ray Muons.* Ph.D. Dissertation, New York University, New York, New York, October 1992.

[14] S. Abachi *et al.*, (DØ). *Nucl. Inst. Meth.*, **A324**:53, 1993.

[15] W. R. Leo, **Techniques for Nuclear and Particle Physics Experiments**. Springer-Verlag, 1994.

[16] C. Fabjan, Calorimetry in High Energy Physics. In **Experimental Techniques in High Energy Physics**, T. Ferbel, editor. Addison-Wesley, 1987.

[17] V. Radeka and W. Willis, Calorimetry in High Energy Physics. In **Experimental Techniques in High Energy Physics**, T. Ferbel, editor. Addison-Wesley, 1987.

[18] W. Blum and L. Rolandi, **Particle Detection with Drift Chambers**. Springer-Verlag, 1993.

[19] J. Borders, Energy Linearity and Resolution of DØ Calorimeters. DØ Note 1171, 1991.

[20] N. Roe, Test Beam Results from the DØ End Electromagnetic Calorimeter. DØ Note 1287, 1991.

[21] M. DeMarteau, Electron Position Resolution in CCEM Modules. DØ Note 842, 1989

[22] N. Graf, Improvements to the Calorimeter Electron Position Algorithm. DØ Note 1352, 1992

[23] C. Gerber, *Measurement of the Production and Muonic Decay Rate of W and Z Bosons in $p\overline{p}$Collisions at $\sqrt{s} = 1.8TeV$ With the DØ Detector.* Ph.D. Dissertation, Universidad de Buenos Aires, Argentina, 1994.

[24] Q. Li-DeMatrteau. Private communication.

[25] J. Mead, A Current Monitoring and Protection System for the DØ Central Drift Chamber. 1993. Unpublished.

[26] N. Graf. Private communication.

[27] D. Schamberger. Private communication.

[28] N. Amos, J. Linneman, R. Partridge and L. Paterno, Luminosity Calculations for DØ. DØ Note 2031, 1994.

[29] M. Abolins, D. Edmunds, P. Laurens and B. Pi, *Nucl. Inst. Meth.*, **A289**:543, 1990.

[30] S. Fahey, *Direct Photon Production at* $\sqrt{s} = 1.8TeV$. Ph.D. Dissertation, Michigan State University, Lansing, Michigan, July 1995.

[31] S. Youssef, *Comp. Phys. Comp.*, **45**:423, 1987.

[32] U. Heintz and M. Narain, A Study of Electron ID Efficiencies using $Z \rightarrow ee$ Decays. DØ Note 1814, 1993.

[33] M. Fatyga, The Performance of the Liquid Argon Electromagnetic Calorimeters in DØ. Electron and Photon Identification in DØ. DØ Note 1521, 1992.

[34] N. Denisenko, Electron identification in the DØ detector. DØ Note 1885, 1993.

[35] R. Engelmann *et al.*, *Nucl. Inst. Meth.*, **A216**:45, 1983.

[36] A. Frodesen, O. Skjeggestad and H. Tofte, **Probability and Statistics in Particle Physics.** p. 424. Columbia University Press, 1979.

[37] Particle Data Group, *Phys Rev.*, **D50**(3):1173-1876, August 1994.

[38] N. Hadley, Cone Algorithm for Jet Finding. DØ Note 904, 1989.

[39] V. D. Elvira, *Measurement of the Inclusive Jet Cross Sections at* $\sqrt{s} = 1.8TeV$ *with the DØ Detector.* Ph.D. Dissertation, Universidad de Buenos Aires, Argentina, 1994.

[40] M. Bhattacharjee, D. Elvira, G. Blazey, Efficiencies of the Standard Jet Cuts for Cone Sizes: 0.3, 0.5, 0.7. DØ Note 2197, 1994.

M. Bhattacharjee, D. Elvira, G. Blazey, Jet Energy Resolution. DØ Note 2557, 1995.

[41] R. Kehoe and R. Astur. Determination of the D0 Jet Energy Corrections, DØ Note 2597, 1995.

R. Astur. Energy Scale Corrections, DØ Note 2089, 1994.

[42] R. Hirosky, A Data-based Estimate of Jet Reconstruction Efficiencies. DØ Note 2369, 1994.

[43] R. Hirosky, A Data-based Estimate of Jet Reconstruction Efficiencies. DØ Note 2405, 1995.

[44] F. Abe, *et. al.* (CDF), Phys. Rev. Lett. **68**(18):2734, 1992.

[45] F. Abe, *et. al.* (CDF), Phys. Rev. Lett. **71**(5):679, 1993.

[46] S. Keller and J. Owens, Phys. Lett. **B269**:445, 1991.

[47] L. Nakae, PhD Dissertation, *Direct Photon Center-of-Mass Angular Distributions in Proton-Antiproton Collisions.* PhD Dissertation, Brandeis University, Waltham, Massachusetts, April 1992.

[48] The OPAL collaboration, A Model Independent Measurement of Quark and Gluon Jet Properties and Differences. CERN-PPE/95-075. (unpublished)

[49] L. Lyons, **Statistics for Nuclear and Particle Physicists**. Cambridge University Press. 1993.

[50] S. Fahey. Private communication.

[51] S. Jerger, A Photon Purity Measurement in the Central Region. DØ Note 2636, 1995.

[52] G. Marchesini, B. Webber, G. Abbiendi, I. Knowles, M. Seymour and L. Stanco, *Comput. Phys. Commun.* **67**:465, 1992

[53] A. Milder, *Dijet Angular Distributions at* $\sqrt{s} = 1800GeV$ *Using the DØ Detector*. PhD Dissertation, University of Arizona, Tucson, Arizona, May 1993.

[54] Y.C. Liu. Private communication.